Investigations on Solid State Boosters and Polyoxometalates for Redox Flow Batteries

Felix Leon Pfanschilling

A thesis prepared for the degree of
Doctor of Philosophy

School of Natural and Environmental Sciences
Newcastle University
Newcastle upon Tyne
United Kingdom

October 2022

Abstract

The current fossil fuel based electricity production is unsustainable and a transition towards a decarbonised energy economy urgently needed. However, unlike electricity produced from fossil fuels, many renewable power sources provide power only intermittently, creating the necessity for expanding large scale energy storage. Among a multitude of technologies in this field, Redox-Flow batteries (RFBs) are of special interest for large scale applications, particularly due to their flexibility in capacity and power rating as well as their inherent safety advantages over other types of batteries. However, current RFB technologies often suffer from low energy densities and high capital costs, which prevent widespread use.

In this work, ways are explored to increase the capacity and energy density of RFBs by employing solid-state booster materials based on organic redox active materials. These capacity boosters are designed to be insoluble in the electrolytes while being able to exchange electrons with the redox active species therein, combining the flexible scalability and safety of a RFB with the higher concentration of active material in solid matter. Various attempts of demonstrating a capacity increase attributed to a booster are described and a successful proof of concept is shown, where the capacity of a half-cell could be increased by ca. 200% using a booster (from 22.3 mAh for the electrolyte alone to 67.6 mAh with booster). However, one of the major challenges found during this work was slow electron exchange between booster and electrolyte. Potential reasons and implications are discussed alongside possible solutions. The current development status of the concept of redox boosters is critically evaluated and teachings from the various investigations presented here are taken into account to gauge what future research is necessary to improve this concept.

Furthermore, a method of calculating the electrochemical potential in solution

for a species with more than two possible oxidation states is presented. The theoretical basis is derived from thermodynamic principles and experimental verification of the predictions is provided.

Acknowledgements

I would like to thank Prof. Ulrich Stimming for welcoming me as his PhD student and introducing me to the field of redox flow batteries, as well as for giving me the opportunity to engage with the scientific community and to participate in various conferences.

A huge thank you to Alan Wiles from the University of Glasgow for the fruitful collaboration on the booster project. Alan developed and synthesised the organic booster materials investigated in this project and proved to be a fountain of creative ideas. Many thanks also for the helpful discussions in our frequent exchanges, for giving me the opportunity to visit the laboratory in Glasgow and for coming to visit the laboratory in Newcastle.

I am very grateful for the friendship of Jack Mitchinson, with whom working is both remarkably productive as well as enjoyable. Together with Jack the idea for extending the Nernst equation to more than two oxidation states was developed and successfully implemented. The result of this collaboration can be seen in form of chapter 6 of this thesis.

Many thanks also to the other members of the research group. They were always prepared to give a helping hand in the laboratory and to give advice when discussing results. It was a pleasure to work in this environment and to spend time with them.

I would also like to thank Jochen Friedl for his support in getting a foothold both in the UK and in energy research.

A very warm thank you also goes to Isabelle Gerz for her tireless efforts in proofreading my thesis and her helpful and encouraging advice.

I am deeply thankful for the support and encouragement from my family, who always believed in me and who ultimately made it possible to move abroad

and to pursue a doctoral degree.

And finally I would like to thank Denise Wagner for her love and support and for the tremendous amount of patience she showed during this endeavour.

Contents

List of Figures

List of Tables

Chapter 1

Introduction

The ever growing demand for energy poses one of humankind's major challenges today. Since the start of the industrial revolution and the large-scale use of fossil fuels, the world's energy consumption has been growing continuously.

From 1969 to 2019, a period of only 50 years, the global primary energy consumption (i.e. commercially traded fuels as well as renewables used to generate electricity) more than tripled, from 193 EJ to 587 EJ (see figure 1.1, growing at a current rate of ca. 1.3% (10-year average 2011-2021).[1, 2] In 2021, global electricity consumption amounted to ca. 102 EJ, out of which 15% were produced from hydropower and 13% from other renewable power sources. The majority of electric power, however, was produced from coal and natural gas (36% and 23%, respectively).[2]

This modus operandi is highly unsustainable and a decarbonisation of the energy industry is urgently required.[3]

For the transition to a more sustainable energy economy, it is crucial to move away from fossil fuel consumption and to expand the utilisation of renewable energy sources. This shift, however, creates new challenges: As most renewable energy sources, like solar and wind power, provide energy only intermittently, the necessity of increased storage arises. Production peaks usually do not match consumption peaks, so electricity grids need to be buffered in order to ensure a stable energy supply. This task requires efficient and flexible storage solutions over a range of different scales. Redox flow batteries (RFBs) have the potential

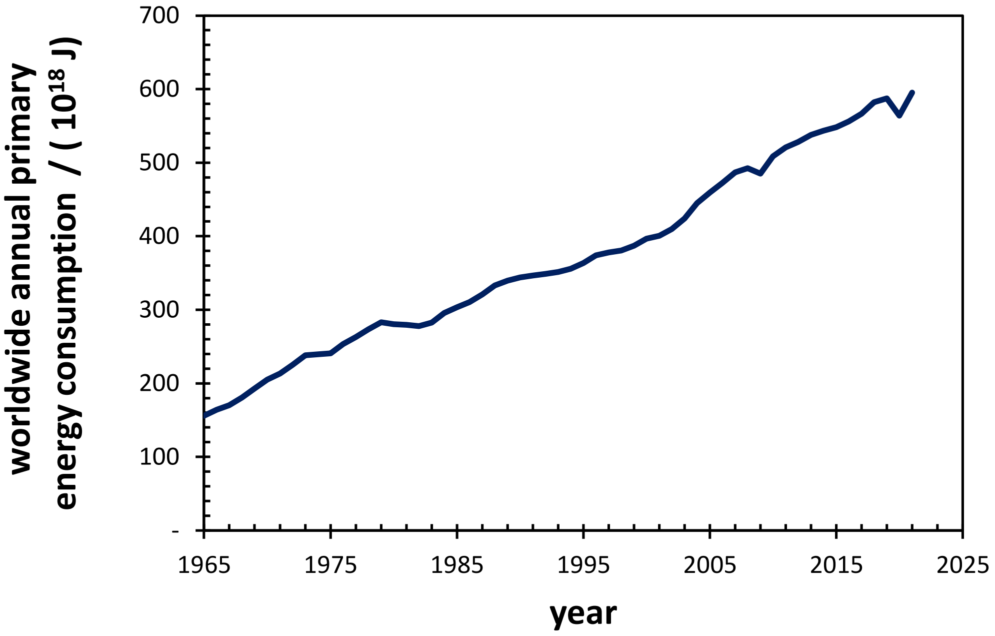

Figure 1.1 Development of worldwide primary energy consumption (commercially traded fuels, hydroelectricity, other renewables) in EJ/year.[2]

to be part of the solution to this challenge.

The development of such a battery lies at the heart of this thesis, with the different chapters covering various aspects of this endeavour. Chapter 2 introduces the reader to some of the fundamental concepts of energy storage and details advantages of RFBs for the purpose of (large scale) energy storage as well as associated challenges. It also provides information on polyoxometalates (POMs) and solid state redox boosters and their respective roles in energy storage. In chapter 3, an overview is given about various RFB-concepts and previous works on solid-state boosters as well as POM-RFBs. Chapter 4 provides details on methods and materials utilised in the investigations presented in this work. Following this, chapter 5 details the investigations and results on solid state booster materials including a proof of concept. The results are discussed and an outlook on possible future investigations is given. Chapter 6 is intended as a paper manuscript and describes the calculation of the electrochemical potential from the average oxidation state for a dissolved species with more than two possible oxidation states, such as a POM. The underlying theory is derived from thermodynamic principles and experimental verification of the resulting predictions is provided.

Chapter 2

Fundamentals

2.1 Energy storage systems

The transition to a sustainable energy economy requires enormous efforts and investments in renewable energy sources. However, increasing renewable electric energy production is only a part of the solution. Equally important is the capability to store the produced energy. As mentioned above, one of the major challenges associated with renewable energy sources like wind and solar power is their intermittent nature. Furthermore, power production is only partially predictable and can vary, as the amount of power produced does not only depend on the time of day and the current weather, but is also affected by seasonal changes. These variabilities hinder more widespread implementation of wind and solar power. In order to increase the percentage of renewable energy in the energy mix and ultimately transit to decarbonised power systems, it is necessary to implement adequate energy storage solutions.

However, such a multi-faceted challenge requires a diverse approach as there will be no single energy storage solution solving all problems at hand. For instance storing vast amounts of energy over long periods of time to buffer seasonal changes in energy production (e.g. for large wind farms) requires a different solution than energy storage in residential applications. In the latter case the aim might be to balance household energy consumption and production of e.g. solar panels on the roof over the course of a day.

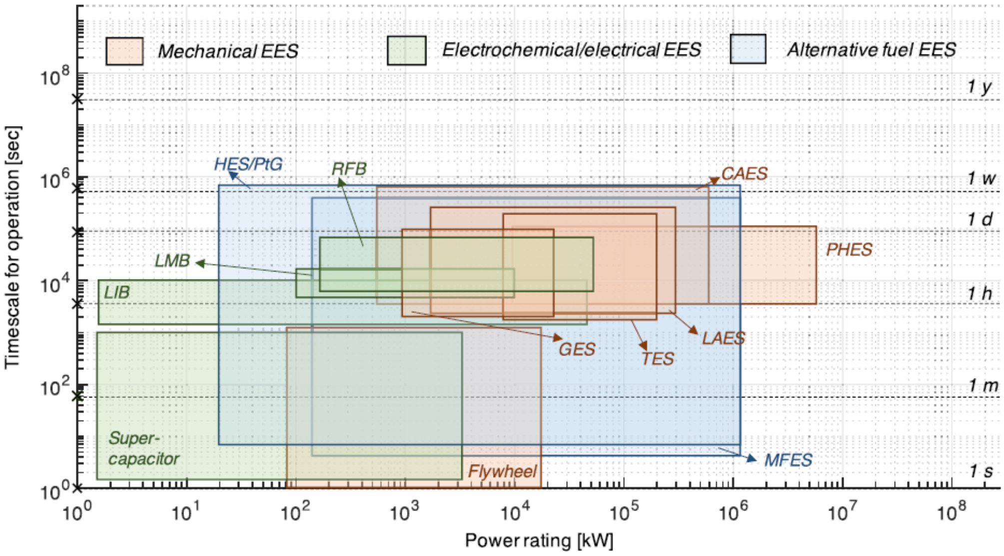

Figure 2.1 Various electric energy storage systems with operation timescales and power rating reprinted from He *et al.*[4] Original caption: "Comparison of power rating and timescale for operation between different EES technologies" Abbreviations: EES = electric energy storage, HES/PtG = hydrogen energy storage/power-to-grid, RFB = redox-flow battery, CAES = compressed air energy storage, LMB = liquid metal batteries, PHES = pumped hydro energy storage, LIB = lithium-ion battery, GES = gravity energy storage, TES = thermal energy storage, LAES = liquid air energy storage, MFES = metal fuel energy storage. Creative commons license CC BY 4.0.

There is a vast variety of ways for realising electric energy storage at different scales: From mechanical energy storage systems, like pumped hydro energy storage, compressed air, liquid air or flywheels via electrochemical systems, like lithium-ion batteries (LIBs), RFBs or supercapacitors to chemical storage like hydrogen gas and other power-to-fuel/fuel-to-power systems.

Figure 2.1 from He *et al.* compares various electric energy storage systems with respect to their timescale of operation (in seconds) and the scale of their power rating (in kW).[4] Systems with short timescales of operation, like flywheels and supercapacitors, are often found in power management systems, like grid frequency regulation and in uninterruptible power supplies.[5]

At longer timescales of operation and generally also at higher power ratings, systems like gravity energy storage, thermal energy storage and batteries can be found. Gravity energy storage builds on the increased potential energy of an elevated solid mass. It is lifted during energy excess (charging), whereas lowering the mass discharges the stored energy through driving a generator. Thermal energy storage is usually operated either as individual power-to-heat/heat-to-power system or integrated with other types of electric energy storage to recover waste heat and boost efficiency.

The largest timescales of operation and power ratings can be found with systems like compressed air energy storage and pumped hydro energy storage, which are generally deployed at large scales.

One of the major considerations for determining reasonable deployment sizes is how the respective technology scales. This can be illustrated by comparing technologies like supercapacitors and LIBs with pumped hydro storage: While supercapacitors and LIBs offer good energy and power density, doubling their capacity or power output essentially requires doubling the amount of raw materials used so large scale deployments do not offer big cost advantages. Thus, these technologies tend to be used when space is limited and/or weight has to be minimised (e.g. in mobile applications). In the case of pumped hydro storage on the other hand, doubling the capacity merely requires doubling the size of the reservoirs while the rest of the high upfront-cost infrastructure remains largely the same. Hence, there is no incentive to implement technologies like pumped hydro storage below a certain scale as they only become cost effective at larger deployment sizes.

Beyond scalability, there are other important metrics for characterising and evaluating potential use cases for electric energy storage systems: capital cost ($/kWh of installed capacity), levelized cost of storage ($/kWh of discharged energy over the complete lifetime of a device when accounting for all associated costs of operation), energy density (kWh/L), power density (W/L), energy efficiency (percentage of retrievable energy after accounting for all loss mechanisms), system lifetime (calendar and/or cycle lifetime), response time (the time delay before a system delivers a rated power), (future) availability of raw materials, geographical feasibility, safety considerations, etc.[4, 6–8]

The various electric energy storage systems mentioned above vary greatly in terms of these parameters and the preferred type of storage always depends on the intended application. The individual evaluation of these various electric energy storage systems is beyond the scope of this work. The reader is therefore directed to a recent introductory review on electric energy storage provided by He *et al.*, discussing a broad range of energy storage technologies in further detail and exploring strengths and weaknesses as well as economic challenges and opportunities.[4]

The battery type investigated in this work is the redox flow battery. It offers some very interesting properties for buffering the output of intermittent renewable energy sources like solar panels or wind turbines for medium- to large scale applications. These properties are discussed in the following section.

2.2 Redox flow batteries

A RFB is a special type of battery where the charge is stored in a fluid: The electrochemically active material is present either in the liquid state or in a dissolved state, called the electrolyte. Only a part of the electrolyte is present in the electrochemical cell at any given time; the rest is stored in two (or sometimes four) separate tanks. Besides the electrochemical cell (where the electrochemical reactions take place) and the tanks (where the majority of the charge is stored), a typical RFB comprises a battery management system, tubing and pumps. The latter enable transport of the electrolytes from the tanks to the cell and back in two separated circuits for the high-potential (catholyte) and low potential electrolyte (anolyte), respectively. During charging of the battery, the catholyte is being oxidised and the anolyte is being reduced, and vice versa during discharging.

The RFB-cell itself (as depicted in figure 2.2) consists of two compartments, separated by an ion-conducting membrane that is permeable for certain ions to allow for charge balancing during charge or discharge but ideally does not allow for the electrochemically active materials to cross over into the other compartment. Each half cell contains an electrode that is connected to a metal current collector, typically via an electrochemically inert material, such as graphite, to prevent contact and reactions between the electrolyte and the metal. The actual electrochemical reactions take place at the interface between

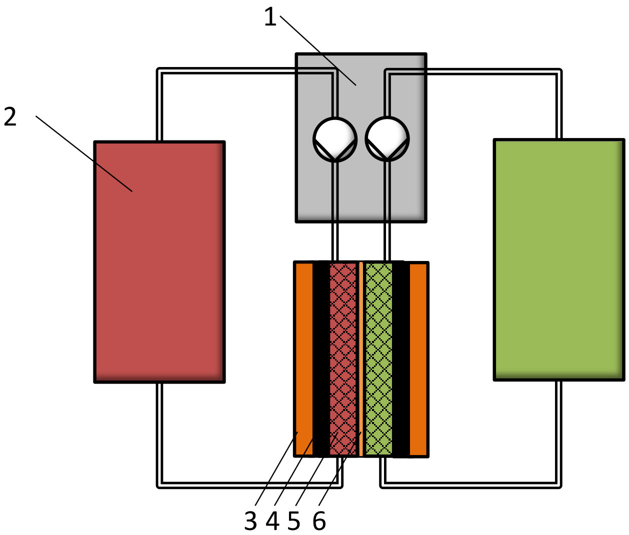

Figure 2.2 Schematic of a RFB. (1) pump, (2) electrolyte tanks, (3) metal current collector, (4) graphite plate, (5) porous electrode, (6) ion-conducting membrane (separator).

electrolyte and electrode (usually porous, carbon-based materials, like carbon papers or carbon felts), so the electrode itself does not undergo chemical reactions. Thus, ageing and degradation, which are common problems in other types of batteries, are considerably limited.[9, 10]

The working principle outlined above implies a spatial decoupling of energy conversion (taking place in the cell) and energy storage (taking place in the electrolyte tanks). This unique feature of RFBs allows for independent scaling of energy content and power of the battery.

Another major advantage of this concept when using aqueous electrolytes is the RFB's inherent safety due to non-flammability. Other types of batteries, for example LIBs, tend to rapidly release vast amounts of energy in the form of heat and/or catch fire after malfunctions or damage. These hazards are even more serious in large scale deployments, where a single malfunctioning cell can cause damage to nearby cells.[11] Such runaway events can be excluded if aqueous RFBs are employed instead.

A remaining risk of RFBs is leakage, releasing the often acidic electrolytes. This is usually mitigated by placing appropriate collection containers underneath the battery. Even in the unlikely event of a rapid mixing of both electrolytes in the battery's charged state, a catastrophic energy release is not conceivable: The limited energy density together with the high heat capacity of water, the main constituent of the electrolyte, would merely lead to a limited rise in temperature.[1] Consequently, this risk is manageable by keeping temperature stabilities in mind when selecting construction materials for the RFB.

Early on, Dr. Walther Kangro of the Technical University of Braunschweig worked on methods of storing electricity in liquids, submitting his first patent on the subject in 1949.[12] This patent already contained many characteristics of RFBs seen today, like carbon-based electrodes and membranes to separate the electrolytes. Interestingly, it also already points out the advantages of using the same element in both half cells, namely mitigating long-term capacity fade due to cross-over (the process of unwanted migration of the redox-active species through the separator/membrane). Nevertheless, when NASA started their 'Redox Storage System Technology Project' in 1973, they decided to use iron and chromium as the positive and negative redox-active species, respectively.[13]

The first patent for an all-vanadium redox-flow battery (VRFB) with electrolytes based on sulfuric acid was filed in 1986 by Skyllas-Kazacos *et al.* at the University of New South Wales.[14] The first large scale application of a VRFB was realised about a decade later in 1997 by Mitsubishi Electric Industries together with the Kashima-Kita Electric Power Corporation, who built a 200 kW/800 kWh system.[15]

Since then, numerous projects for practical applications of RFBs have been realised at various scales. Even though other chemistries for the redox-active materials have been developed (see chapter 3), most large scale applications still rely on the all-vanadium technology, as it is the most mature RFB technology at this point.[16, 17] While the VRFB offers great calendar- and cycle stability as well

---

[1] E.g.: The energy density of a typical all-vanadium redox-flow battery of 25.3 $\frac{\mathrm{Wh}}{\mathrm{L}}$ (determined from a typical vanadium concentration of 1.5 $\frac{\mathrm{mol}}{\mathrm{L}}$ with a standard potential difference of 1.26 V) of electrolyte translates to 91.2 $\frac{\mathrm{kJ}}{\mathrm{L}}$. Due to the heat capacity of 4.184 $\frac{\mathrm{J}}{\mathrm{kgK}}$ (at 20 °C) found in water, 72 kJ of heat would increase the temperature of 1 kg of water by only about 21.8 K (depending on exact conditions). The electrolytes obviously do not only consist of water, but this example serves to illustrate that the water content alone would be able to absorb the total energy content of the battery at only a limited temperature increase.

as relatively simple, scalable electrolyte preparation (dissolving vanadium salts in aqueous inorganic acid solutions), it comes with certain unsolved challenges. Issues like low energy efficiency and the relatively low energy density (25 Wh/L (see above) in a typical VRFB vs. around 670 Wh/L in a typical LIB[18]) limit its breadth of application. Additionally, while cross-over does not lead to an accumulating permanent capacity loss in a VRFB (since both half-cells use the same element), it results in some self-discharge and thus decreases coulombic and energy efficiency.[19]

In order to improve on these shortcomings, a potential alternative for the redox-active material would need to exhibit high solubility in water and/or allow multiple electron exchanges per molecule (for greater energy density) and have fast electron exchange kinetics (for greater power density), whilst undergoing limited or no cross-over and maintaining high cycle stability and non-flammability. One potential candidate to fulfil these criteria are POMs, introduced in the following section.

2.3 Polyoxometalates

Polyoxometalates (POMs) are clusters of transition metal oxoanions. The metal-oxygen polyhedrons (usually octahedrons) are connected via shared oxygen atoms to form symmetrical molecules. Isopolyoxometalates consist of only one type of metal oxide whereas heteropolyoxometalates comprise at least one additional heteroatom (not necessarily a metal).[20]

Structure

POMs come in a variety of structures which usually exhibit high symmetry. Common examples for isopolyoxometalates are the Lindqvist structure $[M_6O_{19}]^{n-}$ and the decavanadate $[V_{10}O_{28}]^{6-}$.[21] However, the most well-known POM structure is probably the so called Keggin structure $[XM_{12}O_{42}]^{n-}$ (X = central (hetero)atom and M = metal framework atom), an example of a heteropolyoxometalate. Many other POMs can be derived from smaller POM structures, like the Dawson structure $[X_2M_{18}O_{62}]^{n-}$, which can be described as two lacunary Keggin-type

POMs linked together.[22] POM structures cover a wide range of sizes: From small clusters like the Lindqvist structure to POMs containing several hundred atoms.[23]

Usable Elements

Well known examples for the metal framework of POMs are tungstates and vanadates. In previous studies, the use of $[PV_{14}O_{42}]^{9-}$ (PV_{14}) and SiW_{12} as redox-active electrolytes in a RFB could be demonstrated by our group.[24, 25]

However, a number of other elements are also suitable for forming the metal framework of POMs, mainly other group V metals (niobium, tantalum) or molybdenum, a group VI metal. Typical heteroatoms are phosphorus and silicon, but more than 50 other elements have also been reported as heteroatoms in POMs, providing a huge variety of combinations.[20] Furthermore, it is possible to create POMs with more than one type of metal in the framework. Elements like iron, manganese, aluminium, gallium, nickel, copper, zinc, etc. can be incorporated into the structure to form new POMs with different chemical and electrochemical properties.[26–28] Properties like solubility, stability, or redox-behaviour of a POM can be tailored by exchanging one or more atoms of the original structure with alternative elements. For use in large scale energy storage, low-cost, earth abundant elements, such as iron, manganese, nickel or aluminium are of special interest. Various POMs incorporating those elements have already been reported in the literature, examples for which are: $[SiW_9O_{37}Fe_3^{III}(H_2O)_3]^{7-}$, $[SiW_9O_{37}Mn_3^{II}(H_2O)_3]^{10-}$, $[SiW_9O_{37}Ni_3^{II}(H_2O)_3]^{10-}$, $[SiW_9O_{37}Al_3(H_2O)_3]^{7-}$, $[Mn_4^{II}(H_2O)_2(SiW_9O_{34})_2]^{12-}$ and $[AlO_4Al_{12}(OH)_{24}(H_2O)_{12}]^{7+}$.[26, 28, 29]

Synthesis

Polyoxometalates are formed by condensation reactions (olation and oxolation) from dissolved metal oxides, linking them together via bridging oxygen atoms. These reactions are self-assembly reactions, occurring when a solution of the respective metal oxide is acidified.[20] The reactions are controlled mainly via pH, concentration and temperature. Which kind of POM is formed is further influenced by the type of counter cation(s), solvent(s) and additional elements

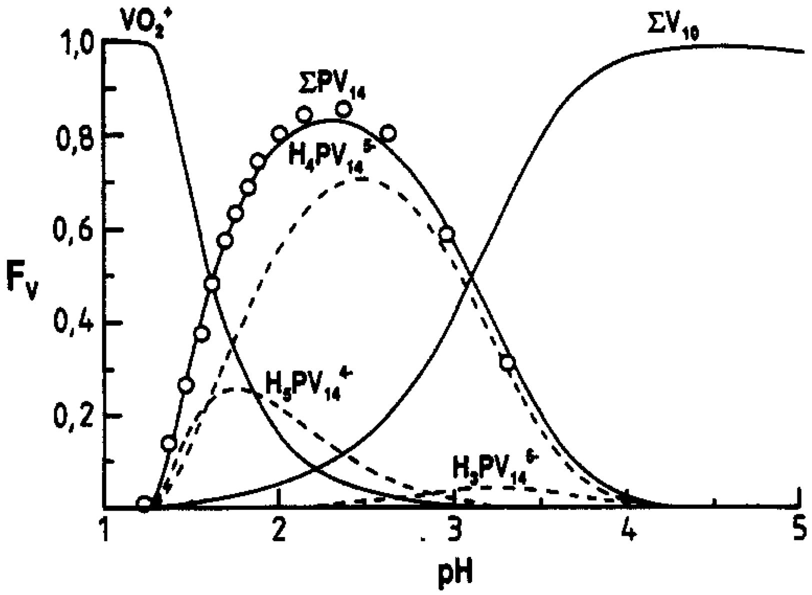

Figure 2.3 pH-dependency of the vanadophosphate-system as shown by Selling *et al.* Original caption: "Distribution of vanadium species at equilibrium plotted vs pH, in solutions of 8 mM P, 24 mM V, 0.6 M Na(Cl), at 25 °C. F_V is the fraction of the total vanadium. The circles represent NMR integral data from equilibrated solutions." Reprinted with permission from.[32] Copyright 1994 American Chemical Society.

in solution.[30] The complex underlying mechanisms of this self-assembly are not yet fully understood. Despite the vast number of contributing factors, by carefully controlling the above parameters it is often possible to obtain (mainly) a single molecular species.[31] In the case of the synthesis of PV_{14}, phosphoric acid is added to a solution of sodium or lithium metavanadate with the resulting mixture being further acidified using hydrochloric acid. Depending on the pH, the predominating species will be either VO_2^+, $[PV_{14}O_{42}]^{9-}$ or $[V_{10}O_{28}]^{4-}$, as can be seen in Figure 2.3.[32] A detailed synthesis procedure for PV_{14} can be found in section 4.2.2 on page 36.

The synthesis of PV_{14} can be performed as a one-pot reaction. However, more sophisticated POMs usually require a more elaborate approach, such as the formation of a lacunary species first and the consequent addition of a second framework metal, for instance. Intermediate purification steps are also necessary in certain reactions.[20]

2.4 Solid state boosters

2.4.1 Concept

As described in section 2.2, RFBs provide various advantages over other types of batteries. Nevertheless, their applicability faces the major challenge of a relatively low energy density, which is often limited by the solubility of the active species. Typical solubility values of metal ions in water are on the order of 1 M, or 0.001 mol/cm^3. In contrast, the amount of atoms in solid matter can be around two orders of magnitude greater. The aim of this project was to combine the advantages of RFBs with the energy density of solid state batteries, as depicted in the schematic in figure 2.4. In order to achieve this, the majority of the charge should be stored in solid state porous redox-active polymers (‘boosters’) located in the electrolyte tanks. In this concept, the dissolved redox-active material would mainly act as a shuttle carrying charge between the electrochemical cell and the tanks. This approach builds on the one described by Zanzola *et al.*,[33] as discussed in section 3.3 on page 23. They used polyaniline as the booster material and worked on targeting the two redox events of this material (transitions from emeraldine to pernigraniline and leucoemeraldine to emeraldine) with varying success.

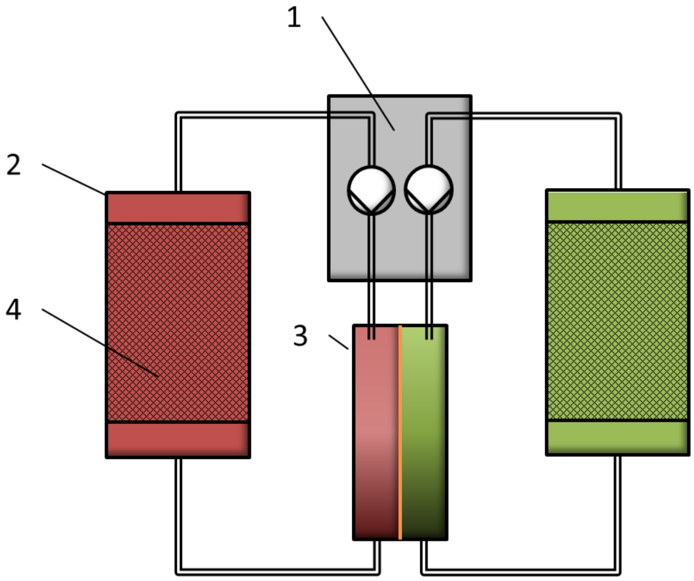

Figure 2.4 Schematic of a RFB equipped with solid state boosters in both half-cells: (1) pump, (2) electrolyte tanks, (3) electrochemical cell and (4) booster polymer. The booster polymer is kept in the electrolyte tanks and in direct contact with the electrolyte solution to allow for electron exchange between them.

2.4.2 Porosity

The original idea was to introduce designed porosity in the booster material on a molecular level by carefully selecting the constituents. This could for instance be achieved by reacting a rigid linear redox-active segment together with a linker of trifold symmetry (or a rigid linear linker together with a redox-active segment of trifold symmetry). This would force the material to polymerise in a hexagonal structure, leaving cavities that allow for equal access for the redox mediator to all active sites, as depicted in the schematic in figure 2.5. The individual monomers would therefore be designed to contain distinct functional groups to enable coupling reactions with each other in the desired places.

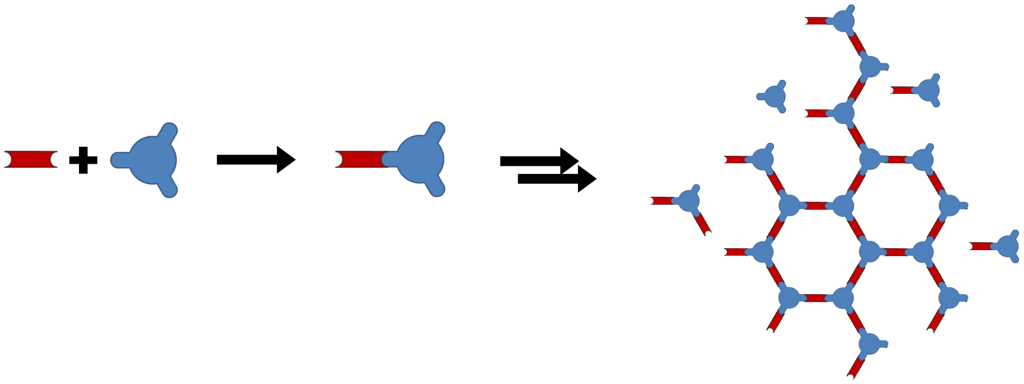

Figure 2.5 Schematic depiction of a synthesis for a polymer with designed porosity. Both monomers contain distinct functional groups compatible for a coupling reaction between them (depicted by the complimentary shapes). The final polymer is designed to contain hexagonal cavities through utilising one linear rigid molecule (red) and one with trifold symmetry (blue). In this concept, one of the monomers would contain the redox active section while the other one would act as structure-providing linker.

This method of carefully designed reaction sites where the functional groups of one of the monomers can react with the functional groups of the other monomer in a coupling reaction is depicted in the schematic in figure 2.5 by different complementary shapes representing the reactive sites in the individual monomers. The utilised reactions, however, may also include condensation reactions in which a small molecule is split off during the process, which, for reasons of clarity, is not detailed in the schematic.

2.4.3 Sketching the ideal booster

A hypothetical ideal booster polymer would be based on low-cost starting materials for a high-yield, scalable synthesis. The resulting product should be stable (long cycle lifetime as well as long calendar lifetime), insoluble in water but easily wettable in order to facilitate the electron transfer reactions between electrolyte and booster. The potential window should be equal or slightly narrower than that of the corresponding shuttle materials and within the water splitting window. Careful selection of booster-shuttle combinations is also crucial for optimising charge transfer between the two. Low specific weight is a secondary objective, as the target application is in stationary batteries. It is highly unlikely for a material to fulfil all of the above criteria, so the challenge is to find suitable candidates and evaluate trade-offs and compromises.

2.4.4 Booster - shuttle combinations

When identifying a potential combination of booster and shuttle, the principal aspect to consider is the standard reduction potentials (U^o) of the respective electron transfers. In the ideal case of zero overpotential for the redox reaction between shuttle and booster, it would be preferable to have the standard reduction potentials of shuttle and booster match as closely as possible. There is, however, a certain tolerance given by the concentration dependency of the Nernst equation:

$$U = U^o + \frac{RT}{nF} \ln \frac{c_{Ox}}{c_{Red}} \tag{2.1}$$

where U = (half-cell) reduction potential, U^o = standard half-cell reduction potential, R = universal gas constant, T = temperature, n = number of electrons transferred in the reaction, F = Faraday constant, c_{Ox} = concentration of the oxidised species and c_{Red} = concentration of the reduced species. Technically, U depends not on the concentration but on the activity of the oxidised and reduced species, but at low concentrations activity can be approximated as concentration, as discussed in section 6.2.1 on page 92.

If, for example, the ratio of oxidised to reduced species in the shuttle material is 10:1, the Nernst equation predicts a reduction potential for this solution 59 mV positive of the standard reduction potential (for a single electron transfer at 25 °C). This means that thermodynamically it is possible for a shuttle material to oxidise a booster material, even though its standard reduction potential might be lower than that of the booster. However, there are limits to this concept. As the ratio of oxidised to reduced species approaches either very small or very large values, mass transport limitations arise and reduce efficiency and eventually feasibility. Furthermore, the case of zero overpotential is a hypothetical one and in practice any redox reaction has some overpotential associated to it. As is the case in the primary redox reactions in a RFB, it is desirable to minimise any overpotentials in order to maximise efficiency. This is, however, not always possible and the overpotentials for the reduction and the oxidation of the booster might cause a significant difference between the electrochemical potentials required for oxidising and reducing the booster. Thus, it might be preferable to employ two different redox species as shuttle materials: One to target the oxidation of the booster and one to target the reduction, or to employ one species with multiple redox events of suitable electrochemical potentials, such as a POM.

Chapter 3

Redox flow battery concepts: State of the art

3.1 Aqueous and non-aqueous solvents and active materials

The solvents used in RFBs can be divided into two fundamental groups: aqueous solvents and non-aqueous or organic solvents. Both types feature their own advantages and suffer specific disadvantages. In general, water based solvents are considerably cheaper than their counterparts and unlike most organic solvents they are not flammable, which, especially in large scale applications, can be a prohibitively serious safety hazard. Whilst the VRB, as discussed in section 2.2, dominates large scale deployments, alternative aqueous RFB chemistries have been reported, such as complexated all-iron[34], Zn-MnO_2[35] or Br-AQDS (9,10-anthraquinone-2,7-disulphonic acid)[36].

However, using water based electrolytes in a RFB limits the maximum achievable cell voltage: From a thermodynamic perspective, the electrochemical stability window of water lies between 0.0 V vs SHE and 1.23 V vs SHE with hydrogen evolution reaction (HER) and/or oxygen evolution reaction (OER) occurring when operating outside this window.

Yet, even though the thermodynamic stability window of water is narrow, kinetic stabilisation can be used to expand the usable potential range by selecting beneficial combinations of electrode material and electrolyte composition.[37] This can be seen e.g. in the well-known lead-acid battery used as starter battery in cars. They are typically 6-cell batteries and can operate at > 12 V, i.e. > 2 V per cell. Given the right circumstances, this can be taken even further. For example Tomiyasu *et al.* reported a stability window of ca. 3.2 V for a saturated aqueous sodium perchlorate solution in a CV on GC.[38]

In contrast, some organic solvents have electrochemical stability windows in excess of 6 V (e.g. acetonitrile, trimethylphosphate or 1,2-butylene carbonate)[39], so that solvent stability is less of a concern when developing RFBs with these types of solvents. It comes thus as no surprise, that organic solvent-based RFBs regularly feature cell voltages in excess of 2 V.[40–42]

Organic solvents are often paired with organic active materials due to solubility considerations. Those systems can feature high concentrations of several mol/L[43], higher than typical aqueous systems (e.g. common vanadium concentration in a VRFB ≤ 1.6 M). Though for practical applications the concentration of active material can be lower, since additional supporting electrolytes might be required to make up for the lack in conductivity. E.g. Wei *et al.* reported a solubility of 5.2 M for (2,2,6,6-Tetramethylpiperidin-1-yl)oxyl (TEMPO) in ethylene carbonate/propylene carbonate/ethyl methyl carbonate, which drops to 2.0 M upon including 2.3 M $LiPF_6$ as supporting electrolyte.[40]

Generally, the often higher concentration of active material paired with high cell voltages allows for higher potential energy densities and power densities in non-aqueous organic RFBs compared to aqueous RFBs. This, however, comes at the expense of additional costs for the solvents and for mitigating the increased safety risks. Using aqueous solvents in combination with organic active materials would benefit both areas and is therefore especially desirable. However, insufficient solubility in aqueous media severely limits the amount of organic candidates for this role. Additionally, many newly proposed organic active materials are anolyte materials with only limited development on organic catholyte materials.[44] Furthermore, many organic active materials face challenges in terms of their electrochemical stability.

3.2 Stability and cost

Organic materials participating in redox reactions tend to undergo side reactions. Since the target application involves hundreds or thousands of cycles of repeatedly oxidising and reducing the material, even small capacity losses due to irreversible side reactions can quickly accumulate and significantly diminish the accessible capacity in a short time frame.

In contrast, this is of no concern for dissolved metal ions, which is why many early RFBs focused on this technology (see section 2.2). Metal based electrolytes can even be recycled electrochemically, whereas organic active materials can often only be thermally recycled.[45] Research in aqueous metal RFBs is ongoing: For example Li *et al.* reported successful efforts in increasing vanadium concentrations to 2.5 M.[46] Further increase to 3.2 M has also been reported, albeit at the cost of reduced material utilisation.[47]

However, besides safety, low-cost materials are deemed one of the most important aspects for future RFBs.[45, 48] Therefore, alternatives for expensive metal-based active materials (especially for those with volatile world market prices, such as vanadium, see figure 3.1) are sought, as evidenced by an increase in research on organic active materials.[45]

Yet, for the overall price for energy storage, capital costs of the material are only one part of the equation. This does not take into account e.g. after how many cycles a system needs to be replaced. An often used metric is levelized cost of storage (see section 2.1, page 7), which takes into account the longevity of the system and thus includes cycle stability in the cost calculations. In this regard, metal-based storage materials still have a clear lead, with cycle lifetimes for e.g. the VRFB of around 20,000 cycles[44], but promising approaches using organic (or combinations of organic and organometallic, e.g. complexed iron compounds) alternatives have been reported with capacity retention of >99.9%/cycle over several hundred cycles.[44, 50, 51]

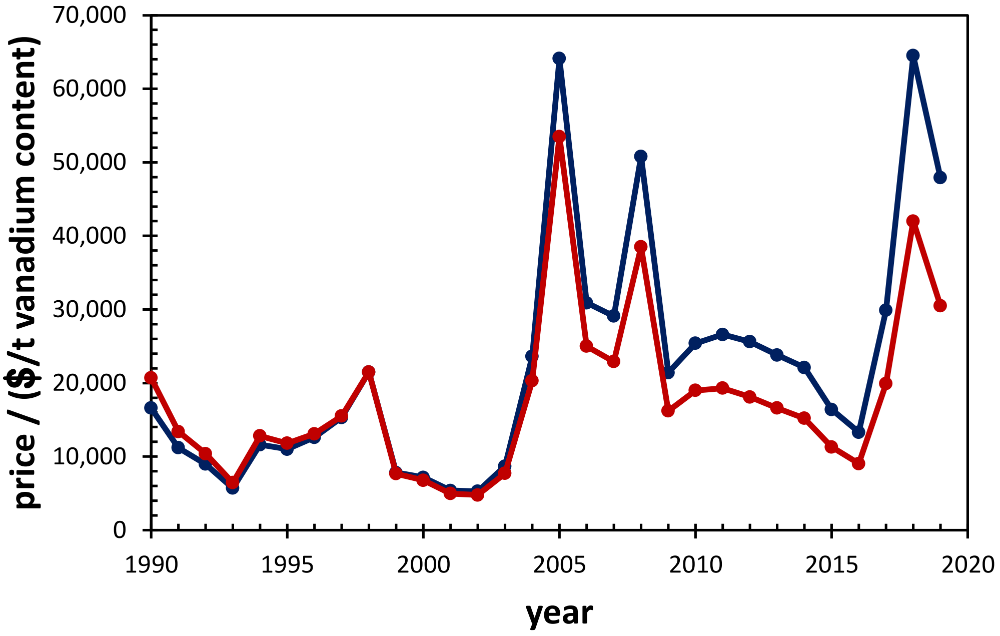

Figure 3.1 Vanadium world market price in USD per metric ton of vanadium content (blue graph) and adjusted to inflation (1998$, red graph). Data obtained from the U.S. Geological Survey.[49]

3.3 Solid state boosters

As described in section 2.4.1 (page 14), the basic incentive for using solid state redox boosters in RFBs is the combination of an RFB's flexibility and safety with the potentially higher energy density of solid redox-active materials.

To date, storing charge in an RFB by incorporating solid state materials has been attempted in various ways. For example Duduta *et al.* proposed a semi-solid flow cell which employed a RFB that was supplied with various LIB cathode materials in the form of particles in a slurry.[52] The maximum concentration they tested corresponded to a lithium concentration of ca. 12 M. However, a common problem with this approach is high viscosity of these slurries, which significantly increase pumping energy losses, especially at high flow rates, as well as poor conductivity.[52–54] Solid matter charge storage can also be realised via plating reactions in at least one half-cell of a RFB, often called hybrid RFBs. This has been done using various metals, including copper[55], iron[56] and zinc.[57, 58] Whilst promising, especially when using low-cost, earth-abundant elements, hybrid RFBs typically face challenges like electrode deformation (including dendrite formation), side reactions (e.g. HER) decreasing efficiency, as well as self-discharge.[56, 58]

To mitigate this whilst still exploiting the aforementioned benefits of both, RFBs and solid redox-active materials, Wang *et al.* in 2006 proposed redox targeting of lithium intercalation materials ($LiFePO_4$ in this case) with freely diffusing redox-shuttles. As an alternative to carbon-based conductivity-increasing additives or molecular wiring, this was done to address poor conductivity in the material.[59] Going further, in 2013 the same group proposed to integrate this concept in a RFB and presented what they called a redox flow lithium-ion battery.[54]

Zanzola *et al.* transferred these ideas to acidic aqueous systems, as those make up the majority of current large scale RFB realisations.[33] Their approach focused on using polyaniline (PANI), a polymer with three distinct oxidation states, namely leucoemeraldine, emeraldine and pernigraniline. They identified the Fe(III)/Fe(II) redox couple as a potential redox shuttle to target the emeraldine/pernigraniline reaction and V(IV)/V(III) for the leucoemeraldine/emeraldine transition. They used the same booster in both half-cells, which essentially uses only half of the possible electron transfers for each half-cell. In traditional flow-cells using dissolved metal ions there is an advantage to using the same material in both half-cells, namely avoiding permanent capacity loss due to cross-over. However, when it comes to selecting a booster material, there is no advantage during operation of an RFB to using the same booster material in both RFB tanks, as it is by design insoluble and thus not subject to cross-over. In fact, the redox active sites that are not used in one half-cell are essentially dead weight if they serve no purpose in the polymer structure.

In their work Zanzola *et al.* also noticed that in flow-cell tests the addition of the PANI booster actually decreased the capacity of the battery, unless a considerable amount of carbon black (CB) was added to the polymer (2.47 g CB plus 7.4 g PANI). The reason for this could not be determined. Upon addition of the CB, however, they managed to increase the capacity of their system by 49% over the baseline capacity.[33]

3.4 Polyoxometalates in energy storage

An alternative approach to improving on the shortcomings on aqueous metal RFBs is the use of POMs as active materials. As discussed in section 2.2 (page 11), low energy density and low power density are amongst the main challenges for current VRFBs. POMs feature multiple redox centres (facilitating high energy densities) and fast electron transfer (facilitating high power densities).[24] Furthermore, due to their nature as large anions cross-over through cation exchange membranes is negligible.[24] POMs and their electrochemical properties have been studied for several decades. Studies on SiW_{12} and other isostructural polytungstates for example have been presented as early as 1966 by Pope and Varga.[60] Launay presented investigations on highly reduced (up to 32 electrons per molecule) forms of ${H_2W_{12}O_{40}}^{6-}$ in 1976[61](publication in French) and Pope followed in 1983 with a comprehensive work on synthesis and properties of heteropoly- and isopolymetalates.[20] Wansheng and Zhorgyin in 1997 reported the use of four Keggin-type POMs (SiW_{12}, PMo_{12}, $H_3PW_{12}O_{40}$, $H_4SiMo_{12}O_{40}$) in combination with the Fe(III)/Fe(II) redox couple as the active materials in a

RFB.[62]

It is possible to employ the same POM species in both half cells of a RFB by exploiting different redox waves of the POM. Examples for this method have been reported, e.g. by Liu *et al.* and Pratt *et al.*, using ${CoW_{12}O_{40}}^{6-}$ and ${SiV_3W_9O_{40}}^{7-}$ as the active material, respectively.[63, 64] This practice eliminates the possibility of electrolyte cross-contamination through the membrane and simplifies material synthesis. However, as discussed above, it could be shown that cross-over is of no concern when using cation-exchange membranes with POMs.[24] Furthermore, using the same POM in both half-cells comes at the price of reduced maximum energy density. Only a limited amount of the POM's redox reactions is accessed in each half-cell, creating unused material and thus dead weight for the battery (similar consideration as for PANI, discussed in section 3.3 on page 24).

Alternatively, two different POMs can be used as active materials in a RFB, which was successfully tested in our group using PV_{14} and SiW_{12} for the catholyte and anolyte, respectively.[24] We were also able to demonstrate a scaled up version of this battery, which was continuously operated over approximately three months only exhibiting limited capacity fade.[25] The respective publication can be found in appendix B.

Chapter 4

Methods and materials

4.1 Cyclovoltammetry

Cyclovoltammetry is a versatile and powerful technique that can be used to gain a multitude of information about electrochemical reactions and processes at an electrode surface.[65] A very basic setup requires a conductive solution containing the dissolved redox active material to be analysed in a vessel equipped with a working electrode (WE), a counter electrode (CE) and a reference electrode (RE). A potential is applied between WE and CE, using the RE as a reference point, and the current response is recorded. However, in cyclovoltammetry the potential is not being kept static but rather constantly shifted at a steady rate (in mV/s), normally back and forth between two selected vertex potentials. If the potential reaches a value at which an electrochemical reaction takes place, an increase in the measured current can be observed. An oxidation taking place at the WE will produce a positive current shift while a reduction will produce a negative current shift.

An example of a typical CV of a single reversible redox event can be seen in the schematic in figure 4.1. Starting at the lowest potential (to the left) and then increasing this potential, the current initially barely changes (upper line). Only from a certain potential might an oxidation occur, indicated by an abrupt increase in current. At the onset of the current increase, the concentration of reduced redox-active species at the surface of the WE is the same as the bulk

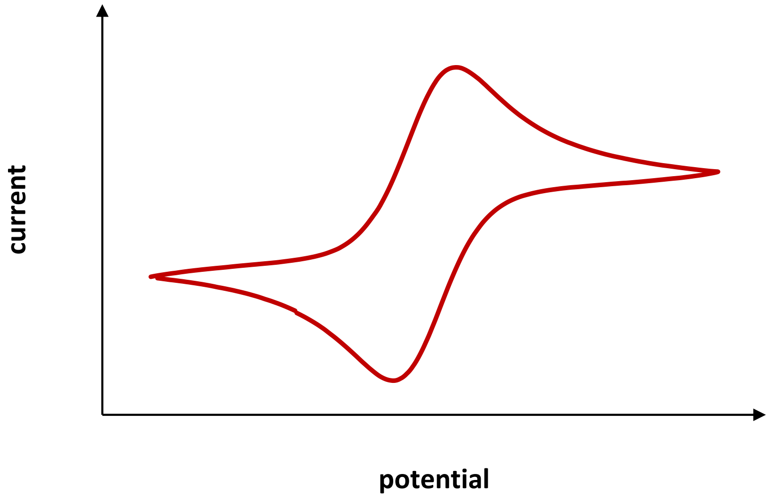

Figure 4.1 Schematic representation of a cyclovoltammogram of a reversible redox reaction.

concentration of that species. However, as soon as the oxidation reaction sets in and starts consuming the reduced species, its concentration drops at the surface of the WE surface, with diffusion then setting in to counteract the concentration imbalance between the bulk solution and the WE surface. At the same time the potential keeps getting shifted towards higher potentials, increasing the reaction rate. Thus the observed current increases, while more material gets transported to the WE via diffusion due to an increasing concentration discrepancy between WE surface and bulk solution. Yet, at some point diffusion is not able to keep up with species consumption anymore and the concentration decrease at the surface of the WE leads to a reduced current increase (resulting in a less steep, albeit still positive slope). Eventually the decreasing concentration will lead to a net decrease in observed current, forming a characteristic peak. Further decrease in concentration at the WE surface then causes the current to approach a steady value. At this point, the concentration of reduced species at the WE surface is zero, since all new material transported by diffusion immediately reacts. This is called the diffusion-limited or mass-transport limited current.

After reversing the scan direction, the same effects can be observed for the reduction reaction. The schematic in figure 4.1 shows the symmetric cyclovoltammogram that can be observed under ideal conditions with a reversible redox active species present at equal concentrations of reduced and oxidised form.

Above considerations imply that the current measured is not only a function of the applied potential, but also has a time dependency. In a CV experiment, this time dependent aspect can be manipulated via the scan-speed. A faster scan-speed causes the peak current density to increase, because less time passes between the onset of the reaction and reaching the respective peak current potential. Thus, the concentration of reactant at the WE surface has not depleted as much. A concise description of this relationship is given by the Randles-Ševčík equation:[65]

$$I_{peak} = 0.4463\, nFAc \left(\frac{nFvD}{RT} \right)^{1/2} \tag{4.1}$$

Where I_{peak} = peak current, n = number of electrons exchanged, F = Faraday constant, A = electrode area, c = concentration of active species, v = scan speed, D = diffusion coefficient, R = universal gas constant and T = temperature.

A common treatment of experimental data is to plot I_{peak} vs $\sqrt{v}$, which can be used to gain information on the other variables in the equation, e.g. about D for known c, n, T and A.

Cyclovoltammetry can also yield a variety of information if a reaction deviates from 'ideal' conditions. E.g. for adsorption reactions, decomposition reactions, in situations where the forward reaction proceeds via a different mechanism than the reverse reaction (for example two one-electron reductions but one two-electron oxidation), etc.[65]

4.1.1 Membrane assisted cyclovoltammetry

For booster materials that are redox active, but not soluble in water and also not necessarily electrically conductive, a different setup was required, which is why in the course of this work an alternative setup for measuring CVs was developed. In order to establish contact of the booster both with the electrolyte and the electrode, a small amount of booster was soaked and submerged in the electrolyte solution and then squeezed between a glassy carbon electrode and a cation conducting membrane. This electrode-booster-membrane assembly was then used as the WE in an otherwise regular three-electrode setup. That way it was possible to investigate reactions otherwise inaccessible via cyclovoltammetry. However, one drawback of this method was that the unknown amount of contact between the solid analyte and the glassy carbon(GC)-electrode, which could change drastically at even a touch of the setup. Hence, calculating the current density or comparing the actual current values between experiments brought no advantage and thus all results are reported simply as the measured current vs potential and not as current density vs potential. These experiments were rather used to identify the electrochemical potential, at which the electron transfer occurred. This was deemed an acceptable trade-off for being able to investigate prospective booster materials without relying on their solubility or electric conductivity.

As shown in the schematic in figure 4.2, a three-electrode setup was constructed with an extra compartment for the WE, separated from the main compartment by a Nafion 117 membrane. The GC disc working electrode was pressed against this Nafion membrane with a small amount of potential booster material squeezed in between. Both compartments contained the same electrolyte solution. This allowed fixation of the material while simultaneously contacting it to the working electrode and the electrolyte solution. Crucially, the booster material to be tested in this setup does not need to be soluble in aqueous or organic solvents nor does it necessarily need to be electrically conductive. Results acquired using this setup can be found in section 5.2.

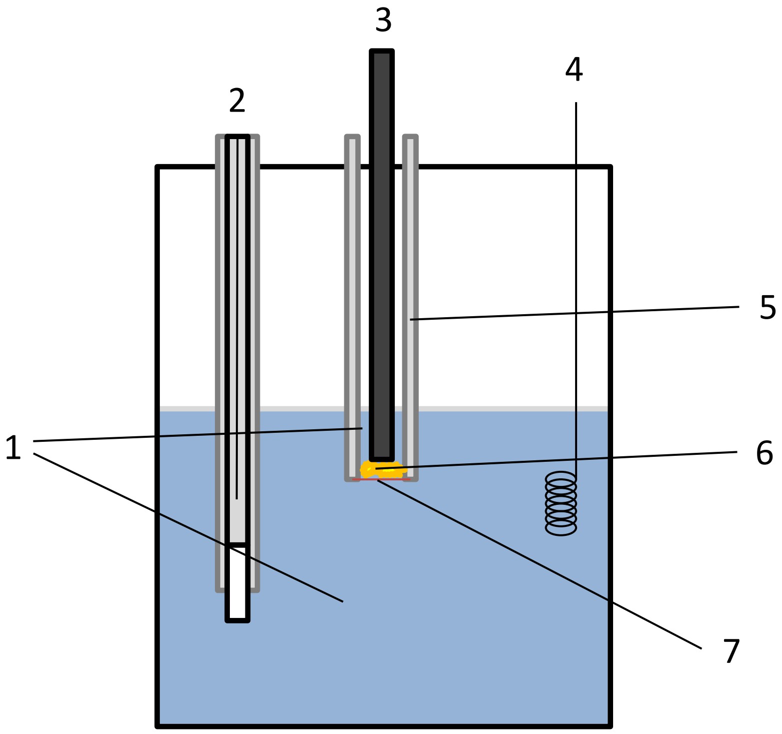

Figure 4.2 Schematic of the experimental setup for membrane-assisted cyclovoltammetry on prospective redox-active booster materials. While submerged in the electrolyte solution, the analyte was squeezed in between a cation-conducting membrane and the glassy carbon working electrode. (1) electrolyte solution, (2) reference electrode, (3) glassy carbon disc working electrode (3 mm diameter), (4) Pt-wire counter electrode, (5) polyethylene tube, (6) prospective booster material analyte, (7) Nafion 117 membrane. The reference electrode was either a Ag/AgCl in 3 M NaCl (209 mV vs. SHE) or a MSE in 1 M H_2SO_4, (674 mV vs. SHE) depending on the electrolyte solution used.

4.2 Chemicals

4.2.1 Booster materials and organic shuttle material

In order to gather electrochemical information on potential booster materials, their precursors or 'building blocks', as outlined in the concept in section 2.4.1 on page 14, were investigated first: The monomers containing the redox-active centre(s) were used in electrochemical experiments without having co-polymerised them with the linker monomer. The idea was to gain insight into the electrochemical properties and, if necessary, correct or alter the preceding synthesis before investing into the process of polymerisation. Although properties like the redox potential(s) might change in the final polymer, these changes were expected to be small, if any, due to the spatial distance between the redox centre(s) and the linking groups within the molecule.

Figure 4.3 shows the structure of 2,7-Bis(4-bromophenyl)benzo[lmn][3,8]phenanthroline-1,3,6,8(2H,7H)-tetrone. The redox active core of this molecule was of the group of naphthalenetetracarboxylic diimides (NDIs). NDIs are planar molecules that form stable radical anions upon reduction.[66]

Figure 4.4 shows the structure of a molecule from the family of the 10,15-dihydro-5,10,15-triaza-5H-tribenzo[a,f,k]triindenes (or triindoles), namely 5,10,15-Tris[2-(hydroxy)ethyl]-10,15-dihydro-5,10,15-triaza-5H-tribenzo[a,f,k]triindene, abbreviated as TAT-booster. Other derivatives based on a central triindole structure have been investigated elsewhere, confirming their redox activity and potential variability depending on substituents.[67–69] They generally can be oxidised reversibly, forming stable radical cations and further positively charged species in

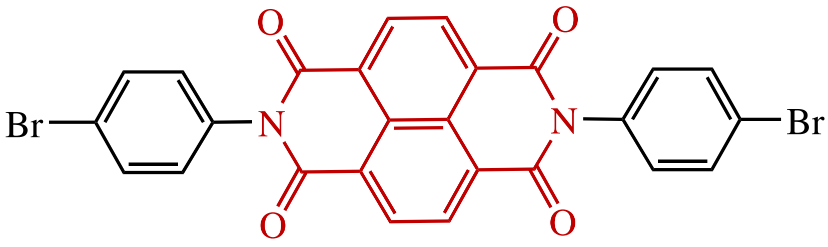

Figure 4.3 Precursor for a booster polymer based on a redox-active core (highlighted) of naphthalenetetracarboxylic diimide (NDI).

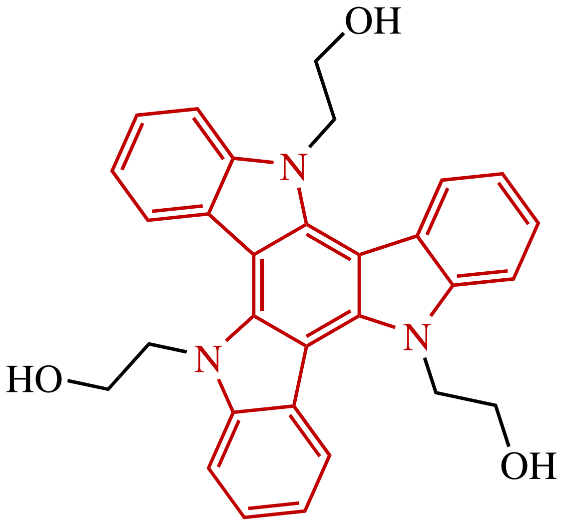

Figure 4.4 Precursor for a booster polymer derived from a redox active triindole core structure (highlighted).

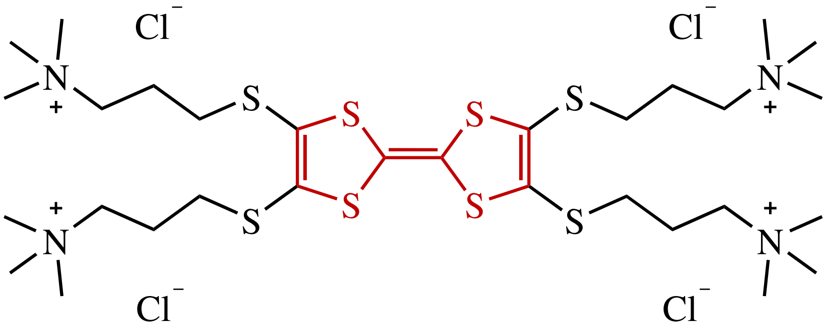

Figure 4.5 Redox shuttle based on a central tetrathiafulvalene unit (highlighted) with cationic sidechains to increase solubility in aqueous solutions.

the process.[68] Gámez-Valenzuela *et al.* found that the first reduction potentials in particular are heavily influenced by substituents on the outer benzene rings. Their research suggests that electron withdrawing groups can be used to decrease the electron density in the conjugated π-system, thereby increasing the redox potential and vice versa for electron donating groups.[69]

Unlike the other structures depicted here, the molecule in figure 4.5 was prepared as a shuttle material, rather than a booster. It was designed to be soluble in water and to carry charge between the electrochemical cell and the booster in the tank. The central structure is a tetrathiafulvalene, hence the

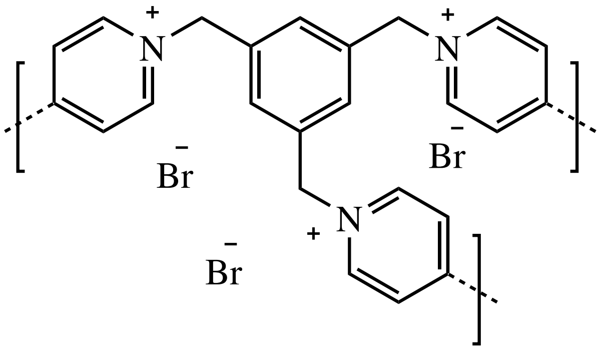

Figure 4.6 Structural unit of tris-Br, a booster polymer candidate based on a 1,3,5-tris(1-pyridyl)benzene. The redox activity is due to the bipyridinium-units created by the direct bond between two pyridnium rings in the polymer.

abbreviation as TTF-shuttle throughout this work. Tetrathiafulvalenes can undergo two reversible one-electron oxidations, forming first a stable radical cation and then the dication.[70] The stabilisation is facilitated by the molecule's symmetry, allowing for charge delocalisation, as well as the aromatic configuration caused by oxidation: The two dithiolylidene rings contain seven π-electrons each, which, upon oxidation, become six π-electrons per ring and thereby fulfilling Hückel's rule for aromaticity.

Apart from the experiments on booster precursors, two finished polymers were also tested as potential booster candidates. The structure shown in Figure 4.6 is based on a 1,3,5-tris(1-pyridyl)benzene, which is linked to the neighbouring units via the 4-position of the pyridinium rings. Figure 4.6 shows the bromide salt of the polymer (tris-Br), but the counterions can also be replaced, e.g. by chloride (tris-Cl). The theoretical capacity of the bromide salt is 136.01 mAh/g. The direct bond between two pyridinium rings forms a bipyridinium unit, which is responsible for the redox activity in this molecule, as shown in Figure 4.7. Unlike the previously discussed booster candidates, this polymer does not feature a rigid structure to enforce a hexagonal polymerisation. Instead, the -CH_2-groups between the central benzene ring and the three bipyridinium groups offer some flexibility.

The second tested polymer, AQ-tris, was based on a anthraquinone (AQ) redox active unit, combined with a linker of trifold symmetry (figure 4.8). Similarly to

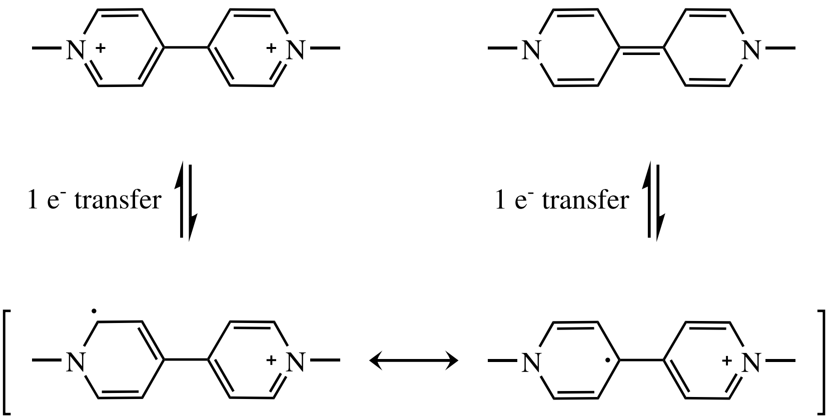

Figure 4.7 Bipyridinium redox chemistry

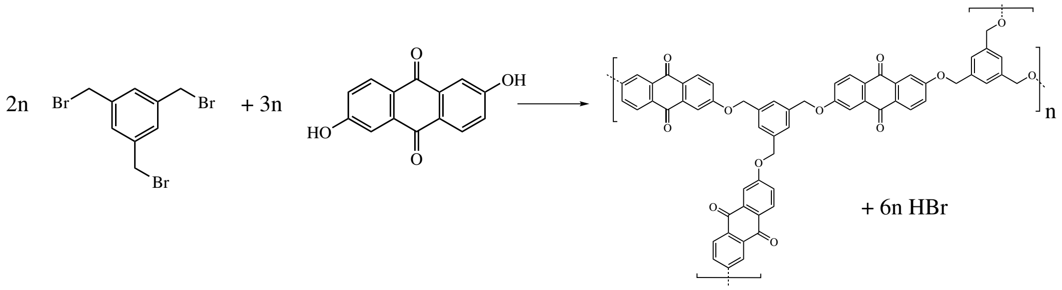

Figure 4.8 Anthraquinone based booster polymer and precursors.

tris-Br this polymer featured a non-rigid structure. In contrast, however, AQ-tris does not contain any formal charges in neither its oxidised nor reduced form (figure 4.9).

All five compounds shown in Figure 4.3, Figure 4.4, Figure 4.5, Figure 4.6 and 4.8 were designed and synthesised by Dr. Alan Wiles at the University of Glasgow. At later stages of this work, 1,1-dibromoferrocene (DBF) and ferrocene

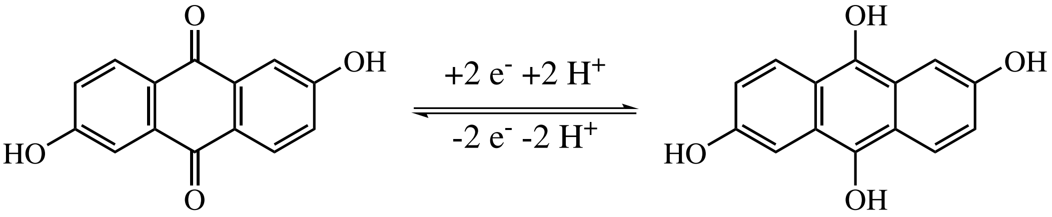

Figure 4.9 Redox activity of anthraquinone derivatives.

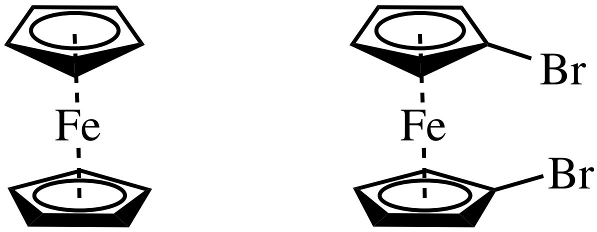

Figure 4.10 Ferrocene (left) and 1,1-dibromoferrocene (right).

were also used as booster materials. These were commercially purchased.

4.2.2 Synthesis of $[PV_{14}O_{42}]^{9-}$

PV_{14} was not commercially available and instead was synthesised as needed. The following synthesis route is a modification of a literature synthesis by Selling *et al.*[32] Unlike this literature synthesis, the route described here produces a sodium-free form of PV_{14}, using lithium as counter cation instead to increase the solubility of the product. Also, the final product is obtained as an aqueous solution and not a salt, as this is the form in which it was experimentally used anyway. Further modifications were introduced, including decreasing the amount of phosphate used. While in the synthesis from Selling *et al.* the excess phosphate was removed through a crystallisation step at the end, the solution obtained in the synthesis described here was designed to be used as is or diluted. The spare phosphate still present served to drive the equilibrium of the PV_{14}-formation reaction (from phosphate and vanadate) towards PV_{14} according to Le Chatelier's principle whilst used in a RFB system. During battery operation this was exploited to reform PV_{14} in case of decomposition, thus creating a 'self-healing' solution.[24]

$LiVO_3$ (254 g, 2.40 mol) was dissolved in hot deionised water (400 mL) until no solid particles were left. After cooling the transparent slightly yellow solution down to room temperature, concentrated H_3PO_4 (85% w/w, 41.0 mL, 0.600 mol) was added dropwise under vigorous stirring. Following this, concentrated aqueous HCl solution (37% w/w, 90.0 mL) was added to the now dark red solution, lowering the pH to about 2.00. The solution was stirred for ca. 2 hours during which the pH slowly rose. It was acidified to pH 2.25, again using

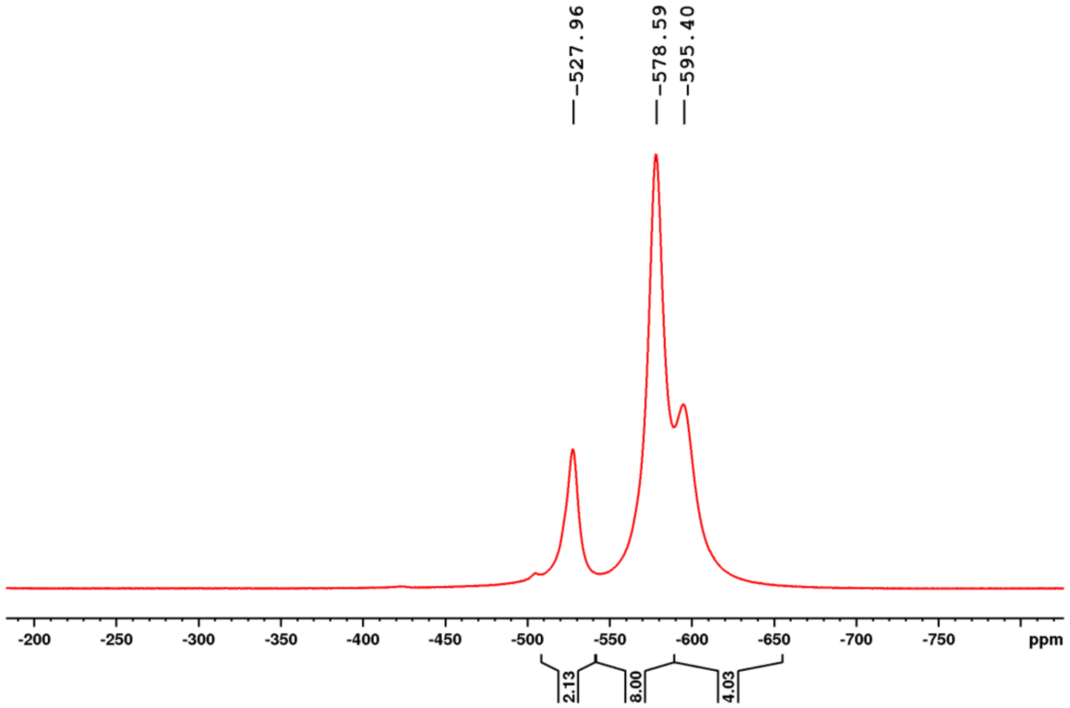

Figure 4.11 ^{51}V NMR (78.9 MHz, H_2O, 298 K) of Li-PV_{14} at 90 mM in pH 2.3

concentrated aqueous HCl solution (37% w/w, 8.00 mL). Now the solution was gently stirred overnight. The final pH adjustment was done on the next day with concentrated aqueous HCl solution (37% w/w) to reach a pH of 2.30.

The procedure described above yields a solution with a PV_{14} concentration of about 330 mM. The exact concentration of the final product may vary slightly due to water loss during the heating step (affected by boiling time, shape of vessel, etc.), but as the total vanadium content (and thus the amount of PV_{14}) of the solution was known, measuring the final volume allowed calculating the precise concentration.

Given enough time to equilibrate at pH 2.3 (one to two days), the conversion of vanadate to PV_{14} was near quantitative with only trace amounts of $[V_{10}O_{28}]^{6-}$ and VO_3^-, which are always present in a PV_{14} solution, see below.

^{51}V NMR measurements were conducted, confirming the vanadium to be present almost exclusively as PV_{14}. Figure 4.11 shows the three characteristic peaks of PV_{14}. Unlike the highly symmetric standard Keggin-structure, in which

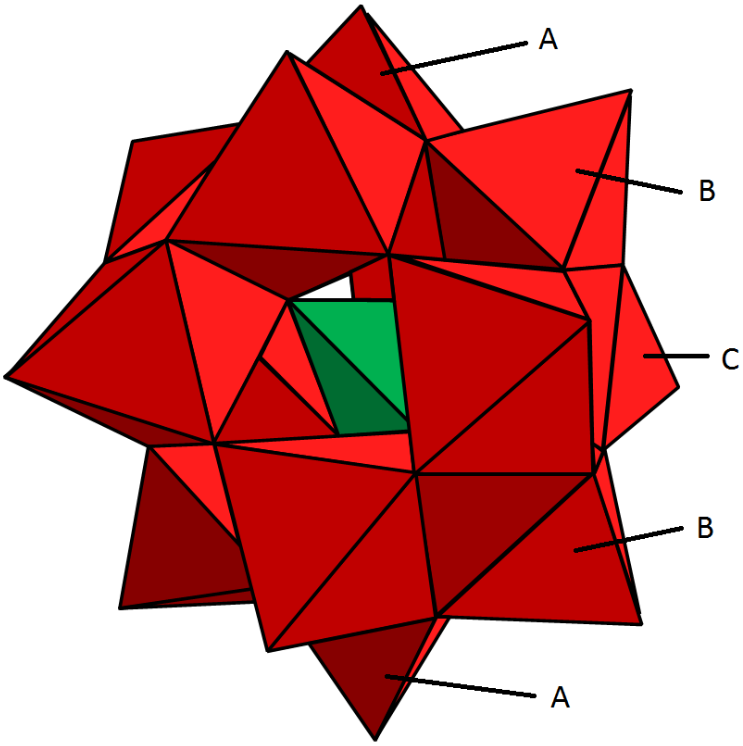

Figure 4.12 Polyhedral representation of the bicapped Keggin structure. Corners represent oxygen atoms with one vanadium atom at the centre of each red polyhedron and a phosphorus atom at the centre of the central tetrahedron. A, B and C represent the different vanadium positions.

all twelve framework atoms are chemically identical, the so-called 'bicapped' Keggin structure of PV_{14} has three distinctive positions of framework vanadium atoms. While the α-isomer of the Keggin structure has tetrahedral symmetry (point group T_d), its bicapped form's symmetry is reduced to D_{2d}. The thus ensuing framework vanadium atom positions are: The two opposing capping positions (position A), each with four adjacent vanadium atoms (position B), as well as the four vanadium atoms along the 'equator' of the molecule (position C), equidistant to the capping atoms (depicted in figure 4.12). In ^{51}V NMR, these species had distinct chemical shifts of -528 ppm (position A), -579 ppm (position B) and -595 ppm (position C), as shown in figure 4.11. The spectral data was in agreement with literature and the chemical shift of all three peaks varied with pH (compare figure 4.11 and 4.13), as has been reported before.[32]

The NMR spectrum also showed two minor other signals (at -424 ppm and

-505 ppm), which originated from a different vanadium-POM, $[V_{10}O_{28}]^{6-}$.[32] In an aqueous solution, it is not possible to purify the product further, as PV_{14} is subject to a pH-dependant chemical equilibrium with $[V_{10}O_{28}]^{6-}$ and VO_3^- [32]. The equilibrium reactions can be written as:

$$[PV_{14}O_{42}]^{9-} + 20\,H^+ \rightleftharpoons PO_4{}^{3-} + 14\,VO_2{}^+ + 10\,H_2O$$
$$[PV_{14}O_{42}]^{9-} + 6\,H_2O \rightleftharpoons {}_7\,[V_{10}O_{28}{}^{6-} + 5\,PO_4{}^{3-} + 12\,H^+$$

Figure 2.3 on page 13 shows that, even though PV_{14} is the dominating species under the given conditions at pH 2.3, there is also some $[V_{10}O_{28}]^{6-}$ as well as VO_3^- present. The ^{51}V NMR shown in Figure 4.11 was measured on a diluted sample (90 mM) of Li-PV_{14}. When recording ^{51}V NMR at higher concentrations of PV_{14}, such as the synthesised aqueous solution, the peaks tend to broaden so that the signals of $[V_{10}O_{28}]^{6-}$ can no longer be easily distinguished and eventually even the two signals of PV_{14} at -579 ppm and -595 ppm coalesce and form a single broad peak with a shoulder, as shown in the NMR in Figure 4.13, which was measured at 330 mM Li-PV_{14}.

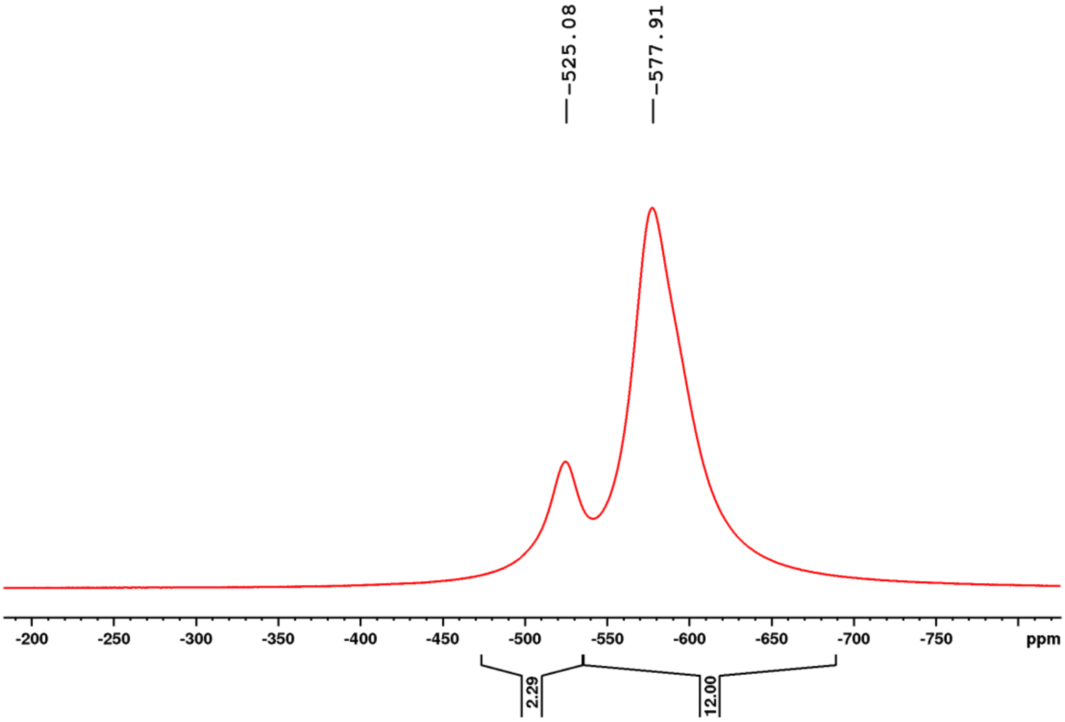

Figure 4.13 ^{51}V NMR (78.9 MHz, H_2O, 298 K) of Li-PV$_{14}$ at 330 mM in pH 2.3

Chapter 5

Solid state boosters for redox-Flow batteries

5.1 Measuring electrochemical properties of non-conductive, insoluble materials

There are a multitude of ways to measure and evaluate electrochemical properties, like for instance redox-potential(s), cycling stability or charge transfer resistance. Often, these experiments involve some form of solid-liquid interface between a working electrode and an electrolyte solution. For soluble materials, a solution of the analyte (and a supporting electrolyte) in a suitable solvent is measured. Alternatively, if the material is an insoluble solid, it can be used as the electrode and be investigated in this way. However, the latter method requires the material to be conductive.

The booster materials under investigation were by design solid and insoluble, but not necessarily conductive, which prevented either form of conventional investigation as described above. In the projected application, the booster material would reversibly react with a redox-active species in the electrolyte solution. Given sufficient porosity and wettability, good and uniform contact between the electrolyte and the booster material is enabled and conductivity should not be necessary for charge transfer. However, for initial investigations of the electrochemical properties of the booster material the lack of inherent conductivity posed a challenge. Since these investigations were necessary to build an understanding of how the booster material can be utilised, a solution was required.

5.1.1 Spin-coated and drop-cast samples on indium tin oxide slides

Initial samples of potential booster materials were received from Dr. Alan Wiles at the University of Glasgow either spin-coated or drop-cast as a thin film on small indium tin oxide (ITO)-coated glass slides. ITO is a transparent and conductive oxide which can be deposited as a thin film on glass substrates. Due to these properties, it can often be found in applications such as touch panels, solar cells and a vast variety of display technologies, such as liquid crystal displays.[71] In the applications described herein it was used for its properties as a hard, even and conductive substrate. A custom electrochemical cell was designed (figure 5.1), in which the ITO-slide could be integrated as the bottom of a small vessel. For electrochemical measurements, the vessel was filled with an electrolyte solution and equipped with RE and CE. The ITO was electrically contacted as the WE outside of the vessel, so that the bottom of the cylindrical cell served as the WE.

The cell (schematic in figure 5.2) consisted of a hollow PTFE cylinder in between a square stainless steel base plate and a square PTFE top plate, held together by nuts on four threaded bars. The drop-cast or spin-coated samples on the conductive side of a flat ITO-covered glass slide were placed on the base plate (sample/conductive side up), forming the bottom of the cell. A rubber seal was placed between the sample slide and the PTFE cylinder to prevent the electrolyte solution from leaking out. The PTFE top plate had openings for a Ag/AgCl reference electrode, a Pt-wire counter electrode and a small tube for N_2-purging (not shown in the schematic for clarity). The sample slide itself was contacted as the working electrode outside the cell.

However, after a number of experiments it became apparent that the redox activity of the ITO itself interfered with the measurements, particularly in acidic electrolytes. Specifically, H_2SO_4 (aq., 1 M) as the electrolyte produced a redox

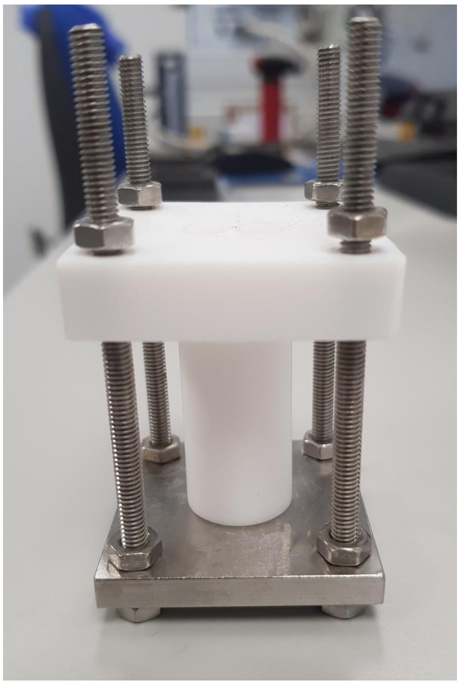

Figure 5.1 Custom-built cell for analysing potential booster materials on flat conductive sample-slides.

wave at around 620 mV vs SHE while HCl (aq., 1 M) caused a redox wave at around 0 V vs. SHE. Different electrolytes and pH-values were tested, e.g. LiCl, $NaClO_4$, etc. and compared to blank measurements with no booster material on the ITO slide but results were inconclusive. In order to rectify this, the experimental setup was redesigned.

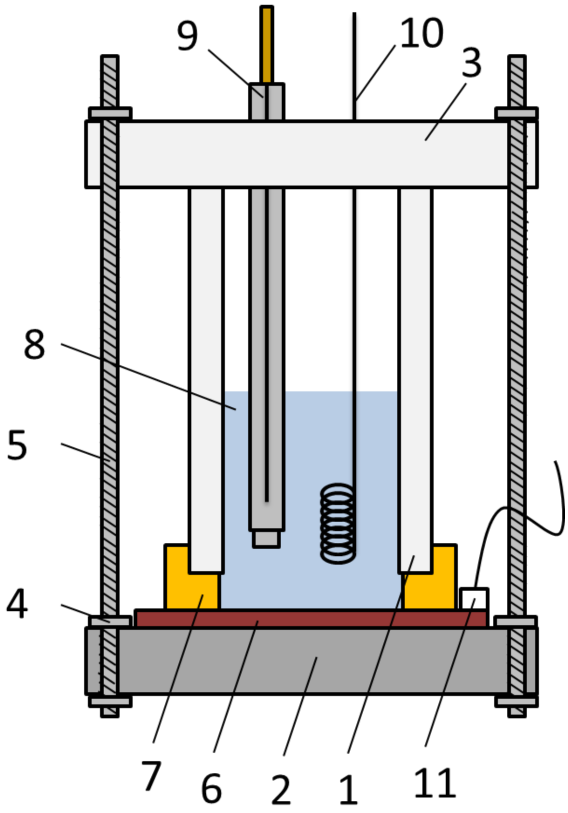

Figure 5.2 Schematic of the custom-built cell for analysing potential booster materials coated on a flat, conductive sample-slide. (1) PTFE cylinder, (2) stainless steel base plate, (3) PTFE top plate, (4) nuts, (5) threaded bars, (6) ITO-covered glass slide with sample (WE), (7) rubber seal, (8) electrolyte solution, (9) Ag/AgCl RE, (10) Pt-wire CE, (11) WE contact.

5.1.2 Drop-cast samples on carbon electrodes

Teachings from previous experiments were considered and it was decided that either the composition of the electrolyte solution had to be altered (e.g. higher pH) in order to suppress any unwanted redox reactions of the ITO or that the ITO substrate itself had to be replaced. Since the composition of the electrolyte solution also affects the behaviour of the booster material and in order to keep options open regarding electrolyte constituents, it was decided to replace the ITO substrate. GC was chosen as a redox-inactive (within reasonable potentials) and conductive substrate. In order to deposit the booster material to be analysed on the GC substrate, a suitable organic solvent was identified. The solvent had to dissolve the booster in sufficient quantities while being volatile enough to be evaporated quickly and at reasonably low temperatures to not damage the booster. Toluene was identified and selected as a suitable solvent for NDI, the booster material investigated here.

Small amounts of the booster were then dissolved in this solvent, drop-cast onto a glassy carbon electrode and the solvent evaporated. The resulting modified glassy carbon electrode could then be used as a working electrode in a standard three-electrode setup. However, CV measurements showed only capacitative currents. Even at scan speeds as low as 10 mV/s, no redox activity could be discerned in the potential range between -300 mV and +1200 mV vs. SHE. Since the amount of electrochemically accessible material was thought to be too small, a series of similar tests were conducted with NDI deposited on 1 cm x 1 cm pieces of carbon felt (CF) (Sigracell GFD 4.6, heat treated at 400 °C for 3 h in air) as this electrode material has a much higher surface area. These pieces were then connected via a gold wire and used as the WE in various electrolytes (LiCL, NaCl, KCl, 1 M each) and compared to blank measurements (carbon felt with and without exposure to toluene), but results were neither consistent nor reproducible (e.g. some redox-activity seemingly present in one electrolyte but not the other and then vice versa upon repeat measurements).

The other one of the two initially available booster material precursors, TAT, proved to be slightly soluble in ethanol. This opened up the possibility to dissolve samples of the material in Nafion solution (Sigma Aldrich, Nafion 117 containing solution, ~5 wt% in a mixture of lower aliphatic alcohols and water). Drops of the sample solution (1.2 µg TAT in 240 µL of ~5 wt% Nafion solution) were applied to a 5 mm diameter GC disc electrode (analogous to the attempts with NDI in toluene) and the solvents evaporated. This resulted in a GC electrode modified with TAT in an ion conducting matrix of Nafion.

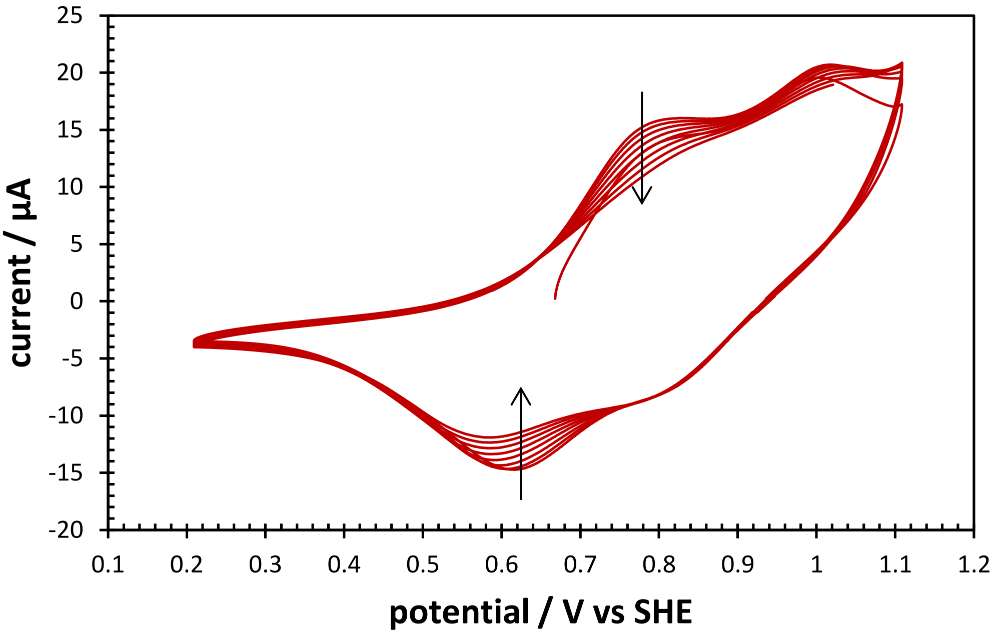

Figure 5.3 CV of TAT in a matrix of Nafion on a 5 mm diameter GC disc WE showing a reducing current response in consecutive cycles. CE: Pt-wire, RE: Ag/AgCl in 3 M NaCl (209 mV vs. SHE), electrolyte: 1 M $NaClO_4$, scan speed: 10 mV/s.

Figure 5.3 shows an example of the resulting CVs of TAT in 1 M $NaClO_4$ at 10 mV/s. While this approach seemed suitable to gauge oxidation (ca. 800 and 1010 mV vs. SHE) and reduction (ca. 620 and 840 mV vs. SHE) potentials, it can also be seen that the peak current decreased with every consecutive cycle. This might have been due to particles of the booster material detaching from the electrode as a result of the material being repeatedly oxidised and reduced. It should be noted that, from a thermodynamic perspective, at neutral pH OER can occur starting from ca. 820mV vs. SHE. However, the observed current at the peaks at 0.8 V and 1.0 V vs. SHE decreases again after the respective peaks which would likely not be the case for OER. The same can be said for the possibility of carbon oxidation (of the GC-electrode).

Comparing results from the NDI and TAT experiments described here it seems possible that the (hydrophobic) layer of NDI impeded ion movement to and fro the active material whereas the mixed in Nafion polymer in the TAT experiments allowed for it, potentially explaining why redox activity could only be observed with the polymer present.

Another shortcoming of this method was its reliance on a minimum solubility of the material to be analysed in a solvent (here: TAT in ethanol). For other potential booster materials, in particular the target polymers to which TAT and NDI are merely precursors as described in sections 4.2.1 and 2.4.1, there might be no suitable solvent. Consequently, the approach to reliably analyse prospective booster materials needed to be further refined.

5.2 Membrane-assisted cyclovoltammetry

To mitigate the reliance on solubility, the method of acquiring electrochemical information about prospective booster materials was developed further. In order to more accurately represent the circumstances found in the projected application of the booster, such as direct contact of the booster with the electrolyte solution, an improved setup for measuring CVs was designed that allowed for prospective booster materials to be analysed without relying on their solubility or electric conductivity. A schematic of the experimental setup (figure 4.2) is given in section 4.1.1 on page 31, alongside further experimental details on this method of membrane-assisted cyclovoltammetry.

A selection of the CVs acquired with this method is shown below. Specifically those of ferrocene (figure 5.4 and 5.5), DBF (figure 5.6), tris-Br, (bromide salt of a 1,3,5-tris(1-pyridyl)benzene-based booster material) (figure 5.7) and AQ-tris (figure 5.8), as these materials are further investigated in the following sections. With this setup, it was possible to investigate different boosters in various electrolyte solutions, making it a suitable standard method for this thesis and other works that target the same concept.

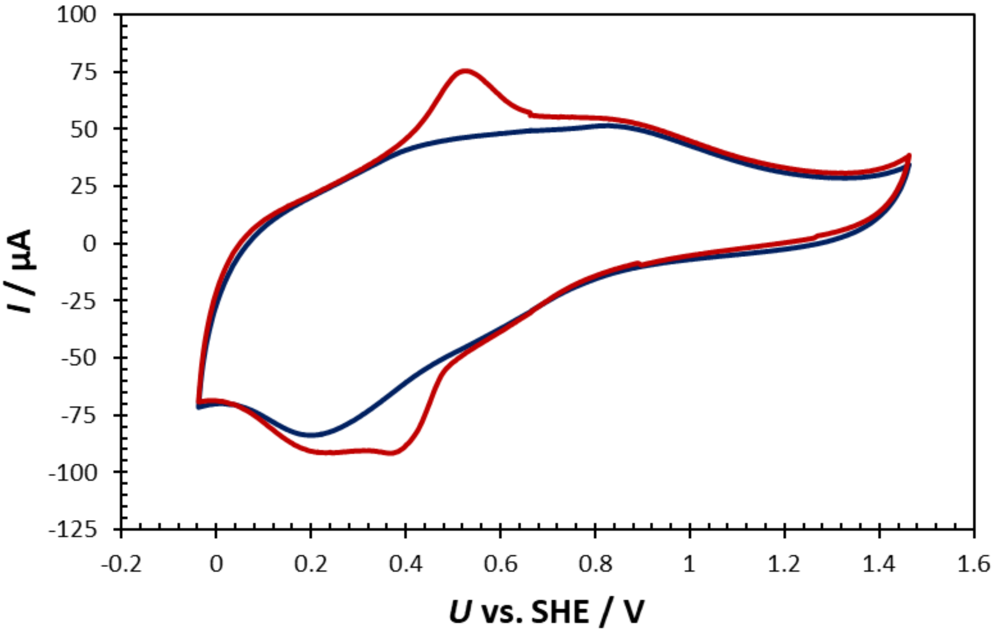

Figure 5.4 Membrane CV of ferrocene in 1 M H_2SO_4 (red) and blank measurement in 1 M H_2SO_4 (blue). WE: GC-disc, CE: Au-wire, RE: MSE (1 M H_2SO_4), scan speed: 100 mV/s.

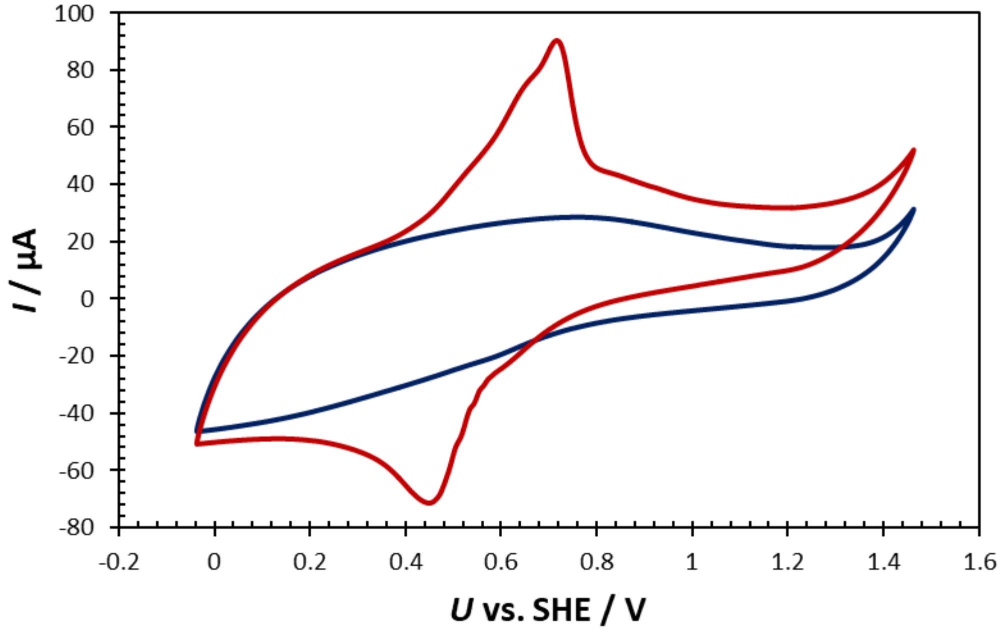

Figure 5.5 Membrane CV of ferrocene in 3 M NaCl (red) and blank measurement in 3 M NaCl (blue). WE: GC-disc, CE: Au-wire, RE: Ag/AgCl (3 M NaCl), scan speed: 100 mV/s.

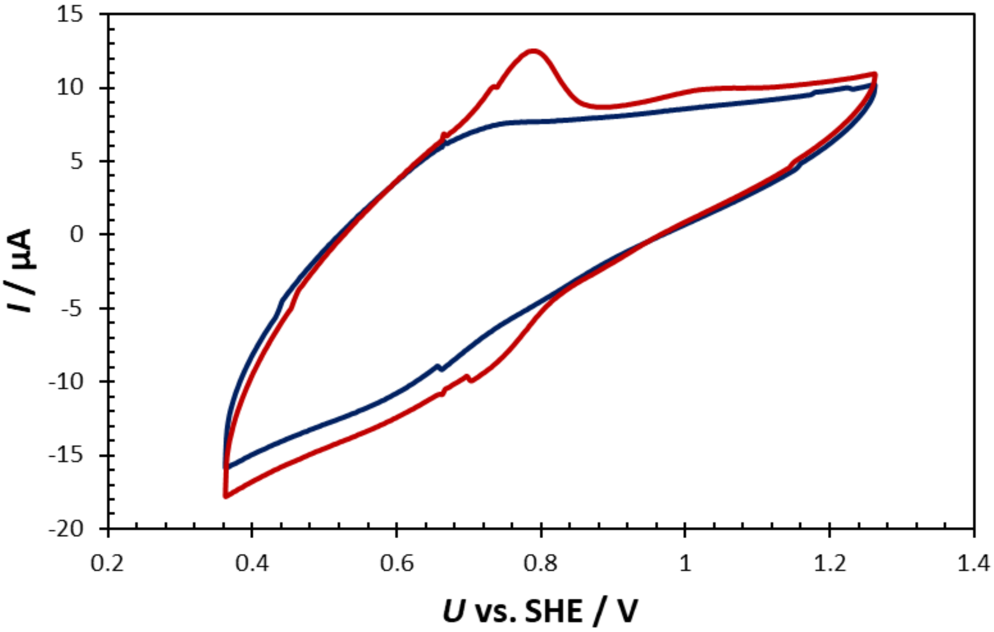

Figure 5.6 Membrane CV of 1,1-dibromoferrocene in 1 M H_2SO_4 (red) and blank measurement in 1 M H_2SO_4 (blue). WE: GC-disc, CE: Pt-wire, RE: MSE (1 M H_2SO_4), scan speed: 100 mV/s.

The standard reduction potential of ferrocene is 0.64 V vs. SHE [72], which agrees with figure 5.5. While the reaction is not proton-coupled (oxidation of ferrocene, Cp_2Fe, yields the cation Cp_2Fe^+), it is possible to protonate Cp_2Fe to form $[Cp_2FeH]^+$ by exposing it to strong acids [73, 74], which is potentially the reason for the different redox potential observed in the CV in figure 5.4, which was measured in 1 M H_2SO_4.

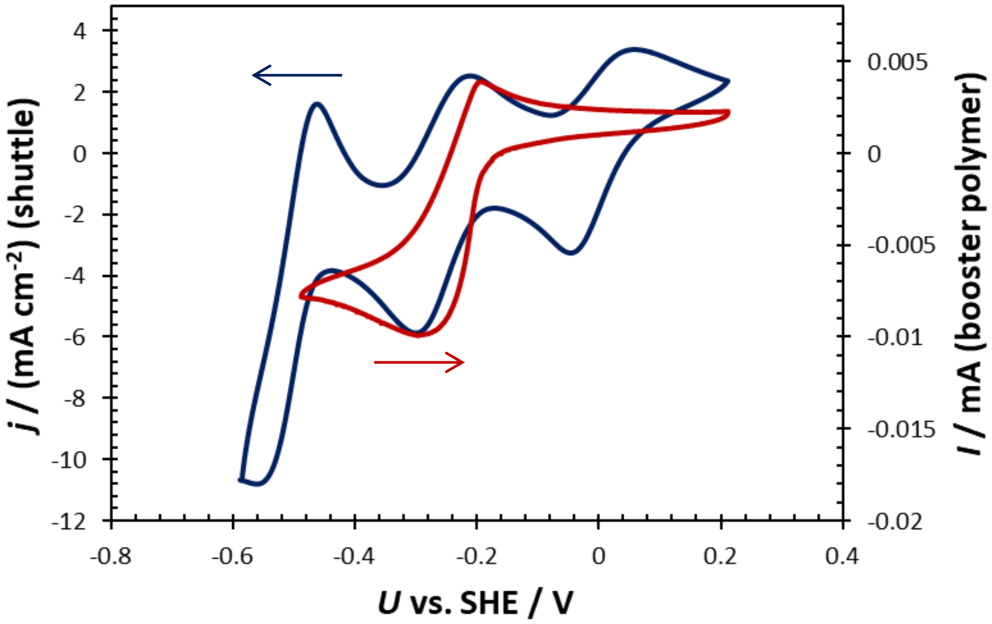

Figure 5.7 CV of SiW_{12} (10 mM in 1 M LiCl, left abscissa, blue trace) compared to membrane CV of tris-Br (in 1 M LiCl, right abscissa, red trace). WE: GC-disc, CE: Pt-wire, RE: Ag/AgCl (3 M NaCl), scan speeds: 100 mV/s (SiW_{12}) and 20 mV/s (tris-Br).

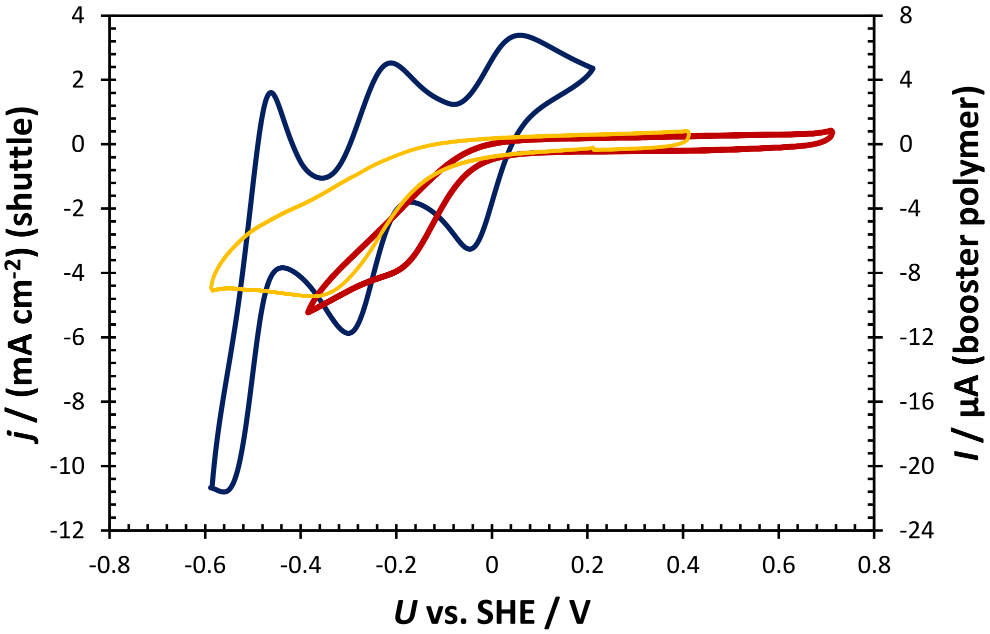

Figure 5.8 CV of SiW_{12} (10 mM in 1 M LiCl, left abscissa, blue trace) compared to membrane CVs of AQ-tris in 1 M LiCl (right abscissa, red trace) and in 1 M LiCl acidified with several drops of 6 M aqueous HCl (right abscissa, yellow trace). WE: GC-disc, CE: Pt-wire, RE: Ag/AgCl (3 M NaCl), scan speeds: 100 mV/s (SiW_{12}) and 20 mV/s (AQ-tris).

Depending on the pH, the third redox wave of SiW_{12} can be located very close to the onset of HER (compare figure 6.9 on page 106, showing CVs of SiW_{12} at different pH values as well as the respective onsets of HER). The lower vertex potential of the SiW_{12}-scan in figure 5.7 and 5.8 was chosen as shown due to the steep drop typical for HER appearing directly after. However, the actual onset of this HER-wave overlaps with the shown reduction wave of SiW_{12}, explaining why the reduction peak of this third wave is larger than the corresponding oxidation peak. The overall net negative current for this CV of SiW_{12} (note the level of the zero-current line) is due to the fact that this CV was recorded using a solution of fully oxidised SiW_{12}.

5.3 Testing a tetrathiafulvalene derivative as organic shuttle

Amongst the initial ideas for this project was the plan to use an organic shuttle to transport the electrons between booster and electrochemical cell. Small alterations to the structure introduced by modifying the synthesis of this organic redox shuttle would then allow optimising the system by specifically influencing its redox potential(s) and matching them to those of the booster material. Also, organic shuttle materials, since they usually comprise only earth abundant, cheap elements, are theoretically much less expensive than inorganic shuttle materials, such as V, where the world market price of the raw material sets a lower limit for how cheap it could be made. However, as discussed in section 3.2, many organic materials undergo side reactions when cycled, so preventing or suppressing those and monitoring cycle stability was of special concern.

One material synthesised by Alan Wiles in Glasgow for the use as such an organic shuttle was the tetrathiafulvalene derivative shown in section 4.2.1. While it was possible to measure the reduction potential (U) of the TTF-shuttle in aqueous solutions, it also became apparent that the measured current in a CV constantly decreased over consecutive cycles, indicating an irreversible decomposition process. The material safety data sheet for tetrathiafulvalene, the redox active core of the TTF-shuttle, states that the compound is both light sensitive and air sensitive.[75] This suggests that the same is likely true for the TTF-shuttle used here. It was soon noticed that the TTF-shuttle indeed seemed sensitive to light. Figure 5.9 shows two CVs of the same solution, 4 mM TTF-shuttle in 1 M LiCl. One was measured with the freshly prepared solution (from the TTF-shuttle as a powder) and the other one after 16 days, during which time the solution was stored in an airtight but transparent container on a shelf in the laboratory.

While light sensitivity is hardly a concern in the target application (tubes, tanks and cells in applications bigger than testing equipment tend to be made from non-transparent materials anyway), it presents an additional layer of complexity in a laboratory environment. Generally, the possibility of degradation or side reactions in organic materials is a significant concern, which applies to prospective

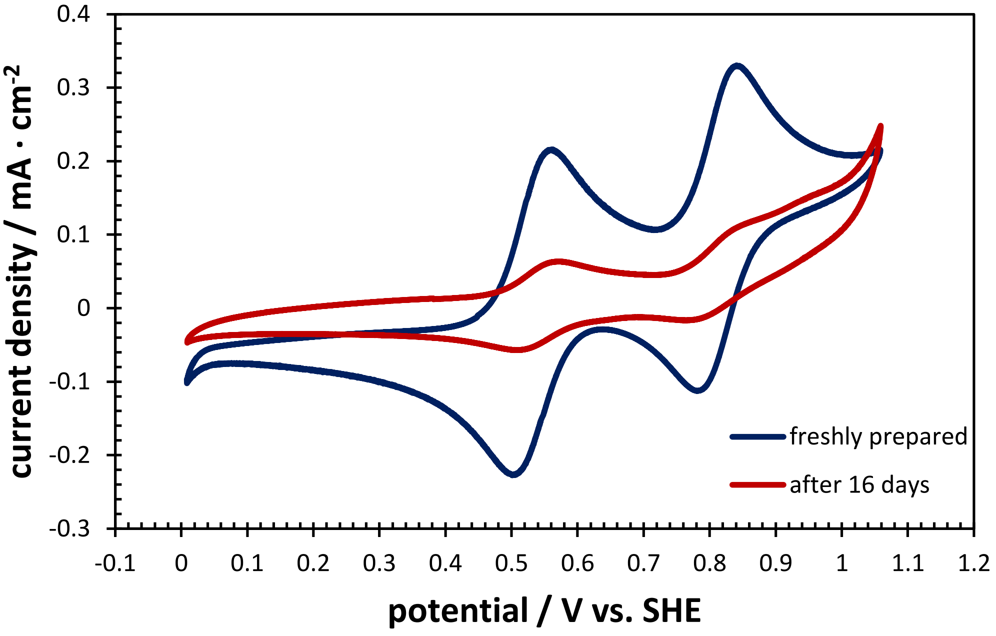

Figure 5.9 CVs of 4 mM of the TTF-shuttle in 1 M LiCl freshly prepared (blue) and measured again under the same conditions 16 days later (red). WE: GC disc, CE: Pt-wire, RE: Ag/AgCl in 3 M NaCl (+209 mV vs SHE), scan speed: 100 mV/s.

booster as well as shuttle materials. As the investigation of possible booster materials was considered the primary objective of this project, it was decided to prioritise research on them. Rather than pairing them with organic shuttle materials, thereby introducing more experimental parameters and potentially uncertainties in the evaluation of results (e.g. whether an observed instability originates from the booster or the shuttle), it was decided to test said boosters alongside already known inorganic shuttle materials and not use organic materials for the purpose of acquiring a proof of concept.

5.4 Shuttle absorption by booster material

During earlier stages of this project, full cell tests were conducted using a PV_{14}-SiW_{12} POM-RFB as described in [24] and appendix B. The standard reduction potential of tris-Br determined by membrane cyclovoltammetry overlaps well with the second redox wave of SiW_{12}, as shown in figure 5.7 in section 5.2. Thus, in theory SiW_{12} should be able to oxidise and reduce tris-Br (depending on its oxidation state). To test this, a PV_{14}-SiW_{12} POM battery was constructed containing tris-Br in the anolyte tank as a coarse powder suspension (as a form of a packed-bed reactor). A filter at the outlet of the tank prevented the booster from being sucked out of the tank and circulating through the system. The catholyte consisted of a pre-reduced PV_{14} solution in vast excess to exclude capacity limitations from the half-cell that did not contain a booster.

This experiment produced results that were initially thought to hint at some decomposition of the SiW_{12}, as charge and discharge plateaus shifted during the initial cycles and the total capacity dropped considerably before stabilising.

Furthermore, earlier variants of the experiments described in section 5.5 were performed, also employing tris-Br and SiW_{12}. Again, results pointed at some loss mechanism of SiW_{12} during initial cycling to equilibrate the system. It was suspected that the SiW_{12} might have been absorbed by the employed tris-booster. To test this, two identical solutions (2 mM SiW_{12}, 1 M LiCl, pH 1.74, 30 mL) were prepared. To one of the solutions tris-Br (100 mg) was added before sealing them and stirring them both for five days to ensure the systems were in equilibrium. Afterwards, the solutions were left to settle so that the booster sank to the bottom of the vessel and CVs were recorded on both solutions (figure 5.10)

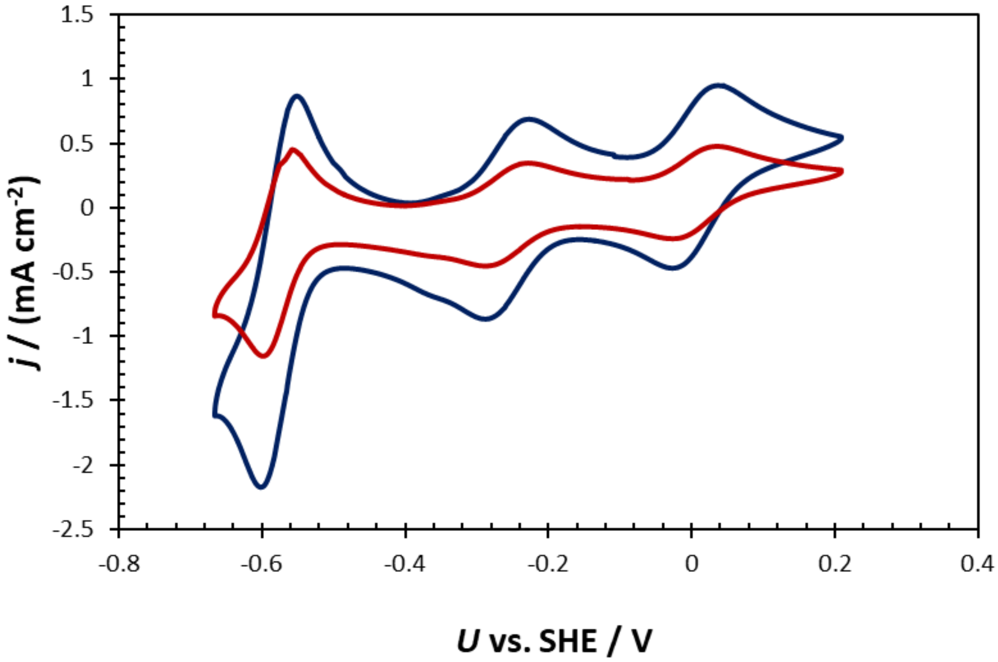

Figure 5.10 CVs of SiW_{12} solutions (2 mM in 1 M LiCl, pH 1.74, 30 mL each) with (red trace) and without (blue trace) exposure to tris-Br booster (100 mg) for five days. WE: GC-disc, CE: Pt-wire, RE: Ag/AgCl (3 M NaCl), scan speed: 500 mV/s

The peak current (I_{peak}) is directly proportional to the concentration (as described by the Randles-Ševčík equation, eq. 4.1 on page 29), which is the only different variable between the measurements shown in 5.10, since both measurements used the same experimental setup and electrochemically active species. Hence, the solution containing the booster has had a lower concentration of SiW_{12}. This supports the previous hypothesis of the SiW_{12} being absorbed by the tris-Br booster.

In a strict sense, the Randles-Ševčík equation only applies to one individual redox event and not to systems with multiple consecutive redox events. SiW_{12} exhibits multiple electron transfers and was present in its fully oxidised state, so diffusional effects could be expected in the resulting CVs. To minimise those effects, a fast scan rate of 500 mV/s was chosen. Thus, calculating the height for the individual redox waves (as total peak-to-peak current difference between anodic and cathodic wave, i.e. $I_{peak}(Ox) - I_{peak}(Red)$) and comparing those for both solutions should still give a reasonably accurate value for the concentration loss in the solution with booster. Specifically, $I_{peak}(Ox) - I_{peak}(Red)$ for the red trace (with booster) in figure 5.10 was 49% smaller compared to the blue trace (no booster) for the first electron wave (most positive potential) and 49% and 47% smaller for the second and third redox wave, respectively. This means that the concentration of SiW_{12} of the solution with booster was approximately halved compared to the original 2 mM solution with the rest of the SiW_{12} absorbed in the booster.

This absorption can be explained when considering the molecular structure of the booster. In its fully oxidised form, as shown in figure 4.6 in section 4.2.1, the tris-Br booster has three positive charges per unit structure. SiW_{12}, on the other hand, is always present as an anion in solution. Even in its fully oxidised state, the overall charge of the molecule is -4. POMs are also known to precipitate when combined with large cations[76] so it seems reasonable that Coulombic attraction with a positively charged booster polymer would also cause it to precipitate and combine with the booster.

In this experiment only approximately half of the shuttle material got trapped in the booster. However, in the envisioned application, the booster would be present in vast excess and so any absorption of shuttle material would most likely render the battery useless. Consequently, it was decided to also take molecule charges into consideration when selecting prospective booster-shuttle combinations. This means opposite charges of booster and shuttle were sought to be avoided in both discharged and charged battery state.

5.5 Bulk electrolysis and booster cartridge experiments

To avoid unwanted Coulombic attraction between booster and shuttle, an alternative booster material was chosen: AQ-tris, a polymer based on the redox active anthraquinone and a trifold linker, as detailed in section 4.2.1. AQ-tris does not feature a formal charge on the molecule in neither its oxidised nor reduced form, shown in figure 4.9 on page 35. This should prevent any absorption based on Coulombic attraction with the shuttle material. It is also not anionic, so Coulombic repulsion with the anionic SiW_{12} is not an issue. Membrane CVs of this material (figure 5.8 on page 52) showed a broad reduction peak, overlapping with the second redox wave of SiW_{12}, indicating that SiW_{12} should be able to transfer electrons to this booster.

In order to detect any redox-interaction between the booster and the electrolyte, a special experimental setup was developed, consisting of two different electrochemical cells.

The first cell was a bulk electrolysis (BE)-cell (figure 5.11), consisting of a glassy GC mesh WE, a Ag/AgCl RE (in 3 M NaCl, separated from the main compartment by a frit) and a Pt-wire CE (in 1 M Li_2SO_4, separated from the main compartment by a Nafion 117 membrane, pH matched to the main compartment solution). The cell was also equipped with a GC disc WE (3 mm diameter) for measuring CVs, a magnetic stirrer with stirring bar and purged throughout the experiment with humidified nitrogen, to avoid air oxidation. Additionally, the complete setup was placed in a small nitrogen-purged benchtop glovebox, shown in figure 5.12. The experiments involving this benchtop glovebox described in this section were conducted at the University of Glasgow with assistance of Dr. Alan Wiles.

This BE-cell was used to manipulate the oxidation state and thus the electrochemical potential of an electrolyte. Through two individual channels (as shown in figure 5.11), this electrolyte could be pumped through the two half-cells of the second electrochemical cell (depicted in figure 5.13, a 1 cm^2 - flow cell (C-Tech, C-Flow LAB 1×1)), circulating back to the bulk electrolysis cell using a peristaltic pump. The cell was equipped with two 1 cm x 1 cm pieces of carbon felt (Sigracell GFD 4.6 EA, heat treated at 600 °C for 3 h in air) per half-cell and a Nafion 117 membrane as the separator.

Additionally, both electrolyte channels were fitted with a booster cartridge each (depicted in the schematic in figure 5.13 and shown on the picture in figure 5.14), placed before the flow-cell, forming a symmetrical setup. These booster cartridges contained a fitted piece of carbon felt, acting as a filter to allow

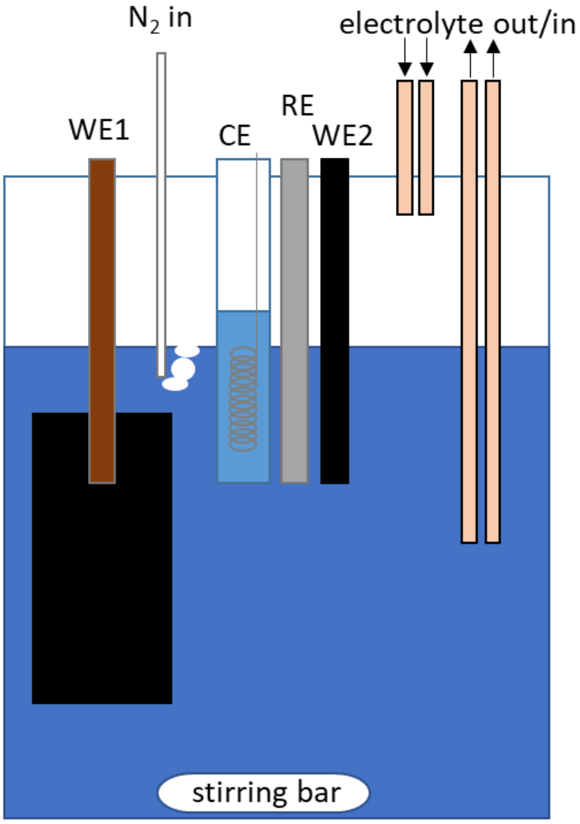

Figure 5.11 Schematic of the BE-cell used to manipulate the oxidation state of the active material (shuttle material) in the electrolyte. The two electrolyte channels were connected via pumps to the booster cartridges (figure 5.14) and further to the OCV cell (schematic in figure 5.13). WE1: GC mesh; WE2: GC disc (3 mm diameter); CE: Pt-wire in 1 M Li_2SO_4, separated from the main compartment by a Nafion membrane, pH matched to main compartment solution; RE: Ag/AgCl in 3 M NaCl. The vessel was closed and purged with humidified nitrogen throughout every experiment. Additionally, the whole setup was placed inside a nitrogen-purged benchtop glovebox (photo in figure 5.12) to minimise air oxidation.

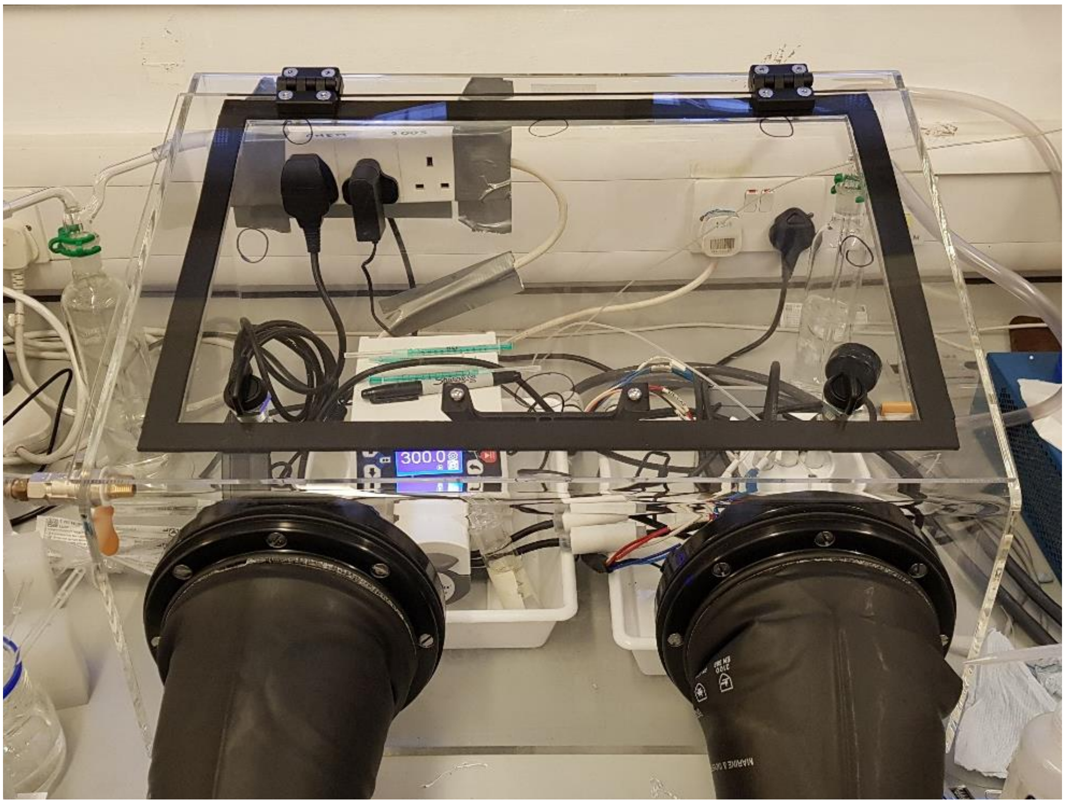

Figure 5.12 Photo of the BE-setup with OCV cell in a nitrogen purged benchtop glovebox. Early version of the booster cartridges visible between glove-openings.

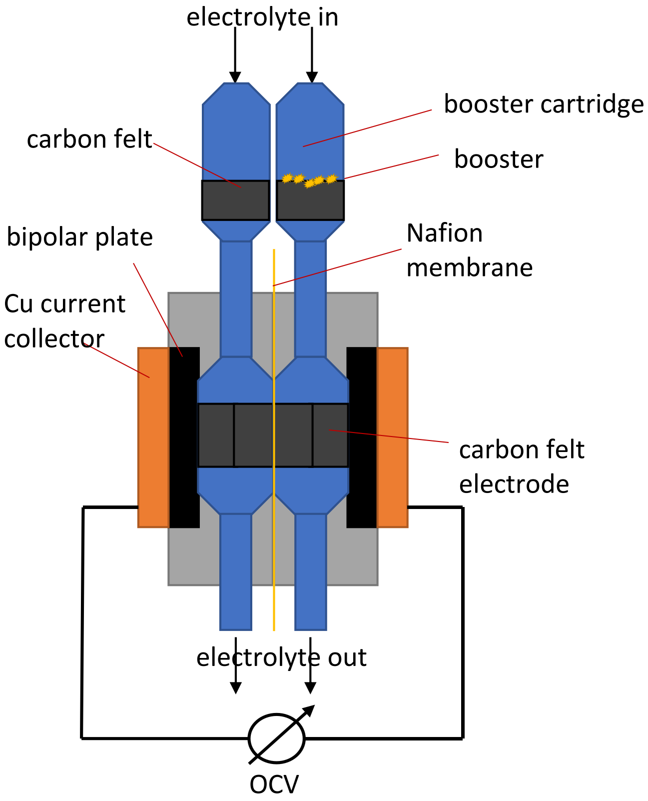

Figure 5.13 Schematic of the booster cartridges connected in series with the 1 cm^2 flow-cell used to measure the OCV between the two electrolyte streams. The two electrolyte channels were connected via pumps to the BE-cell depicted in figure 5.11.

the electrolyte to flow through but keeping the powdered booster material in place. The small flow-cell directly behind the cartridges was used to constantly monitor the difference in U (the open circuit voltage (OCV)) between its two half-cells. For the experiments, a sample of the booster material was added to one of the cartridges, while the other one was left empty. This was done to keep the setup symmetrical and to ensure equal length pathways for both channels. Experiments were also conducted where the booster had been mixed with a conductive additive (carbon black, 30 wt.%).

The electrochemical potential for each of the half-cells is governed by the ratio of the oxidised to the respective reduced species of the electrolyte via the

Figure 5.14 Booster cartridges with connectors for tubing and fitted pieces of carbon felt to retain the booster material during experiments.

Nernst-equation (equation 2.1, page 17). All other symbols in the equation represent constants or parameters which have equal values for both half cells, since the same electrolyte from the same reservoir was being used. Consequently, if the ratio of oxidised to reduced species was the same in both half cells of the flow-cell, then their potentials would also be the same and thus the OCV would be 0 V.

The experiments were started with both the booster and the electrolyte in their respective fully oxidised states. In this situation, there could be no electron exchange between the booster and the electrolyte. Since the electrolyte flowing through both half-cells stemmed from the same reservoir, the OCV was expected to be 0 V. While continuously pumping the electrolyte through the flow-cell, its ratio of oxidised to reduced species was manipulated by applying a current to the bulk electrolysis cell. When the fully oxidised form of the electrolyte was reduced, its concentration of the oxidised species (c_{Ox}) decreased at the same rate as concentration of the reduced species (c_{Red}) increased. As long as no reaction between the booster and the electrolyte occurred, the OCV measured in the flow-cell should still be unchanged, since the same ratio of oxidised to reduced species was supplied to both half-cells.

However, once the electrolyte (starting from its fully oxidised form) was sufficiently reduced, a reaction could be expected between the electrolyte and the booster, oxidising the former and reducing the latter, thereby changing the ratio of oxidised to reduced species in the electrolyte and thus its electrochemical potential. The measured potential was an average across the entire volume of the carbon felt electrode. A larger electrode means the potential is averaged over a larger volume of electrolyte and therefore over a wider time window (in terms of when the electrolyte now in the flow-cell was extracted from the BE-cell, since it was pumped at a constant rate). For a potential change to be more pronounced, it was therefore important to maximise the electrolyte volume flow per electrode area. Hence, a relatively small flow-cell was needed with a high flow of electrolyte, which is why the 1 cm x 1 cm flow-cell was chosen.

Since this reaction occurred in only one of the two electrolyte streams before they reached the flow cell, the measured OCV in said flow cell was expected to deviate from zero, indicating that a redox reaction between the booster and the electrolyte took place.

However, since c_{Ox} and c_{Red} change in a linear fashion (constant current in the bulk electrolysis), but the potential is determined by the logarithm of the ratio $\frac{c_{Ox}}{c_{Red}}$, the influence on the potential will be strongest at very high and very low values of $\frac{c_{Ox}}{c_{Red}}$. E.g. if 99% of the electrolyte is in its oxidised form (and 1% in the reduced form) and 1% of the total electrolyte gets reduced (so that 98% is now oxidised and 2% reduced), the Nernst equation (equation 2.1, page 17) predicts a change in potential by 18 mV for a one-electron reaction at 20 °C. In contrast to that, if the starting conditions are 50% oxidised form and 50% reduced form and again 1% of the total electrolyte gets reduced, the Nernst equation predicts only a 1 mV change in potential. This means that larger potential differences were expected for when a difference in oxidation state between the two half cells occurred while the electrolyte was either almost fully oxidised or almost fully reduced (in the case of an electrolyte with only two potential oxidation states). For the general case of an electrolyte with more than two possible oxidation states (as is the case with POMs and discussed at length in chapter 6), this definition can be extended as follows: Larger potential differences in the measured OCV can be expected whenever a difference in reduction degree between the two half cells occurred while the average oxidation state of the electrolyte was close to an integer value. In other words, the magnitude of the OCV was not expected to be proportional to the reaction rate between booster and shuttle, but rather a qualitative indication of when (in terms of the average oxidation state/the electrochemical potential of the shuttle) a reaction between the booster and the shuttle occurs.

However, for this setup, one additional cause for the OCV deviating from 0 V was conceivable: Even though a considerable effort was put into creating a symmetrical setup, minor deviations in flow rate between the two channels could not entirely be avoided. This means that if one channel has a slightly faster flow rate than the other, the electrolyte taken from the reservoir of the BE-cell reaches the respective half-cell of the flow-cell slightly earlier than its counterpart in the other channel taken from the reservoir at the same point in time. Thus, when reducing the electrolyte in the BE-cell at a constant rate while continuously pumping, the faster-flowing side of the flow-cell would always be slightly ahead in terms of reduction degree, consequently having a lower electrochemical potential and vice versa during oxidation.

For the most part, a slight imbalance in flow speed while pumping and electrolysing the solution in the BE-cell would manifest itself in a small bias in the OCV cell with sharp spikes when the average oxidation state of the electrolyte nears an integer value.

With two potential causes for the OCV deviating from 0 V arose the necessity to distinguish between the two, for only one of them was attributed to a reaction between the shuttle and the booster.

In order to do so, blank measurements were conducted, where no booster was added to the system, i.e. both cartridges were left empty.

The bulk electrolysis procedure was performed so that the SiW_{12} was reduced stepwise to ideally see the point where the booster becomes active. From the starting reduction degree of SiW_{12} of 0 it was reduced first to -1 (i.e. reduced by one electron per molecule of SiW_{12}) and then reoxidised to 0. After this, the following reduction degrees were targeted: -1, -2, -1, -2, -4, -2, -1, 0.
Each reduction and oxidation step was performed as constant current/constant potential (CCCP) operation. The charge limit for each step was set to 90% of the theoretical maximum capacity per electron of the SiW_{12} present in solution or when the current had dropped to 10% of the maximum current. The maximum current for both, oxidation and reduction, was set to 50 mA and the potential limits were selected to be in between the redox waves of the respective redox couples, determined using CV of SiW_{12} at the respective pH, as shown in figure 5.15.

Figure 5.16 and 5.17 show results for 200 mL 2.5 mM SiW_{12} (theoretical capacity: 13.4 mAh per used electron, i.e. a reduction of 1 F mol^{-1} corresponds to 13.4 mAh) in 1 M LiCl at around pH 2 for a blank measurement and a measurement using AQ-tris (39.5 mg mixed with 16.9 mg carbon black; theoretical capacity 6.70 mAh), respectively. The graphs show the accumulated capacity passed through the bulk electrolysis cell where the reduction steps are visible as a falling line and the oxidation steps as a rising line. Alongside this, the signal measured in the OCV cell is plotted on the second abscissa. Both OCV graphs show a similar pattern of the expected sharp spikes as well as the anticipated bias

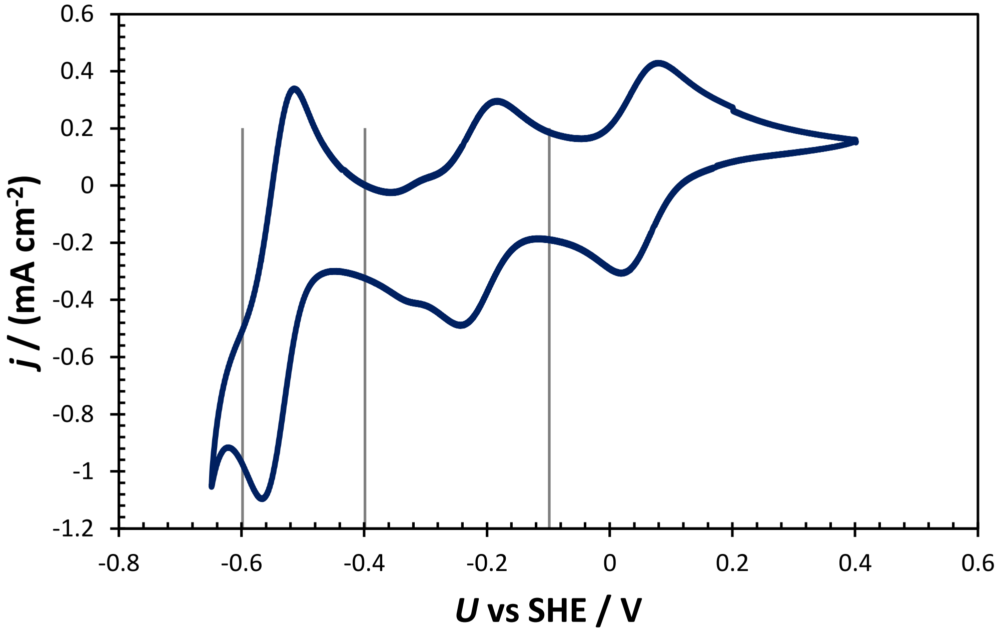

Figure 5.15 CV of SiW_{12} (2.5 mM in 1 M LiCl) at pH 1.95. Indicated are the potential limitations used for the bulk electrolysis procedure: -588 mV vs SHE, -388 mV vs SHE and -88 mV vs SHE. WE: GC-disc, CE: Pt-wire in 1 M Li_2SO_4 pH 1.95, separated from main compartment by a Nafion membrane, RE: Ag/AgCl in 3 M NaCl, scan-speed: 100 mV/s.

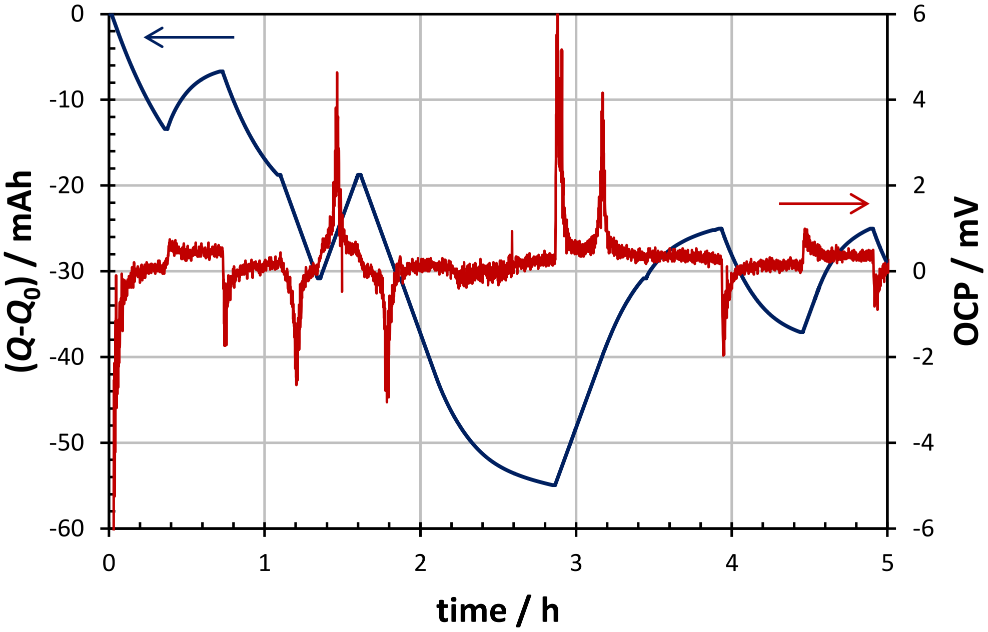

Figure 5.16 Capacity (bulk electrolysis cell, blue trace, left abscissa) and OCV (flow cell, red trace, right abscissa) vs time for the blank measurement (both booster cartridges empty). Electrolyte: 200 mL 2.5 mM SiW_{12} in 1 M LiCl , pH 2.19.

in OCV. Overall the deviation from 0 V OCV is smaller in figure 5.17, indicating better matched flow speeds for both channels during this experiment.

One major difference is exhibited by the capacity graph (blue) during the reduction step from -2 e^-/molecule to -4 e^-/molecule, starting at around 1.8 h experiment time, at ca. -30 mAh for both figures. In figure 5.16 the capacity graph during this step initially displays a constant slope (representing a constant current, i.e. the maximum current of 50 mA). However, upon getting closer to the target of -4 e^-/molecule, the potential limit was met. This potential was then kept (constant potential part of the CCCP operation) with the current decreasing which results in the capacity graph deviating from the previous constant slope and the gradient of the curve becoming less negative. In figure 5.17, the initial constant slope in this section was maintained much longer with only minimal gradient change towards the end of this step.

The fact that in figure 5.17 the current could be kept at the maximum level

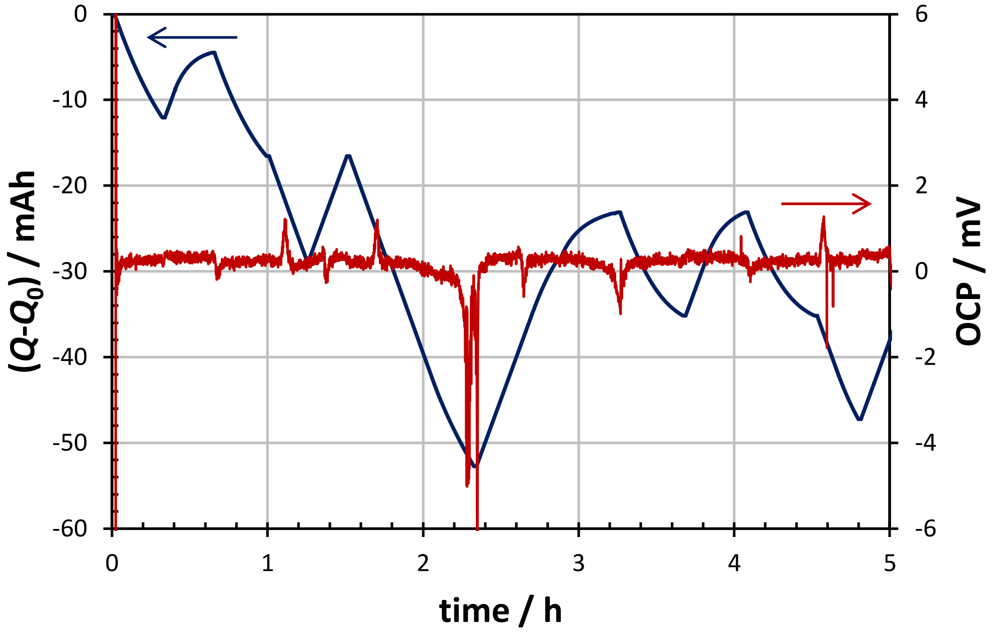

Figure 5.17 Capacity (bulk electrolysis cell, blue trace, left abscissa) and OCV (flow cell, red trace, right abscissa) vs time for the booster measurement (one of the two cartridges equipped with 39.5 mg AQ-tris mixed with 16.9 mg carbon black). Electrolyte: 200 mL 2.5 mM SiW_{12} in 1 M LiCl , pH 1.95.

for longer and that it did not decrease as much after meeting the potential limit shows that *U* of the electrolyte solution was reduced less with the booster present, i.e. some of the reduction equivalents transferred to the SiW_{12} have been passed on to the booster. This observation is supported by the OCV graph showing a rather large and relatively broad spike of negative potential voltage in the booster experiment (figure 5.17) at precisely the same section in the graph (around 2.3 h experiment time). This shows that the *U* in the electrolyte solution that had just passed through the booster at this time was lower than the *U* in the electrolyte in the complimentary half-cell that had not passed through booster material. In other words it became harder to transfer more reduction equivalents to the electrolyte when there was no booster present (from ca. 2.2 h experiment time, figure 5.16) since its *U* had dropped more compared to the measurement with booster (figure 5.17).

However, even though these experiments indicate that the booster was able to absorb some of the reduction equivalents from the electrolyte, the anticipated corresponding discharge of the booster could not be discerned. Expected was a positive signal of the OCV plot in figure 5.17, similar to the negative one at around 2.3 h experiment time.

Even though the WE in the bulk electrolysis cell reached a potential of +0.5 V vs. Ag/AgCl (+0.709 V vs. SHE) at around 2.9 h experiment time, no such peak could be observed. +0.709 V vs. SHE should serve to fully oxidise the SiW_{12} again (compare CV in figure 5.15). Yet, the capacity graph in figure 5.17 did not approach 0 again. Instead, it shows that only about 57% (30 mAh out of the max of 53 mAh) of the capacity transferred to the electrolyte in the bulk electrolysis process could be recovered. Similar experiments were also performed at higher pH values and in KCl instead of LiCl but no clear evidence of the booster discharging could be found in the data either. Also, when comparing the experiments with and without carbon black mixed into the booster materials, no definite advantage to this could be discerned in this setup.

However, after one experiment (in 1 M KCl at pH 4.4) the bulk electrolysis procedure was switched off after the SiW_{12} was fully oxidised with the pump still running. After some time it was observed that the SiW_{12} started turning blue again, the tell-tale sign of the SiW_{12} being reduced, although no current was applied and no chemical reducing agent was added. Apparently the booster had been reduced but seemed to reduce the POM at a very slow rate. A similar observation was made when increasing the pH of a 2.5 mM SiW_{12} 1 M LiCl solution from 2.2 to 4.9 using conc. LiOH solution. Although the SiW_{12} was fully oxidised before, adding LiOH solution while pumping the electrolyte solution through the booster caused the electrolyte to turn blue (i.e. reduce the SiW_{12}). Considering that the AQ-tris reduction is proton coupled (figure 4.9 on page 35), it seems likely that the re-oxidation was facilitated, once the pH was increased.

These results suggested that AQ-tris required higher pH values to be re-oxidised. However, setting the pH higher than ca. pH 5 - 5.5 was not feasible, as the oxidised SiW_{12} becomes unstable at higher pH values. Figure 6.9 in section 6.3.2 (page 106) shows a comparison of CVs of SiW_{12} at different pH-values and a considerable difference between pH 5.7 and 6.0 due to decomposition.

5.6 Proof of concept

For the positive half-cell booster, the original plan was for a polymer to be synthesised from DBF (as the redox active component, shown in figure 4.10 on page 36) and a linker material (similar to the synthesis shown in figure 4.8) by Dr. Alan Wiles. However, the synthesis proved to be challenging and could not be completed. It was then decided to use DBF directly as a booster candidate, as it is not soluble in water. After several experiments using DBF as the booster and vanadium as the shuttle, it was decided to replace the expensive DBF with the much more readily available ferrocene. Thus, more experiments could be performed using larger quantities of booster material.

Ferrocene was deemed a reasonable replacement for DBF, as their key properties for this experiment are rather similar. Just as DBF, ferrocene is insoluble in water and allows redox reactions on the central Fe atom. Naturally, varying functional groups on the cyclopentadienyl rings affects the equilibrium potential of the redox reaction (approximately 250 mV difference between the redox events shown in figure 5.4 and 5.6 in section 5.2), but the functional groups would be different in the envisioned polymer anyway.

After various attempts of measuring booster activity using different forms of booster cartridges proved to be only of limited usefulness, an alternative approach was chosen. Clearly two things were of vital importance, namely to maximise the interface area between the shuttle and the booster and to avoid any coordination or Coulombic attractions that remove the shuttle from the electrolyte solution and bind it to the booster. Also, it was desirable to be able to contact the booster and the electrolyte solution at will with minimal impact otherwise on the system.

With these considerations in mind an improved experimental setup was designed. It was decided to not use pumps, as switching these on and off in order to contact the booster material with the electrolyte also induced minor other changes to the system. These changes may include altered mixing/stirring behaviour and a different rate of air oxygen diffusing into the system. Instead, the booster material was deposited on a porous substrate, which could be lowered into the electrolyte solution without opening the sealed reaction vessel, thus allowing control over whether the booster is contact with the electrolyte or not. The setup is depicted in figure 5.18.

While ferrocene is insoluble in water, it is soluble in ethanol or acetone. Exploiting this property, small amounts of ferrocene were dissolved in ethanol and pieces of heat-treated and pristine carbon felts were soaked in this solution. The ethanol/acetone was evaporated, leaving the fibres of the carbon felt coated in a thin layer of ferrocene, ensuring a large surface area. An example of the prepared electrodes can be seen in figure 5.19.

In previous experiments, electric charge on the involved molecules posed certain challenges. In the case of DBF in combination with vanadium both the oxidised form of the booster and the shuttle material meant to reduce it were positively charged. The resulting Coulombic repulsion may have prevented interactions between those molecules. In the case of tris-Br and SiW_{12}, it could be shown (section 5.4) that the booster material, positively charged in its oxidised form, trapped the negatively charged SiW_{12}.

Ferrocene (and DBF), however, did not seem to trap negatively charged shuttle materials. This could potentially be explained by the fact that unlike in tris-Br, in ferrocene the positive charge is shielded by the electron-rich cyclopentadienyl

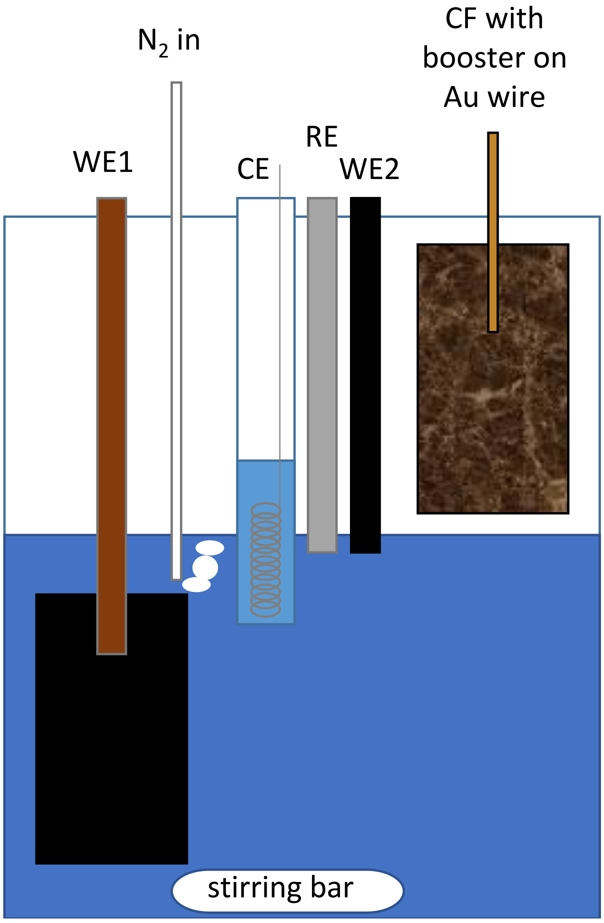

Figure 5.18 Schematic of a setup for measuring booster activity. The primary working electrode (WE1) and counter electrode were used to charge and discharge the electrolyte via bulk electrolysis while stirring and purging the closed system with humidified nitrogen. The booster material was coated onto a piece of carbon felt (Sigracell GFD 4.6 EA carbon felt, 2.5 cm x 5 cm, heat treated at 600 °C for 3 h in air) that could be lowered into the solution and thus measure the influence of the booster on the system capacity. WE1: Sigracell GFD 4.6 EA carbon felt, 2.5 cm x 5 cm, heat treated at 600 °C for 3 h in air, supported by a carbon plastic strip; CE: Pt wire in 1 M NaCl pH 1.5, separated from the main compartment by a Nafion membrane; RE: Ag/AgCl in 3 M NaCl; electrolyte solution: 100 mL, 2.5 mM PMo_{12} 2.5 mM NaI in 1 M NaCl, pH 1.5; WE2: GC-disc for measuring CVs.

Figure 5.19 Photo of a 2.5 cm x 5 cm piece of carbon felt coated in ca. 0.3 g ferrocene. This was achieved by dissolving the ferrocene in ethanol, soaking the carbon felt in this solution and evaporating the solvent.

rings, preventing further coordination from electron donating groups to the electron deficient d-orbitals of the Fe atom.

It was decided that none of the required reactions should depend on the interaction of two like-charged molecules. Since the reduced form of ferrocene does not carry a net charge, this mainly concerned the oxidised form. Hence, a non-positively charged shuttle material for the positive half-cell of the prospective RFB was needed for the reduction of the ferrocene-booster. Initially, PV_{14} was considered, as it had previously been successfully tested in our group as the positive half-cell electrolyte material in an RFB (appendix B and [24]). However, PV_{14} exhibits multiple electron transfer reactions in immediate vicinity to each other in terms of equilibrium potential. Also, all of those electron transfers are proton coupled, so any reduction or oxidation is affected by and affects the pH of the solution.[24] In general, using PV_{14} for this experiment might have led to uncertainties when attributing charge to either the electrolyte or the booster which is why it was not used here.

This led to trials with PMo_{12} as the shuttle material, a negatively charged POM suitable for the use in the positive half-cell of an RFB with individual electron waves much more clearly separated in terms of equilibrium potential (compared to PV_{14}). Comparing the CVs of PMo_{12} and ferrocene (figure 5.20),

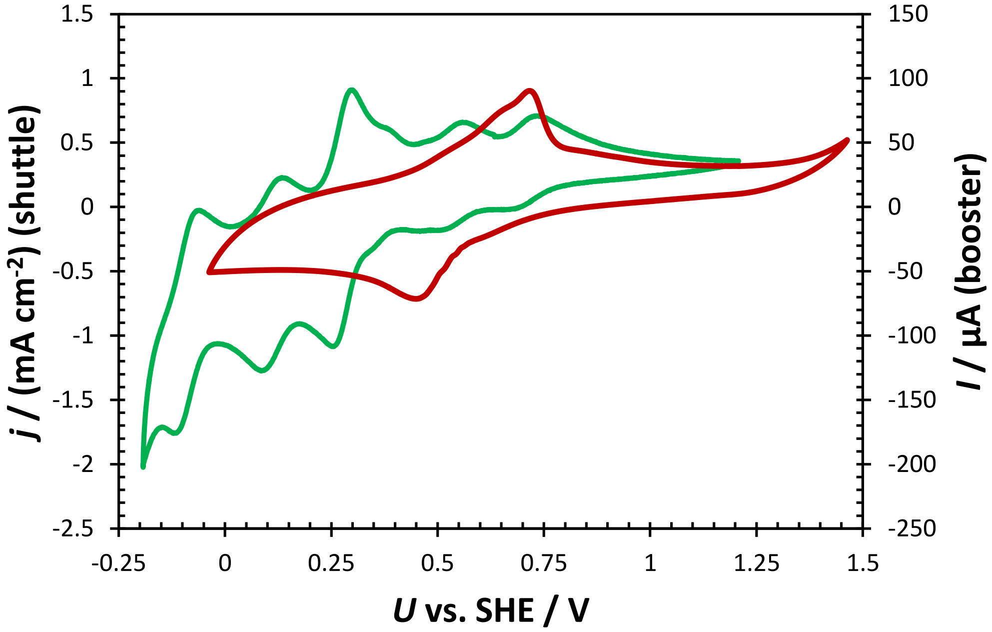

Figure 5.20 Comparison of a a CV of PMo_{12} (2.5 mM in 1 M NaCl pH 1.5, green trace, left abscissa) to a membrane CV of ferrocene (in 3 M NaCl, red trace, right abscissa). WE: GC-disc, CE: Pt-wire, RE: Ag/AgCl in 3 M NaCl, scan-speed: 100 mV/s.

the oxidation peak of the first electron wave of PMo_{12} matches the oxidation peak of ferrocene quite well. This would be ideal in the case of zero overpotential for the redox reaction between booster and shuttle. However, the overpotential was unknown and since the booster material in this case was not conductive, this overpotential could not be directly measured (as discussed in section 4.1.1). For the target of obtaining a proof of concept, efficiency was deemed a secondary objective, so a second shuttle material was added with a redox potential sufficiently higher in an attempt to make sure that possible overpotentials could be overcome.

After screening the literature and testing various candidates, NaI was chosen, as it exhibited a redox wave approximately in the desired potential range (ca. + 800 to 1000 mV vs. SHE). CVs were measured in the supporting electrolyte (1 M NaCl) of PMo_{12} (green trace in figure 5.21) and NaI (red trace) individually and combined (blue trace).

The observed reactions of NaI (red trace) with oxidation peaks at ca. 780 mV and ca. 1080 mV vs. SHE are presumably those of iodide to iodine and/or hypoiodous acid and further to iodate.

Oxidation of iodide to iodine or to hypoiodous acid[77]:

$$2\,\mathrm{I}^- \rightleftharpoons \mathrm{I}_2 + 2\,\mathrm{e}^- \qquad U^o\, vs\, SHE = 0.535\,V$$
$$\mathrm{I}^- + \mathrm{H}_2\mathrm{O} \rightleftharpoons \mathrm{HOI} + 2\,\mathrm{e}^- + \mathrm{H}^+ \qquad U^o\, vs\, SHE = 0.987\,V$$

and further to iodate[77]:

$$\mathrm{I}_2 + 6\,\mathrm{H}_2\mathrm{O} \rightleftharpoons 2\,\mathrm{IO}_3{}^- + 12\,\mathrm{H}^+ + 10\,\mathrm{e}^- \qquad U^o\, vs\, SHE = 1.195\,V$$
$$\mathrm{HOI} + 2\,\mathrm{H}_2\mathrm{O} \rightleftharpoons \mathrm{IO}_3{}^- + 4\,\mathrm{e}^- + 5\,\mathrm{H}^+ \qquad U^o\, vs\, SHE = 1.134\,V$$

Theoretically, all of those reactions can occur in the measured potential window. Furthermore, hypoiodous acid disproportionates and iodine forms tridiodide together with iodide[77]:

$$3\,\mathrm{HOI} \rightleftharpoons 2\,\mathrm{I}^- + \mathrm{IO}_3{}^-$$
$$\mathrm{I}_2 + \mathrm{I}^- \rightleftharpoons \mathrm{I}_3{}^-$$

The further details of those processes go beyond the scope of this work. However, it is clear that both active components of the electrolyte influence each other: This is not surprising, given that PMo_{12} was added in its fully oxidised form and NaI in its fully reduced form. Hence, it is possible that PMo_{12} (partly) oxidised NaI. Also, air oxidation could have played a role, as the solution was only purged with nitrogen before measuring CVs, but not prepared in an oxygen-free atmosphere. Another possible reason for the shifted oxidation peaks of NaI is the fact that the redox reactions of NaI in the respective potential region are proton coupled and PMo_{12} is a buffer taking up the protons released upon oxidation.

This shift seemed to work in favour of the experiment, as the new oxidation peaks occurred precisely in the desired potential range, at ca. 840 mV and 950 mV vs. SHE, the latter being ca. 240 mV positive of the oxidation peak of ferrocene as measured using the membrane-CV method (also measured at 100

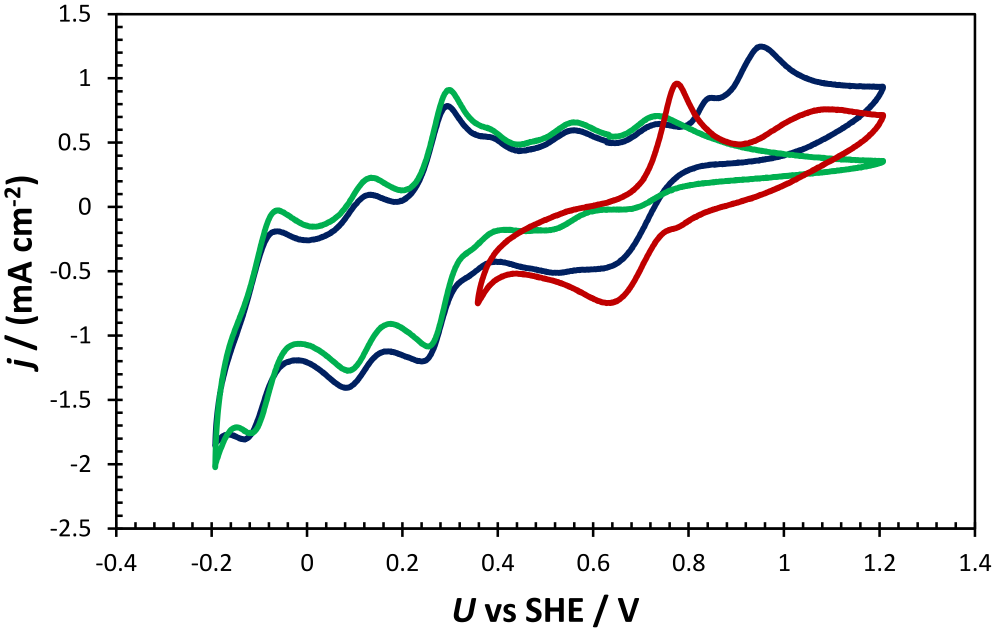

Figure 5.21 CVs of PMo_{12} (2.5 mM in 1 M NaCl pH 1.5, green trace), NaI (2.5 mM in 1 M NaCl pH 1.5, red trace) and PMo_{12}+NaI (2.5 mM each in 1 M NaCl pH 1.5, blue trace). WE: GC-disc, CE: Pt-wire, RE: Ag/AgCl in 3 M NaCl, scan-speed: 100 mV/s. It can be seen that the redox behaviour of NaI is affected by the presence of PMo_{12}.

mV/s in 1 M NaCl).

Initially, it was planned to assemble the whole system with the ferrocene-coated carbon felt suspended from a gold wire above the electrolyte solution, ready to be lowered into it when required, so that the closed, nitrogen purged glass vessel did not need to be opened for contacting the booster and the solution. However, it was discovered that the ferrocene coating sublimed slowly over time when the felt was not submerged in an aqueous solution. Specifically, after less than a week, the orange colour on samples exposed to air (GFD 4.6, heat-treated and pristine, ferrocene loading ca. 0.09 g/cm^2) had completely vanished and only trace amounts of ferrocene could be detected using cyclovoltammetry.

Yet, the booster experiments were planned to be conducted in such a way that the electrolyte alone, without the booster, was cycled over night to equilibrate the system and establish a baseline of the capacity without booster. A

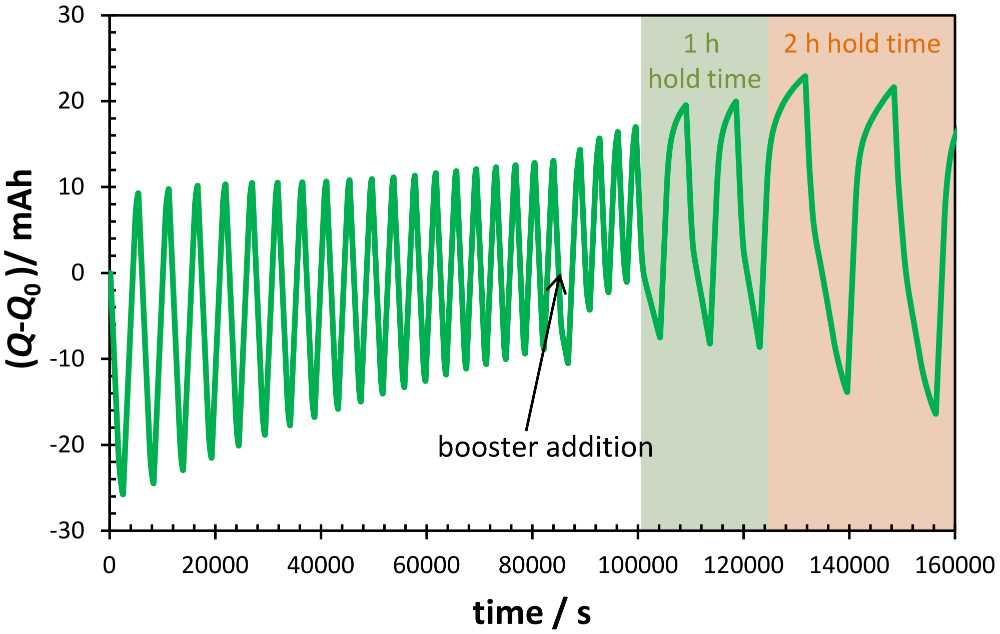

Figure 5.22 Capacity vs time for cycling a half-cell containing 100 mL 2.5 mM PMo_{12} 2.5 mM NaI in 1 M NaCl pH 1.5 (first 28 cycles). A ferrocene (0.311 g) coated carbon felt was lowered into the stirred solution at ca. 85,000 s experiment time and the potential hold time for the charge/discharge procedure altered in subsequent cycles. Charge/discharge methodology: +/- 50 mA constant current until 0.7 V/-0.15 V vs. Ag/AgCl were reached, then constant potential until the current decayed to +/- 10 mA. This minimum current cut-off limit was subsequently replaced by a 1 h and then a 2 h constant potential step.

charge/discharge current of 50 mA (4 mA/cm^2 of geometric area of the carbon felt WE) was chosen as a compromise between increased efficiency and being able to measure a reasonable number of cycles in a given time. In order to avoid leaving the ferrocene-coated carbon felt in the purged nitrogen atmosphere (and thus not submerged in the aqueous solution) for this extended period of time and have an unknown amount of ferrocene sublime, the booster felt was freshly prepared after the equilibration period. Hence, the reaction vessel had to be opened briefly to add the booster felt, which then was immediately lowered into the electrolyte solution. The oxygen ingress caused by this could be seen in an increased reduction capacity for that cycle (at ca. 85,000 s experiment time in figure 5.22).

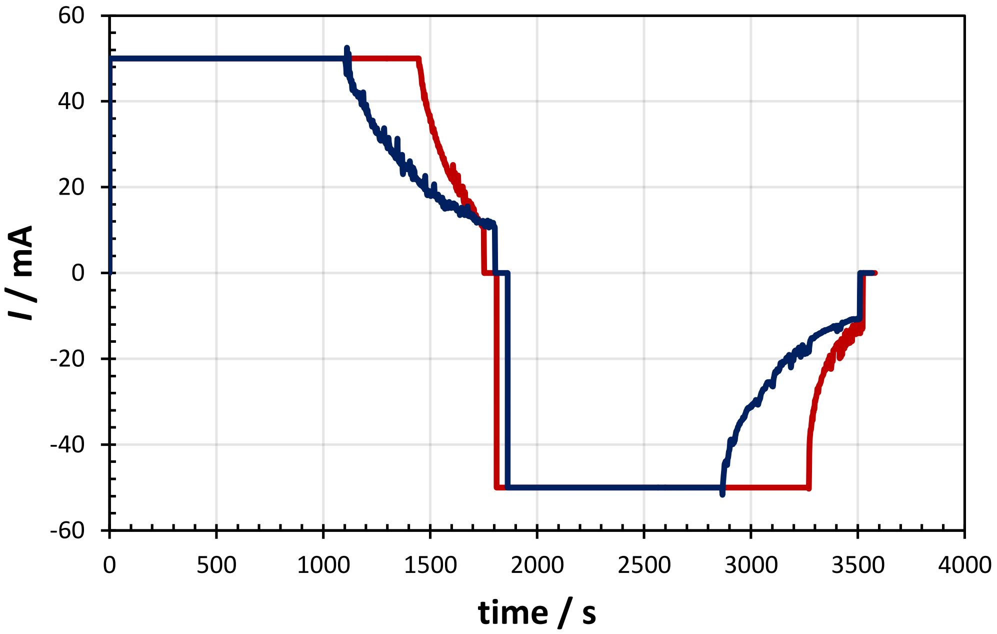

Figure 5.23 Comparison of the cycling behaviour of the PMo_{12}/NaI half-cell shown in figure 5.22 of the cycles just before (cycle 18, red trace) and after (cycle 21, blue trace) the booster was added and the system had stabilised again. It can be seen that during both charge and discharge the current dropped less abruptly during the constant potential steps when the booster was present.

Evaluating the capacity graph (figure 5.22), after the booster was added and the accompanying oxygen ingress was compensated for by the increased reduction capacity during cycle 20, the maximum charge and discharge capacity actually decreased rather than increased, as shown in figure 5.22 and 5.24. Nevertheless, when comparing the cycles immediately before and after addition of the booster, a discrepancy was noted (figure 5.23). In the cycles after addition of the booster the current, rather than dropping steeply towards the end of the charge/discharge-process, still dropped initially but then started to stabilise, so that it took considerably longer to reach the cut-off condition (current drops to 10 mA) compared to the cycles just before adding the booster. This trend was observed for all the cycles just before and just after adding the booster.

This indicated that the booster in fact did take up charge, but at a very slow rate. The cut-off conditions for the charge and discharge cycles were therefore

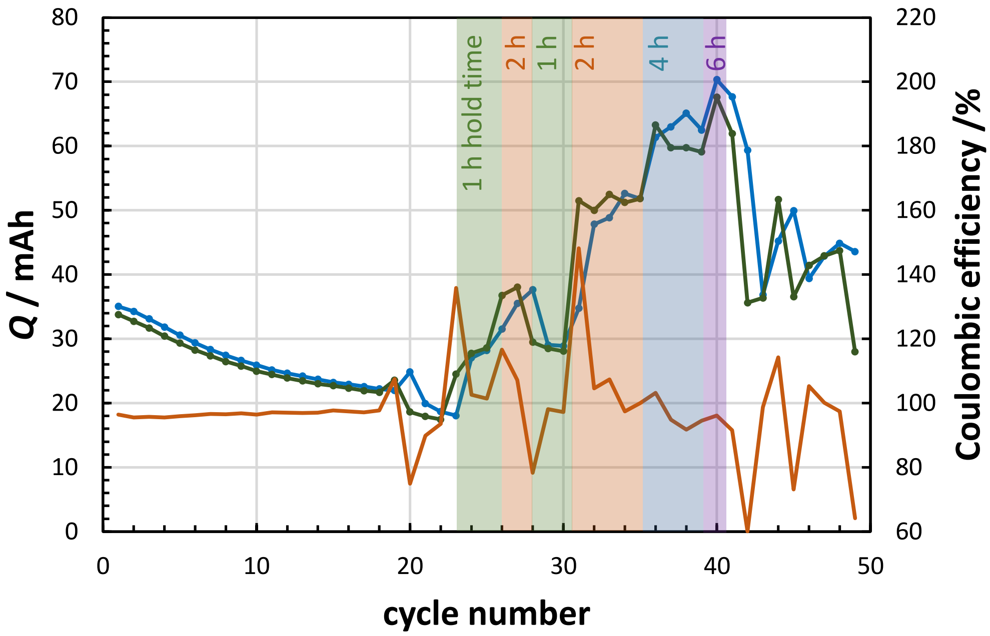

Figure 5.24 Overview of the charge (blue trace) and discharge (green trace) capacity as well as the Coulombic efficiency (orange trace) for each cycle for the PMo_{12}/NaI half-cell shown in figure 5.22. The ferrocene booster was added during cycle 20. Subsequently, potential hold times for the charge/discharge procedure were adapted (marked as coloured background) with the resulting change in charge and discharge capacity visible.

adjusted. Previously, the cycles followed a CCCP-pattern, charging/discharging at 50 mA until +0.7 V/ - 0.15 V vs Ag/AgCl (+0.909 V/ +0.059 V vs SHE) were reached and then holding this potential until the current had dropped to 10 mA. The second, constant potential part was now set to 1 h, without a lower limit for the current. This measure caused the maximum obtainable capacity to increase, as can be seen in figure 5.22. This figure also shows the effect of a two-hour potential holding time, as introduced around 125,000 s experiment time. Furthermore, 4 h and 6 h holding times were tested. The maximum charge- and discharge capacity for each cycle can be seen in figure 5.24.

Just before adding the booster to the system, the capacity of the electrolyte alone had stabilised around 22.3 mAh (averaged discharge capacity over the last five cycles before addition of the booster). For this experiment, 0.311 g ferrocene

Table 5.1 Discharge capacity and relative capacity increase of a PMo_{12}/NaI half-cell with ferrocene booster for different potential hold times. Values of column 3 and 4 based on an electrolyte capacity of 22.3 mAh. Discharge capacity values averaged over cycles 29,30 (1 h), 33-35 (2 h), 37-39 (4 h), 40 (6 h), as shown in figure 5.24.

potential hold time after cut-off potential was met in h	total discharge capacity in mAh	added capacity attributed to booster in mAh	capacity increase by booster in %
1	28.3	6	26.9
2	51.8	29.5	132.3
4	59.5	37.2	166.8
6	67.6	45.3	203.1

had been deposited on a piece of carbon felt (2.5 cm x 5 cm, heat treated at 600 °C for 3 h in air). The amount of booster used corresponded to a theoretical capacity of 44.8 mAh.The total discharge capacity increased to around 28.3 mAh, 51.8 mAh and 59.5 mAh for holding times of 1 h, 2 h and 4 h, respectively (table 5.1). For 6 h holding time, a maximum discharge capacity of 67.6 mAh was observed, an approximately threefold increase compared to the stabilised capacity of the electrolyte alone. Subtracting the observed stabilised capacity of the electrolyte (22.3 mAh) leaves 45.3 mAh; a value which deviates by only 1.1% from the theoretical capacity of the tested booster material (44.8 mAh).

However, it was noted towards the end of this long experiment (ca. 128 h experiment time after finishing the first charge/discharge cycle at 6 h potential hold time) that ferrocene particles detached from the carbon felt. Thus, when the felt was pulled out of the electrolyte in cycle 42, booster particles remained in solution.

To verify that the additional capacity obtained by long potential hold times was in fact due to the booster material and not obtainable by applying the same cycling conditions to the electrolyte alone, the experiment was reset and a control experiment was conducted. Using a freshly made electrolyte solution of the same composition as in the previous experiment (2.5 mM PMo_{12} plus 2.5 mM NaI in 100 mL 1 M NaCl at pH 1.5) the reset system was cycled three times with a potential hold time of 30 min after which the potential hold time was increased

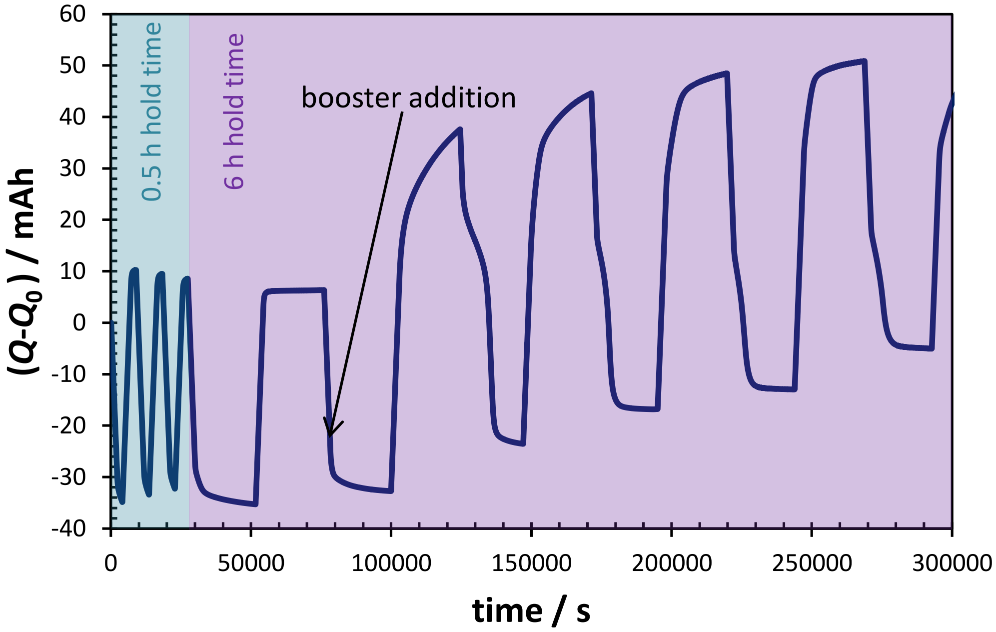

Figure 5.25 Repetition experiment of the one shown in figure 5.22 using the same electrolyte amount and composition, but with the ferrocene-loaded carbon felt present in the nitrogen purged reaction vessel from the start of the experiment, lowered into the solution at ca. 78,000 s experiment time. Charge/discharge methodology: +/- 50 mA constant current until 0.7 V/-0.15 V vs. Ag/AgCl were reached, then constant potential for 0.5 h, which after 3 cycles was increased to 6 h.

to 6 h as in the final step of the previous experiment. Figure 5.25 shows that very little capacity could be gained by only increasing the potential hold time (cycle 4, ca. 30,000 - 80,000 s experiment time). The capacity gain observed in the previous experiment can therefore be attributed to the ferrocene booster. During the reduction step, the current did not quite drop to zero as it did during the oxidation step, which thence can be attributed to the not fully preventable ingress of air oxygen.

This repetition experiment was also used to investigate the effect of exposing the ferrocene-coated carbon felt (ca. 0.357 g ferrocene (theoretical capacity 51.4 mAh) on 2.5 cm x 5 cm GFD 4.6, heat-treated at 600 °C for 3 h) to the nitrogen purged atmosphere of the reaction vessel for extended periods of time, which was deliberately avoided in the previous experiment, as described above.

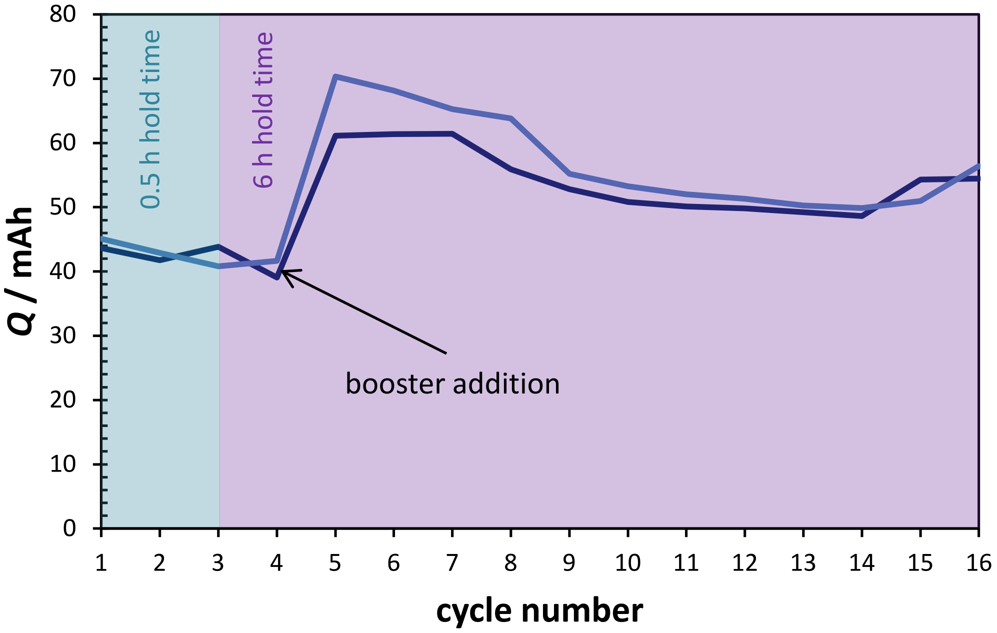

Figure 5.26 Charge (light blue trace) and discharge (dark blue trace) capacity vs. cycle number for the repeat experiment also shown in figure 5.25. The booster was added during the reduction step after the first 6 h reduction/oxidation step had been completed.

In this case, the booster felt was suspended from a gold wire above the electrolyte solution from the start of the experiment, so opening of the reaction vessel to the atmosphere was not required for lowering the booster into the solution. The felt with booster had been suspended above the electrolyte solution during the initial cycles but had no contact with the liquid until it was lowered into the solution after the 6 h potential hold time step was completed (for establishing the electrolyte capacity).

Adding the booster was done at around 78,000 seconds experiment time, during a reduction step after completing the first 6 h reduction/oxidation step of the electrolyte alone. No significant change could be observed in the initial reduction step right after adding the booster (Figure 5.25). This was expected, since the booster was added in its already reduced form.

During the following oxidation step, however, a stark difference was visible: After the initial steep increase in added capacity, the capacity kept increasing at a slower rate throughout the potential hold step. This was in contrast to the previous cycle without booster, when after the initial steep increase in capacity (attributed to the electrolyte) the current suddenly dropped to a negligible amount (appearing as a horizontal section in figure 5.25). This indicated that no more capacity could be added at this potential. The average discharge capacity in this case was increased from ca. 42.1 mAh to ca. 61.3 mAh by adding the booster (figure 5.26). This increase of ca. 19.2 mAh was, as expected, smaller than the theoretical capacity of 51.4 mAh of the booster, due to the previously discussed sublimation of ferrocene. By the time it was lowered into the electrolyte solution, the felt had spent more than 21 h in the purged nitrogen atmosphere of the reaction vessel and visual inspection confirmed that part of the previously orange covering had been removed, so the actual ferrocene loading when lowering the felt into the electrolyte solution was smaller than what had originally been applied to the carbon felt.

These results confirm the results of the previous experiment and can be seen as proof of concept. Changing no other parameters apart from adding the booster to the system showed that the added capacity was indeed due to the booster, demonstrating that the capacity of a redox flow battery can be increased by means of a solid state booster. Under the conditions chosen for the experiment shown in figure 5.22-5.24, the total capacity of that half-cell was approximately tripled, but theoretically even more booster material could be used and thus a greater percentage of the capacity stored in the booster rather than the electrolyte.

Capacity loss during equilibration period

The initial equilibration period in the experiments above was designed to provide a stable capacity baseline before adding the booster to the system. However, the extend of the capacity loss during this period was considered unusual: Figure 5.24 shows a reduction in discharge capacity from 33.8 mAh (cycle 1) to 21.7 mAh (cycle 18). In similar experiments, where PMo_{12} was bulk-electrolysed by itself, hardly any capacity loss could be observed under otherwise similar conditions, so it seemed likely the capacity loss was related to the iodine.

One possible loss mechanism was discovered after the experiments: The Nafion membrane that was employed to separate the CE compartment from the main compartment was found to have turned a dark orange-brown, which had never been observed in experiments containing only PMo_{12} and thus was attributed to iodine. The colour also matched that of aqueous triiodide solutions. This suspected uptake of I in the Nafion membrane might in fact have already started during the stirring/purging step preceding the actual cycling, potentially explaining the different discharge capacities during the respective first cycles of the two experiments shown in figure 5.24 (33.8 mAh) and 5.26 (43.7 mAh), even though the solutions had identical compositions.

In figure 5.24 the discharge capacity during the first 18 cycles seems to approach a value of ca. 20 mAh. It could be speculated that at this point almost no iodine was left in the solution and that the capacity was essentially only that of the first three electron waves of PMo_{12} (0.25 mmol $\widehat{=}$ 6.700 mAh per electron, $3 \cdot 6.7\,\text{mAh} = 20.1\,\text{mAh}$). Using only three electrons of PMo_{12} certainly does not maximise material utilisation. However, the aim here was to obtain a prove of concept and PMo_{12} was chosen mainly for its well spaced out electron waves at ca. 600 mV vs. SHE. (Utilising high reduction degrees in POMs poses some additional challenges: With higher reduction degree, the stable pH window shifts towards higher pH values, so in any battery application the pH-shift has to be balanced with reduction degree, which has further implications on concentrations and counter cations, as briefly discussed in Appendix C.)

The considerations outlined above imply that more research is necessary to fully understand the role that iodine is playing here and/or if it is actually necessary for charging the booster, as discussed in section 5.8 on page 86.

5.7 Summary and conclusion

After testing a number of different boosters in various setups, it was finally possible to demonstrate a capacity increase of the positive half-cell of a RFB by 203% (compared to the electrolyte only).

The experiments presented in section 5.6 show that, while the electrolyte was essentially fully charged after about 30 minutes (figure 5.23), it took 2 h of potential holding time for the system to charge the booster to 66% of its theoretical capacity, 4 h for 83% and 6 h for full booster capacity usage. Apparently the reaction between booster and electrolyte, which is crucial for actually storing the extra charge in the solid state booster, was very slow and the limiting factor in this system. In retrospect, this result suggests that other previous attempts at storing charge in a booster possibly would have been successful if given more time. In other words, the respective batteries were cycled with and without booster but with little or no potential holding time at the end of the charge and discharge operations, so that the system changed from charge to discharge mode (or vice versa), before a noticeable change in capacity occurred.

Nevertheless, the fact that a booster could be demonstrated to be functioning together with a POM in a RFB marks the target proof of concept. As this proof of concept was the main objective of this project, it can be seen as a successful completion. However, these final experiments also highlighted a major challenge for solid-state RFB boosters: Charge transfer between electrolyte and booster happening on such extended timescales does not only complicate laboratory investigations but it severely limits the system's usefulness in any practical application.

By investigating various materials and setups, it was possible to work out key requirements for this type of system: A main factor, as it turned out, was to give the system enough time after the electrolyte was fully charged to pass on that charge to the booster material while maintaining the potential of the electrolyte. Other crucial points included to avoid binding the shuttle to the booster via Coulombic attraction and to account for pH dependencies for both charge and discharge reactions. These findings, together with the membrane CV technique described in section 4.1.1, should facilitate selection of future candidate systems. Additionally, further improvement of the testing setup seems necessary, as discussed in the following section.

5.8 Discussion and future prospect

As discussed in the previous section, the limiting factor for storing charge in the booster material was the slow reaction between booster and shuttle.

One of the next steps should be to improve the preparation of the booster felt. Ferrocene by itself is hydrophobic and the way the felts were prepared (dissolving the ferrocene in acetone or ethanol, soak the heat treated carbon felts in this solution and let it evaporate) likely caused most of the ferrocene to deposit on the outside of the felt (see figure 5.19). It is possible that this in effect formed a protective layer around the felt, blocking the electrolyte from flowing through the porous interior. Of this layer, only the surface would have been in direct contact with the electrolyte solution. This would also mean that this system heavily relied on the shuttle diffusing into the booster material after the surface layer had reacted, explaining the slow charge/discharge process. Furthermore, this entails that the high surface area, for which the carbon felt was originally selected as a substrate, would have been mostly inaccessible.

One relatively simple improvement of the setup would be to lower the ferrocene loading on the carbon felt by either decreasing the ferrocene amount deposited or by increasing the size of the used carbon felt. That way more of the ferrocene would be in direct contact with the electrolyte which should lead to more capacity being accessible after shorter charge/discharge periods. Ideally the method of deposition could be improved in such a way that the ferrocene forms an even coating on the fibres throughout the carbon felt without blocking the electrolyte from flowing through the felt and thereby making use of the carbon felt's porosity.

Furthermore, it should be investigated whether the conductivity of the substrate actually improves the performance. In principle, the ferrocene should also be able to exchange electrons without a conductive substrate. One possible alternative for carbon felt could be silica wool. Alternatively, ferrocene-linked porous organic polymers could be employed, like the ones reported by Sun *et al.*[78]

It could also be tested, if the oxidation of the ferrocene is possible without the added NaI. As discussed in section 5.6 on page 73, PMo_{12} might be able to oxidise the ferrocene without having added NaI to the electrolyte. Provided it performs similarly without NaI, this would simplify the system and might allow to more accurately assess the capacity gain through the booster. This is because the capacity fade during the initial equilibration cycles (as can be seen in figure 5.24) was deemed unusual for PMo_{12} and hence suspected to be related to the NaI.

Yet, in the interest of scalability it might be beneficial to revert to some type of packed-bed reactor in the medium term, like the one briefly described in section 5.4 on page 55 or the one employed by Zanzola *et al.*[33] While this approach entails further questions regarding particle size, if and how conductive additives should be used, clogging of the system etc., it might also allow to employ booster materials that cannot easily be dissolved and deposited on a substrate.

Moreover, it seems worthwhile to further pursue the approach of employing POMs in this system. Combining low cost, high energy density solid state boosters with POMs of high stability and fast electron exchange holds the promise of combining advantages of both areas, if the charge exchange between the two can be accelerated..

Chapter 6

The electrochemical potential of species with more than two oxidation states

Declaration

The following chapter is intended as a paper manuscript. It is the product of intensive collaboration between Jack Oliver Mitchinson and Felix Leon Pfanschilling. The underlying theoretical groundwork as well as the experimental verification were produced collaboratively, with Felix Pfanschilling's work being more strongly focused on producing the mathematical descriptions and solutions and Jack Mitchinson's work on the simulations and multivariate calculations. Experimental setups and measurements were developed and executed together. The resulting chapter appears in both authors' theses. The authors consider the work presented in this chapter to be of equal contribution.

6.1 Introduction

Being able to accurately simulate and predict the behaviour of a RFB is crucial for understanding, planning and implementation of this type of battery. The prediction of basic parameters, such as U, is of fundamental importance but poses a challenge for systems with more than two possible oxidation states. When describing U of a redox-couple in solution as a function of the concentrations of reduced and oxidised species, the Nernst equation is usually employed. However, if the species in question can adopt a third oxidation state, this equation becomes insufficient and using individual Nernst equations for both redox couples fails to describe the transition regime between them adequately. Yet, this problem occurs frequently, e.g. when describing RFBs containing redox-active species with more than two possible oxidation states, such as POMs. For precise modelling of this type of battery and active species with more than two possible oxidation states a concise description of U is strictly necessary.

Here we present an exact mathematical solution that directly relates U to the S_{Ox} in a system with three possible oxidation states. The concentration profiles of all three species are modelled as well. We also show that finding the exact mathematical description for U for greater numbers of possible oxidation states is complex and of limited usefulness due to the challenges associated with solving higher order polynomials. Instead, a solution is presented that yields S_{Ox} as a function of U (rather than vice versa) for any amount of possible oxidation states. For modelling purposes, these results can be calculated to a desired precision and used in the form of a lookup table. Experimental validation is provided for the predicted values of U.

Furthermore, the behaviour of the limiting currents for each involved redox reaction as well as the individual and total exchange current densities (j_0) are predicted. Additionally, the k_0 values for the involved reactions were measured using two independent techniques and from this data j_0 could be derived. Comparing these experimental values with the predictions showed good agreement.

Section 6.3 details the experimental setup for measuring U over a wide range of S_{Ox} of a multi-oxidation state system. This data was also used to calculate kinetic parameters like k_0 and j_0. Impedance spectroscopy was employed, providing an independent experimental technique for verification of these parameters. Section 6.4 compares the measured values to the predicted ones. Reasons for minor deviations are discussed.

6.2 Relating reduction potential to oxidation state

6.2.1 Limitations of the Nernst equation

In the case of a redox reaction accessing only two different redox states, the reduction potential can be described by the Nernst equation:

$$U = U^{o} + \frac{RT}{nF} \ln \frac{a_{Ox}}{a_{Red}} \tag{6.1}$$

where U = (half-cell) reduction potential, U^{o} = standard half-cell reduction potential, R = universal gas constant, T = temperature, n = number of electrons transferred in the reaction, F = Faraday constant, a_{Ox} = activity of the oxidised species and a_{Red} = activity of the reduced species.

At low concentrations, activity coefficients γ tend to unity, thus activity can be approximated as concentrations c_x. ($c_x \cdot \gamma_x = a_x$):

$$U = U^{o} + \frac{RT}{nF} \ln \frac{c_{Ox}}{c_{Red}} \tag{6.2}$$

The Nernst equation, however, covers only the case for two oxidation states. A hypothetical active species M with three accessible oxidation states M^{I+}, M^{II+} and M^{III+} constitutes two associated redox couples. We can formulate one Nernst equation for each of these redox couples. In order to reduce the number of sub- and superscripts and to improve clarity in the following equations, the concentrations of M^{I+}, M^{II+} and M^{III+} will be written as A, B and C, respectively:

$$U = U^{o}_{AB} + \frac{RT}{F} \ln \frac{B}{A} \tag{6.3}$$

$$U = U^{o}_{BC} + \frac{RT}{F} \ln \frac{C}{B} \tag{6.4}$$

where U^{o}_{AB} describes the standard reduction potential of the reaction $M^{I+} \rightleftharpoons M^{II+} + \mathrm{e}^{-}$ (U^{o}_{BC} analogue). These equations describe the reduction potential reasonably well in the vicinity of the standard potentials but fail to describe the transition regime between the two equations, as shown in figure 6.1. The

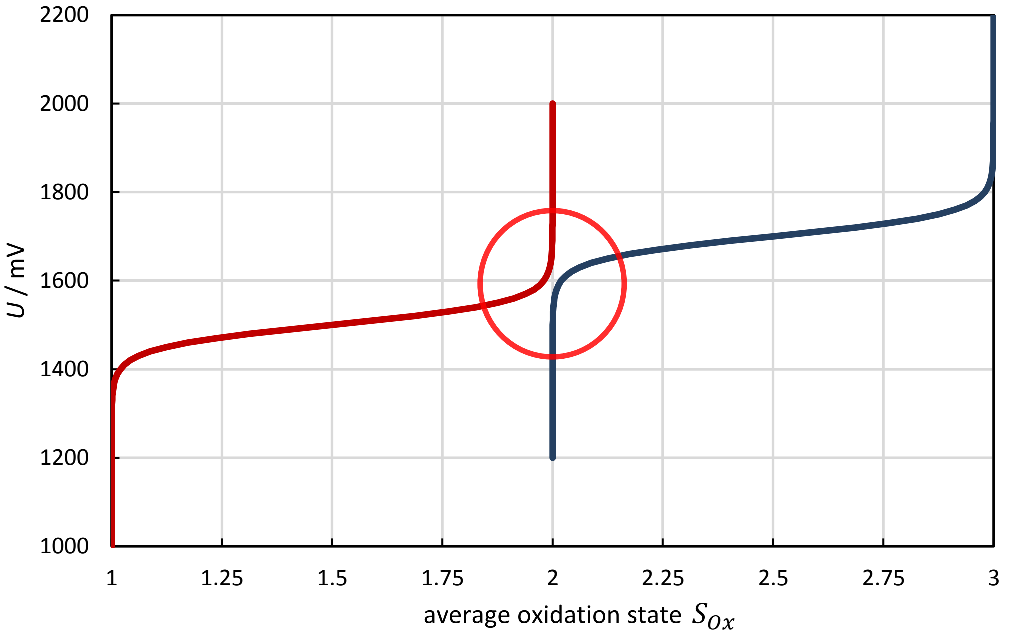

Figure 6.1 Graphical illustration of two individual Nernst equations. The red circle highlights the discrepancy at the transition. $U^o_{AB} = 1500$ mV, $U^o_{BC} = 1700$ mV.

underlying reason is that each equation takes only the concentrations of two species into account, whereas all three species will be present at any given potential in varying fractions.

This formulates the challenge to find a mathematical description of the reduction potential as a function of the average oxidation state in a redox system with multiple redox states that includes the transition regime.

6.2.2 Calculating the reduction potential for a species with 3 oxidation states

The average oxidation state S_{Ox} in our hypothetical system can be described by multiplying each concentration A, B and C with their associated oxidation state 1, 2 and 3, respectively, and dividing the sum of the above by the total concentration of $M(= A + B + C)$:

$$S_{Ox} = \frac{A \cdot 1 + B \cdot 2 + C \cdot 3}{A + B + C} \tag{6.5}$$

In general, this variable can easily be determined from experimentation. For instance by coulomb counting for known concentrations of M, or by comparing spectroscopic data to known references, e.g. UV-Vis spectra of the various oxidation states. A homogeneous solution must have a single reduction potential; therefore, equations 6.3 and 6.4 can be set equal. The constants are separated from the concentrations and for simplicity will be defined as k_1:

$$\exp\left(\frac{F}{RT}(U^o_{AB} - U^o_{BC})\right) = \frac{AC}{B^2} \tag{6.6}$$

$$k_1 = \frac{AC}{B^2} \tag{6.7}$$

Rearranging equation 6.5 for A gives:

$$A = \frac{2B + 3C - S_{Ox}B - S_{Ox}C}{S_{Ox} - 1} \tag{6.8}$$

and substituting equation 6.8 into equation 6.7 gives:

$$k_1 = \frac{C}{B^2}\frac{2B + 3C - S_{Ox}B - S_{Ox}C}{S_{Ox} - 1} \tag{6.9}$$

The result is a second-order polynomial. Solving this for the ratio $\frac{C}{B}$ yields:

$$\frac{C}{B} = \frac{2 - S_{Ox}}{2(3 - S_{Ox})} \pm \sqrt{\left(\frac{2 - S_{Ox}}{2(3 - S_{Ox}}\right)^2 + k_1\frac{S_{Ox} - 1}{3 - S_{Ox}}} \tag{6.10}$$

The negative solution is disregarded as a ratio of two concentrations cannot be negative. Inserting the positive solution into equation 6.4 yields the desired expression that describes the reduction potential as a function of the average oxidation state, implicitly taking into account the interdependence of the various ratios via the reduction potentials included in k_1:

$$U = U^o_{BC} + \frac{RT}{F}ln\left(-\frac{2 - S_{Ox}}{2(3 - S_{Ox})}\right) + \sqrt{\left(\frac{2 - S_{Ox}}{2(3 - S_{Ox})}\right)^2 + k_1\frac{S_{Ox} - 1}{3 - S_{Ox}}} \tag{6.11}$$

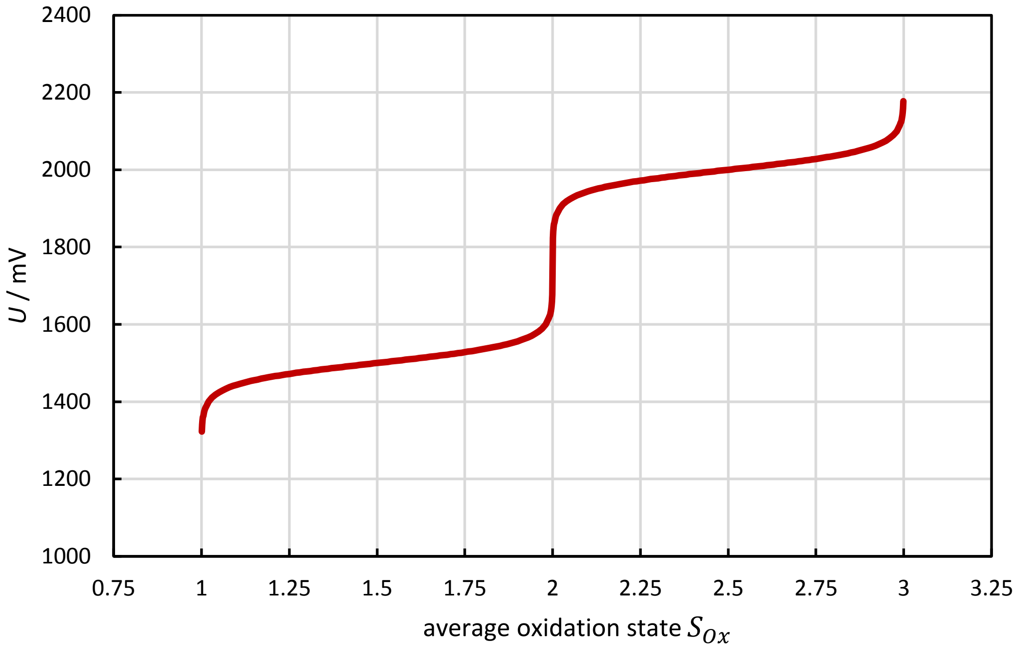

Figure 6.2 Plot of equation 6.11 using 1.5 V and 2.0 V as standard reduction potentials U^o_{AB} and U^o_{BC}, respectively.

The graph shown in figure 6.2 reflects experimental results reasonably well.

6.2.3 Calculating the reduction potential for a species with >3 oxidation states

In theory, this method can be applied to any number of oxidation states. However, with each additional oxidation state, the order of the polynomial will be incremented. When including a fourth oxidation state M^{IV+}, a third Nernst equation can be formulated:

$$U = U^o_{CD} + \frac{RT}{F} ln \frac{D}{C} \tag{6.12}$$

where $D = [M^{IV+}]$. Setting it equal to equation 6.4 and separating constants from concentrations, k_2 can be defined analogously to k_1:

$$\exp\left(\frac{F}{RT}(U^o_{BC} - U^o_{CD})\right) = \frac{BD}{C^2} \tag{6.13}$$

$$k_2 = \frac{BD}{C^2} \tag{6.14}$$

The average oxidation state in this system is also defined analogously:

$$S_{Ox} = \frac{A + 2B + 3C + 4D}{A + B + C + D} \tag{6.15}$$

Combining equations 6.7, 6.14 and 6.15 yields:

$$Q_1^3 k_1^2 k_2 (S_{Ox} - 4) + Q_1^2 k_1 (S_{Ox} - 3) + Q_1 (S_{Ox} - 2) + (S_{Ox} - 1) = 0 \tag{6.16}$$

where $Q_1 = \frac{B}{A}$. Repeating the above procedure for five oxidation states yields:

$$Q_1^4 k_1^3 k_2^2 k_3 (S_{Ox} - 5) + Q_1^3 k_1^3 k_2^2 k_3 (S_{Ox} - 4) + Q_1^2 k_1 (S_{Ox} - 3) + Q_1 (S_{Ox} - 2) + (S_{Ox} - 1)) = 0 \tag{6.17}$$

Comparing equations 6.16 and 6.17, a pattern can be discerned. However, solving higher order polynomials can be complex and computationally expensive. Particularly for general polynomial equations of fifth degree or higher, the Abel-Ruffini theorem states that there is no algebraic solution. To mitigate this, a different approach was chosen: the ratio B/A was calculated for the potential range of interest with increments of 1 mV for U, using a rearranged form of equation 6.3:

$$\frac{B}{A} = Q_1 = \exp\left(\frac{F}{RT}(U - U^o_{AB})\right) \tag{6.18}$$

The results were then used to calculate the associated oxidation states using equation 6.16 in a rearranged form:

$$S_{Ox} = \frac{4Q_1^3 k_1^2 k_2 + 3Q_1^2 k_1 + 2Q_1 + 1}{Q_1^3 k_1^2 k_2 + Q_1^2 k_1 + Q_1 + 1} \tag{6.19}$$

The result can be regarded as a lookup table for correlating S_{Ox} and U.

Figure 6.3 shows the result plotted as U vs. S_{Ox}. This approach can be used for any number of potential oxidation states and with smaller increments for U, if increased precision is desired.

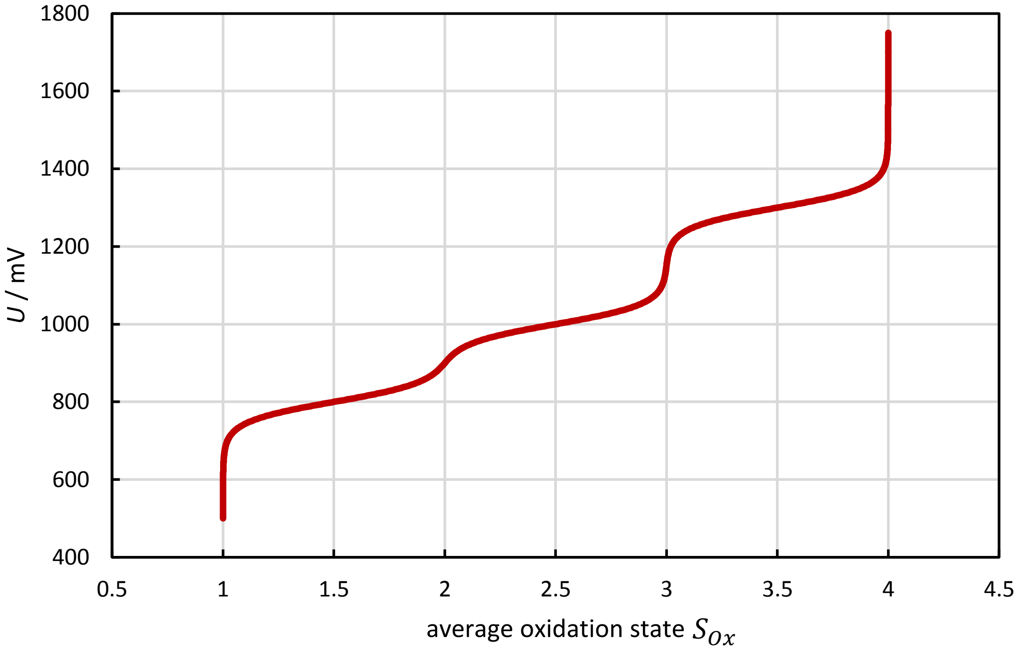

Figure 6.3 Plot of equation 6.19 using the results from equation 6.18 in the potential range from 0.5 V to 1.75 V with 1 mV increments. 0.8 V, 1.0 V and 1.3 V are used as standard reduction potentials U^o_{AB}, U^o_{BC} and U^o_{CD}, respectively.

6.2.4 SiW_{12} as an example case

As an illustrative example, we consider the first three reactions of SiW_{12}:

$$\begin{aligned}
&\mathrm{SiW}_{12}(0) + \mathrm{e}^- \rightleftharpoons \mathrm{SiW}_{12}(-1) && U^o_{CD}\ vs\ SHE = 0.00\,V \\
&\mathrm{SiW}_{12}(-1) + \mathrm{e}^- \rightleftharpoons \mathrm{SiW}_{12}(-2) && U^o_{BC}\ vs\ SHE = -0.26\,V \\
&\mathrm{SiW}_{12}(-2) + 2\,\mathrm{e}^- \rightleftharpoons \mathrm{SiW}_{12}(-4) && U^o_{AB}\ vs\ SHE = -0.40\,V
\end{aligned}$$

Since electrons are at least partially delocalised in POMs[24, 79], oxidation states cannot be assigned to individual atoms. We therefore give the oxidation state of the whole molecule in parenthesis as the deviation from the fully oxidised

POM. U can be described by the rearranged Nernst equations 6.20-6.22:

$$\exp\frac{(U-U^o_{AB})2F}{RT}=\frac{B}{A}=Q_1 \tag{6.20}$$

$$\exp\frac{(U-U^o_{BC})F}{RT}=\frac{C}{B}=Q_2 \tag{6.21}$$

$$\exp\frac{(U-U^o_{CD})F}{RT}=\frac{D}{C}=Q_3 \tag{6.22}$$

As before, the concentration of the lowest oxidation state is assigned A, the second lowest oxidation state B, etc. with the standard reduction potential for the transition between two states marked with the respective subscript, i.e. U^o_{AB} for the transition from A to B. Hence, $[\mathrm{SiW_{12}}(-4)] = A$, $[\mathrm{SiW_{12}}(-2)] = B$, $[\mathrm{SiW_{12}}(-1)] = C$ and $[\mathrm{SiW_{12}}(0)] = D$. Therefore, for any given potential, the reaction quotients Q_i are known. Additionally, the total concentration of species is given by:

$$A+B+C+D=M \tag{6.23}$$

Substitution of the quotients defined by equations (6.20) - (6.22) into equation (6.23) yields expressions for the concentration of individual species:

$$A=\frac{M}{Q_1Q_2Q_3+Q_1Q_2+Q_1+1} \tag{6.24}$$

$$B=\frac{Q_1M}{Q_1Q_2Q_3+Q_1Q_2+Q_1+1} \tag{6.25}$$

$$C=\frac{Q_1Q_2M}{Q_1Q_2Q_3+Q_1Q_2+Q_1+1} \tag{6.26}$$

$$D=\frac{Q_1Q_2Q_3M}{Q_1Q_2Q_3+Q_1Q_2+Q_1+1} \tag{6.27}$$

Analagously to equation 6.5, the S_{Ox} for any distribution of species is given by

$$S_{Ox}=\frac{-4A-2B-1C-0D}{A+B+C+D}=\frac{-4-2Q_1-Q_1Q_2}{Q_1Q_2Q_3+Q_1Q_2+Q_1+1} \tag{6.28}$$

Since the reaction quotients Q_i only depend on constants and U, we can express S_{Ox} for any given U. However, when simulating oxidation and reduction processes in a flow battery, the load profile or current regime is typically used as an input parameter. Since in such a case no direct information about U is given, it must be calculated from the change in S_{Ox}. ΔS_{Ox} is easily calculable from the amount of charge ($\mathbf{Q}$) for a given power (P) or current (I). However, as previously discussed, no explicit expression which relates U as a function of S_{Ox} has been found for systems which are governed by more than two Nernst equations (i.e. more than 3 possible oxidation states).

Despite the lack of an explicit relationship, we can define U based on an implicit relationship with reasonably high accuracy. The procedure for relating S_{Ox} to U is as follows:

1. The range of sensible values for U is defined according to the potential profile of the electrolyte.

   For our illustrative system it is unlikely that U will fall outside the range $-0.6 \leq U \leq 0.2V vs\ SHE$.

2. An array of values ranging from $U(min) - U(max)$ is generated.

3. The arrayed values are used to calculate Q_1, Q_2 and Q_3 according to equations 6.20, 6.21 and 6.22, respectively.

4. A, B, C and D are then calculated from the values for Q_1, Q_2 and Q_3 according to equations 6.24, 6.25, 6.26 and 6.27.

5. S_{Ox} can then be calculated from equation 6.28, essentially creating a lookup table for the distribution of species and S_{Ox} over the defined potential range.

6. For a sufficiently dense array, the assumption can be made that for any small change in U the corresponding change in S_{Ox} can be approximated as a linear change. Therefore, linear interpolation of the neighbouring points allows U for any value of S_{Ox} to be determined.

Fig. 6.4 depicts the resulting concentration distribution of A, B, C and D as well as S_{Ox} against U for a total concentration of 80 mM.9

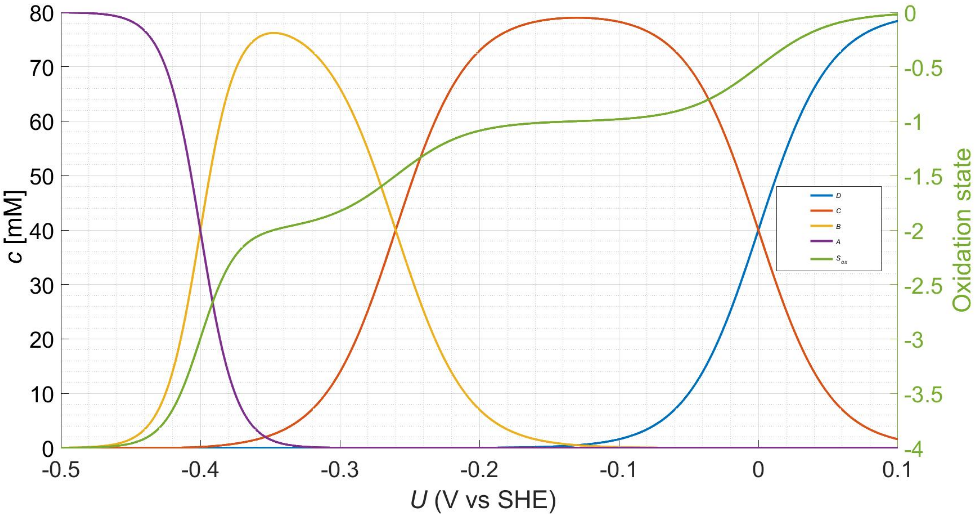

Figure 6.4 Portrayal of the concentration distribution and S_{Ox} vs U for the species described by equations 6.20 - 6.22 where the total concentration is 80 mM.

6.2.5 pH dependence of the reduction potential

The situation becomes somewhat more complex when U is pH-dependent. In that case the concentration of the hydronium cation ($\mathrm{H_3O^+}$) must be considered. For the general case of a proton-coupled electron transfer: $\mathrm{B + n_1\,e^- + z_1\,H_3O^+ \longrightarrow A + z_1\,H_2O}$, where z is the stoichiometric coefficient, U is given by:

$$U = U^o_{AB} + \frac{RT}{n_1 F} \ln \frac{B[\mathrm{H_3O^+}]^{z_1}}{A} \tag{6.29}$$

For the active species containing the redox states A, B and C, where
$\mathrm{B + n_1\,e^- + z_1\,H_3O^+ \rightleftharpoons A + z_1\,H_2O}$ and
$\mathrm{C + n_2\,e^- + z_2\,H_3O^+ \rightleftharpoons B + z_2\,H_2O}$,
following the same procedure as in section 6.2.4 yields

$$\exp \frac{(U - U^o_{AB})n_1 F}{RT} = \frac{B[\mathrm{H_3O^+}]^{z_1}}{A} = Q_1 \tag{6.30}$$

$$\exp \frac{(U - U^o_{BC})n_2 F}{RT} = \frac{C[\mathrm{H_3O^+}]^{z_2}}{B} = Q_2 \tag{6.31}$$

In order to determine the ratio of species, $\frac{B}{A}$ or $\frac{C}{B}$, the pH needs to be taken into consideration. Hence, a relationship between S_{Ox} and pH is required. The precise relationship depends on the electrolyte in question and will be a function of the acid dissociation constants and concentration distribution of the species present in solution. However, if the electrolyte has multiple associated redox couples, then multiple polyprotic species would have to be considered to arrive at a reasonably accurate relationship. Information regarding acid dissociation constants for reduced POMs could not be found. Additionally, the situation is complicated further by the presence of supporting electrolytes, which are, in some cases, also polyprotic. It might, therefore, sometimes be necessary to resort to the use of empirical relationships which will be defined later for the respective systems.

With that established, it is possible to calculate the S_{Ox} for any given pH and U combination. A reasonable range for U and pH is defined and the S_{Ox} is calculated according to a procedure analogous to the one on page 99. The data can be represented as a Pourbaix diagram or surface plot, which can be used in a similar way as the lookup table described in section 6.2.2. If the relationship between pH and S_{Ox} is established (pH$=f(S_{Ox})$), the U for any S_{Ox}/pH combination can simply be inferred from representations like figure 6.5 and 6.6.

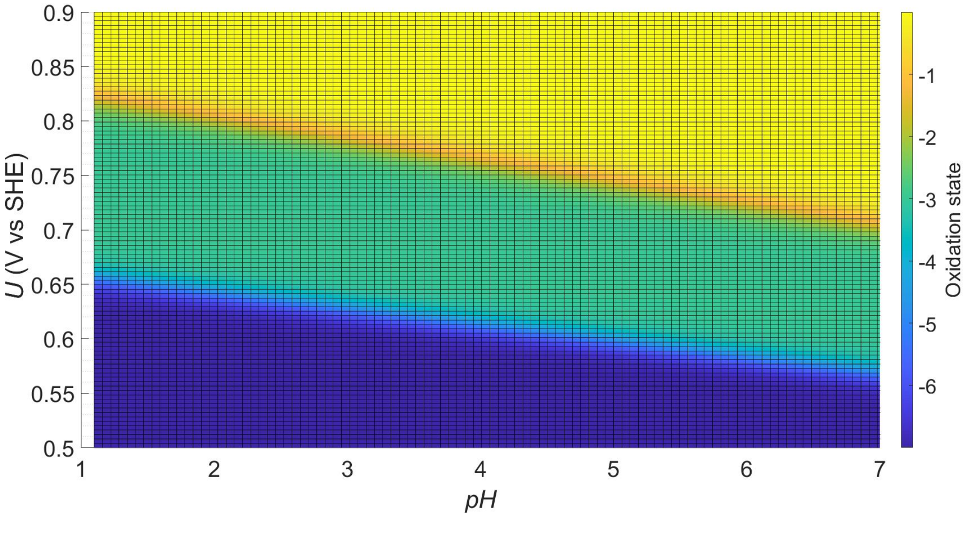

Figure 6.5 Pourbaix diagram for an arbitrary example electrolyte with oxidation states A, B and C, standard reduction potentials $U^o_{AB} = 0.68V$ and $U^o_{BC} = 0.85V$, $n_1 = 4, n_2 = 3$, and $z_1 = z_2 = 1$.

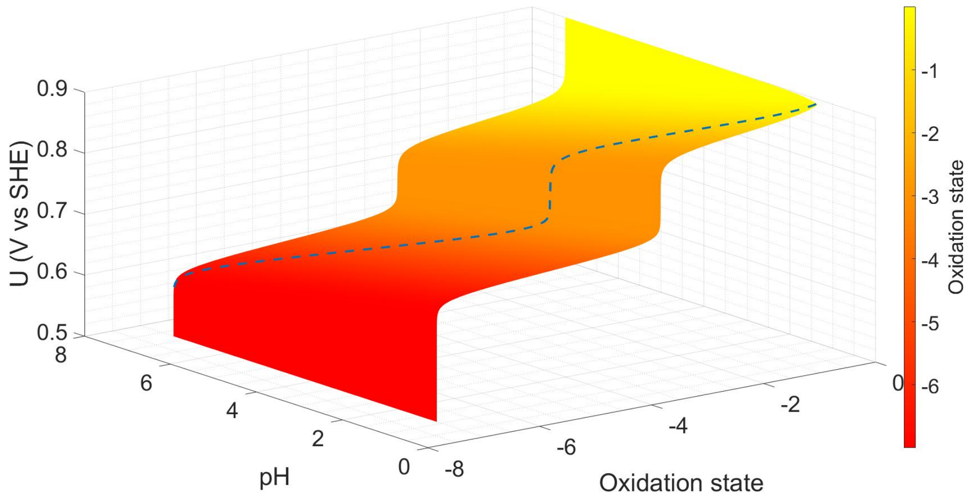

Figure 6.6 A surface plot with the same input parameters as in figure 6.5 depicting the potential profile (blue dotted line) which an electrolyte adopts for the arbitrary relation: pH$= -0.89S_{Ox} + 1.1$

6.3 Experimental

6.3.1 Stationary working electrode experiments

One of the simplest multi-redox couple species available to us, SiW_{12}, was investigated. The two most positive redox reactions are elementary one-electron reactions with no proton coupling and U^os 260 mV apart. [24]

The setup included a redox-flow cell (C-Tech INNOVATION C-Flow LAB 5x5, equipped with 5x5cm 4.6 GFD Sigracell carbon felt electrodes, heat treated for 3 h at 600 °C in air) with the solution of interest (SiW_{12}, aq., 5.33 mM, 100 mL, at an initial pH of 4.0) in one half-cell and a NaCl solution (aq., 1 M, 1 L) in the other half-cell functioning as the counter electrode solution. The counter electrode half-cell also contained a silver wire coated in a layer of silver chloride, which acted as a reference electrode. The separator was a Nafion-117 membrane which, due to being a cation exchange membrane with a small pore size, does not permit significant crossover of POMs.[24]

As a consequence of bulk electrolysis, small amounts of chlorine are evolved

Table 6.1 Electrode specifications for the electrolysis cell (EC) and the reservoir (Res)

electrode	specification
EC working	GFD carbon felt (25 cm^2)
EC counter	GFD carbon felt (25 cm^2)
EC reference	Ag/AgCl in 1 M NaCl (0.200 V vs SHE)
Res working	Polished glassy carbon disk (7.07 mm^2)
Res counter	Au wire
Res reference	Ag/AgCl in 3 M NaCl (0.210 V vs SHE)

and Na^+ crosses the separator. Over time, the change in sodium chloride concentration leads to reference electrode drift. Consequently, all experiments which utilised this setup had their counter electrode solution replaced on a daily basis.

Both half-cells were connected to separate reservoirs which were constantly purged with nitrogen gas (humidified to counter water evaporation). The reservoir containing the POM solution doubled as a three-electrode electrochemical cell. During electrochemical measurements, the pump was stopped and the reservoir solution was stagnant. Figure 6.7 shows a schematic of the setup and table 6.1 details the electrode specifications.

Between electrochemical measurements, the flow was resumed so that the POM solution could be bulk-electrolysed in the flow cell to various extents. After each bulk electrolysis step, the solution was continuously pumped for several minutes so that the oxidation state throughout the RFB and reservoir was homogenised. The homogeneity was easily confirmed by comparing the open circuit potential of the two working electrodes.

The procedure for measuring the U involved polarising the electrode to a fixed potential until a steady state current was attained. This procedure is repeated for numerous applied potentials ± 10 mV vs OCP as shown in figure 6.8. For small overpotentials the electrochemical reaction is kinetically controlled and the current-overpotential relation is linear. The reduction potential can be extracted by interpolating the linear trendline to $I = 0$.

Potentiostatic electrochemical impedance spectroscopy was also carried out on solutions of SiW_{12} at varied oxidation state. This was done using the setup

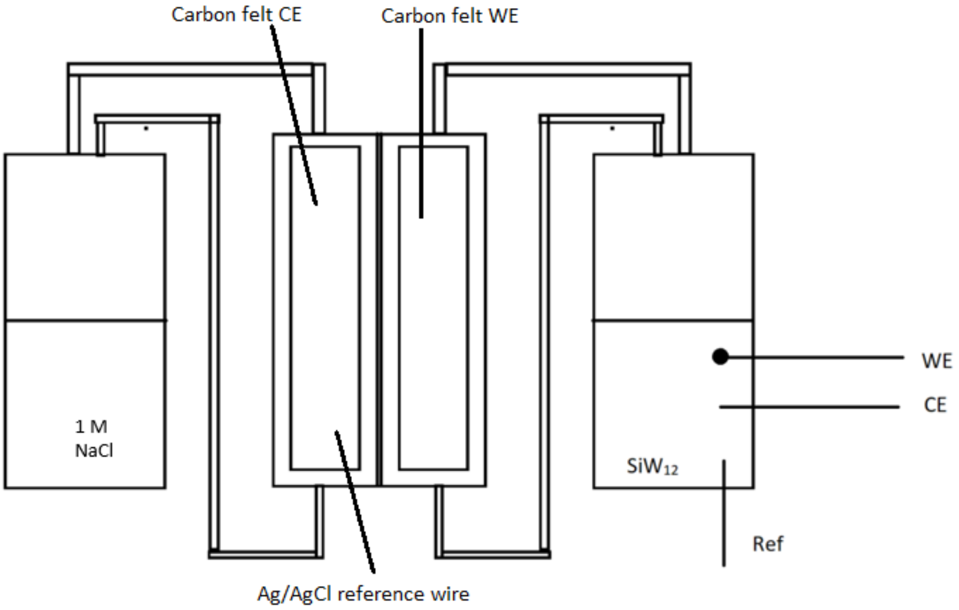

Figure 6.7 Schematic of the setup used for measuring reduction potential and kinetic properties at various oxidation states. The reference electrode for the bulk electrolysis cell is located inside of the cell and is not shown for clarity. There are two potentiostats connected in this experimental setup, one to WE, CE and RE in the electrolysis cell and one to the WE, CE and RE in the reservoir containing the SiW_{12} solution.

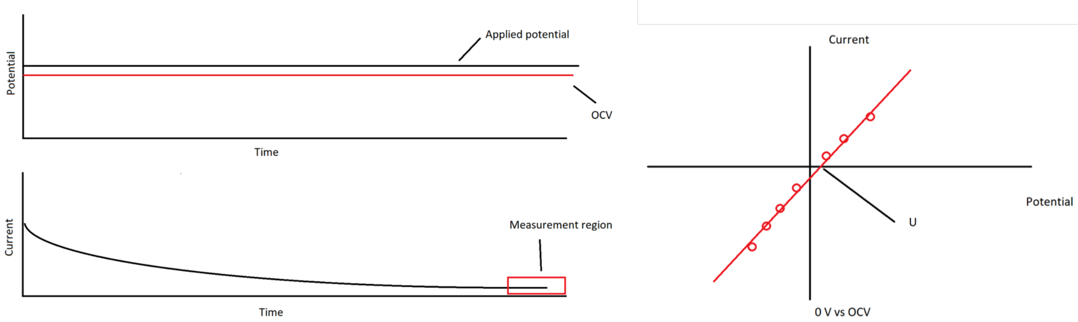

Figure 6.8 Graphical depiction of the experiment procedure (left). Typical plot of the steady state current vs potential (right)

described in table 6.1. The frequency range was 20 kHz-100 mHz and the excitation frequency was 10 mV with no underlying current. Prior to AC excitation, the potential was held at 0 V vs OCP for five minutes.

6.3.2 Rotating disk electrode experiments

As will be discussed in section 6.4.1, mass-transport limitations restrict the usefulness of the data collected in the stationary experiments. Therefore, the reservoir working electrode was replaced with a rotating glassy carbon disk (0.785 cm^2). The concentration of SiW_{12} was also increased to 20 mM to be in-line with previous measurements of kinetic parameters in our group.[24] The starting pH was 2.1, meaning that the third reduction of SiW_{12} (which at a pH < 2 is a two-electron process), is split into two one-electron processes, as shown in figure 6.9. The RDE was spinning at 5000 rpm throughout the experiment. Otherwise, the experimental parameters are identical to those listed in table 6.1.

800 current vs potential (Tafel) plots with maximum overpotentials of ± 250 mV were recorded over the potential range -1.1 V to + 0.1 V vs SHE. This was achieved in the following way:

- As with the stationary electrode experiments described in the previous section, the solution was bulk electrolysed to the desired equilibrium potential by applying a potential at the flow cell working electrode until the current decreased to almost zero.

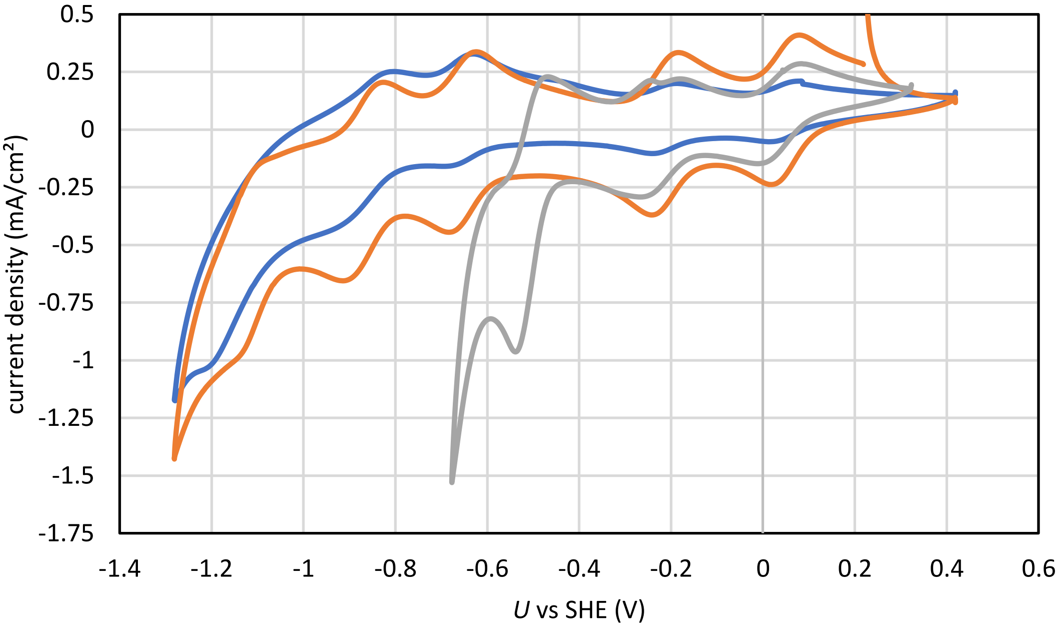

Figure 6.9 Cyclic voltammograms of 5 mM SiW_{12} in 1 M NaCl at varied pH. WE: glassy carbon disk, CE: Pt wire, RE: Ag/AgCl in 1 M NaCl (U = 220 mV vs SHE) for pH > 2 and MSE in 1 M H_2SO_4 (U = 624 mV vs SHE) for pH < 2. pH 1.7 (grey), pH 5.7 (orange), pH 6.0 (blue).

- The open circuit potential was recorded for several minutes to ensure complete mixing.
- With the solution now at a certain equilibrium potential, a slightly deviating potential was applied at the RDE and the resulting current was recorded after it had stabilised, as depicted on the left side in the schematic in figure 6.8. The use of a RDE drastically shortened the required time for the current to stabilise from minutes to under a second.
- The previous step was repeated several times applying a different potential deviation at the RDE until a range of $\pm 250\,\mathrm{mV}$ around the equilibrium potential was covered. The resulting data is depicted schematically on the right hand side in figure 6.8 and examples are shown in figure 6.21.
- The solution was bulk electrolysed again to the next desired equilibrium potential and the whole procedure was repeated.

The range thus covered for the equilibrium potential was -1.1 V to +0.1 V vs. SHE with 800 individual Tafel plots recorded. This was automated using two potentiostats: One for the bulk electrolysis process and one to control the three-electrode setup. Throughout the multi-day experiment, the solutions were constantly purged with humidified nitrogen gas at a rate of ca. $0.5\,\mathrm{L\,min^{-1}}$.

6.4 Results and discussion

6.4.1 Stationary working electrode experiment discussion

The initial set of experiments saw a solution of SiW_{12} (5.33 mM) in 1 M NaCl reduced from the fully oxidised state $SiW_{12}(0)$ to various degrees up to $SiW_{12}(-1.25)$. Thus, at all times the species distribution is dominated by three distinct oxidation states (0, -1 and -2). We therefore model this system using the equations described in section 6.2.2. The extent to which the species is reduced can be determined simply from coulomb counting and the reduction potentials for each unique oxidation state are determined by the method described in section 6.3.1. Figure 6.10 depicts a typical dataset for the stationary cell experiment setup. Figure 6.11 depicts the experimental results and predicted values for the reduction potentials, showing good agreement between the two.

Furthermore, the difference between OCP and the reduction potential was measured for each dataset (figure 6.12) and the difference was found to be small (< 2 mV) for approximately 87% of data sets. Discrepancies between OCP and the reduction potential typically arise due to competing redox reactions on

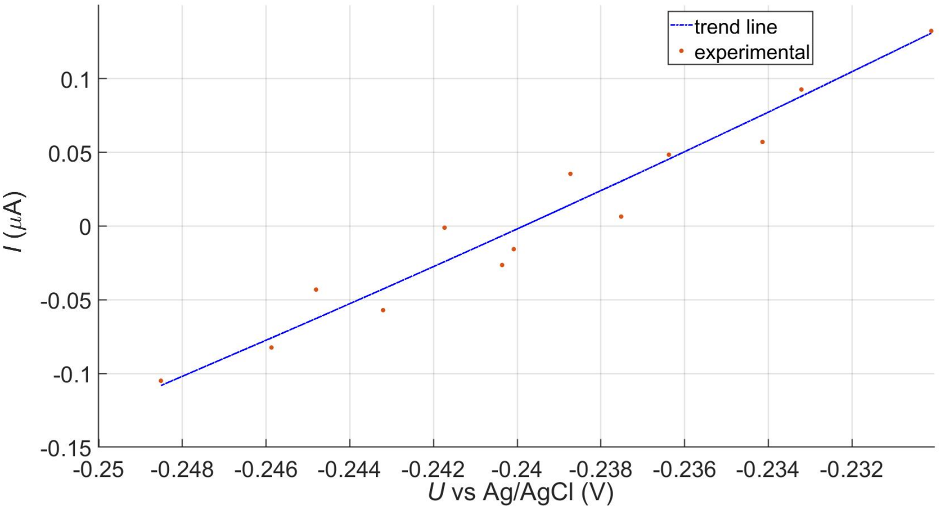

Figure 6.10 Typical results for the experimental procedure described in 6.3.1. steady state current vs potential of a partly reduced SiW_{12}-solution in 1 M NaCl. The trend line (blue) is determined by the least squares method.

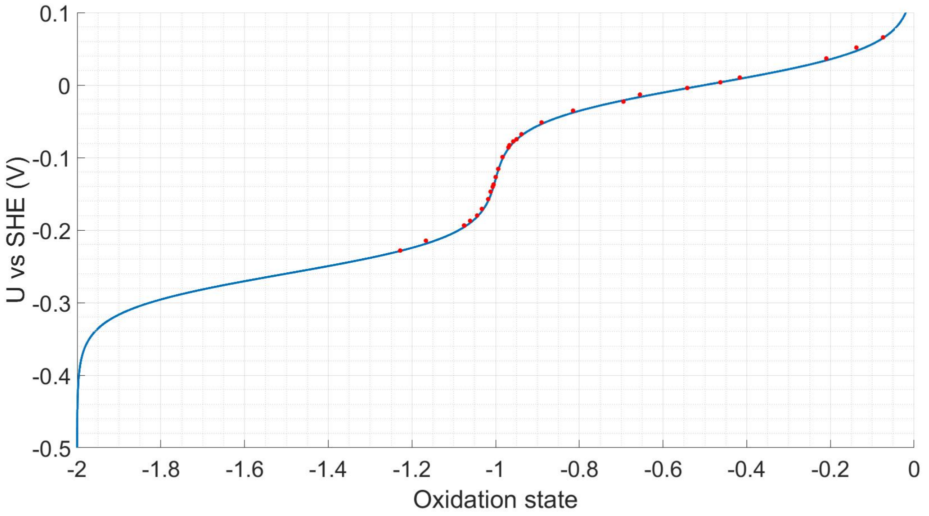

Figure 6.11 Comparison of the predicted reduction potential (blue line) and the experimentally observed results (red spots) vs oxidation state of SiW_{12} in 1 M NaCl.

the electrode surface (in this case from contaminants, e.g. airborne particles, impurities carried in via the nitrogen for purging, leaching from tubing and electrochemical cell, etc.) leading to the formation of a mixed potential. Due to the typically high standard rate constant for POM electron transfer, the possible contribution of contaminants' redox reactions towards a mixed potential is expected to be low. [24, 25, 79]

Since the OCP and U are in good agreement, an additional experiment was carried out: SiW_{12} was continuously electrolysed in the RFB with a 10 mA current until an oxidation state of ca. -1.9 was achieved. During this time, the open circuit potential in the reservoir was continuously recorded. The low current resulted in extremely slow electrolysis, so the oxidation state of the solution in the reservoir and the redox flow battery can be approximated as being homogeneous at any given time throughout the course of the measurement. This allows for direct comparisons of the open circuit potential recorded in the reservoir with the oxidation state according to coulomb counting. It also allows for comparison with the predictions of equation 6.11, as shown in figure 6.13.

It was observed that the highest discrepancy between the predicted and

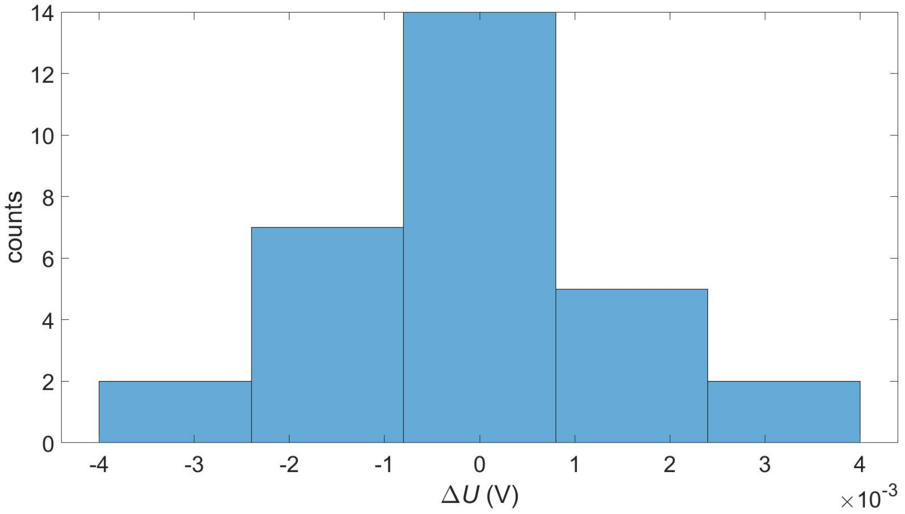

Figure 6.12 Histogram showing the discrepancy between the reduction potential and the open circuit potential for all datasets in this series. In this case, ΔU is defined as $\Delta U = OCP - U$.

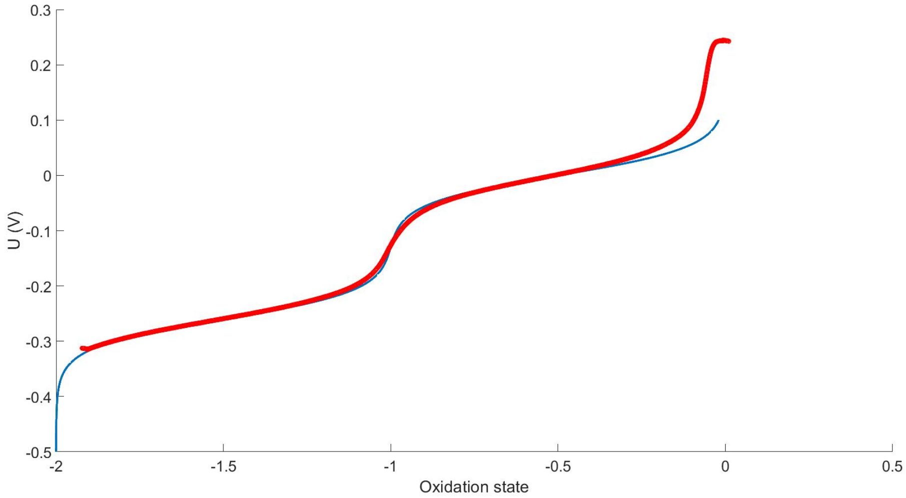

Figure 6.13 Comparison of the open circuit potential in the reservoir (red line) to the predictions of equation 6.11 (blue line) throughout the bulk electrolysis procedure.

observed potential occurred when the oxidation state was close to zero. The exchange current of a redox reaction decreases rapidly when the ratio of the oxidised and reduced species approaches either very small or very large values. Given that this is the case at oxidation states near zero, the observed discrepancy is not unexpected. Additionally, the contribution of contaminants towards a mixed potential becomes more significant when the exchange current attributable to the contaminants rises with respect to the exchange current of the species of interest.

Another point of interest in figure 6.13 is when the oxidation state is near -1. Close inspection shows that the experimental slope $\left(\frac{d(U)}{d(S_{ox})}\right)$ in this region is smaller than expected. The explanation for this is that in this region, the largest change in reduction potential relative to oxidation state occurs. Therefore, the OCP measurement is more sensitive to inhomogeneity in the oxidation state. A certain degree of inhomogeneity is expected and tolerated because perfect instantaneous mixing, even at high pump rates, is unattainable. Consequently, at any given time, it is expected that there is a slight local deviation in the oxidation state at the reservoir working electrode interface, which is placed at the centre of the reservoir.

Despite the aforementioned points, we see that the recorded potential agrees very well with the predicted values of equation 6.11. Using two different experimental techniques, we have shown that the predicted reduction potential agrees very well with the experimentally observed reduction potential for a given oxidation state.

With the relationship between oxidation state and reduction potential established, we now demonstrate that the predicted concentration profile for this system (figure 6.14) is also in line with experimental observations. However, experimentally differentiating between the discreet oxidation states poses a challenge.

Fully oxidised solutions of SiW_{12} in its pure form are entirely colourless, or in some rare instances, a light shade of pink (as per our own observations). Reducing the SiW_{12} results in the formation of a deep blue solution. Indeed, this is perhaps the property for which tungsten and especially molybdenum POMs are best known, as this class of molecules is also described as heteropoly blues

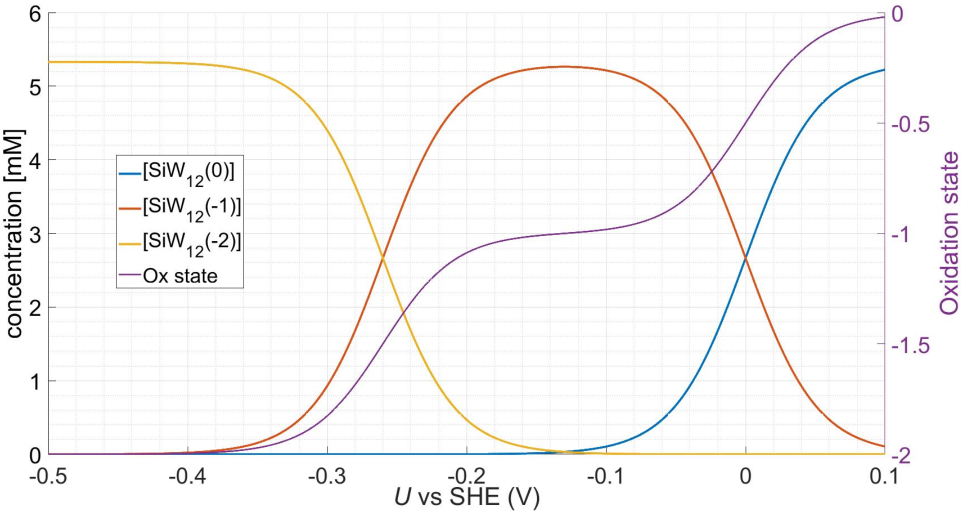

Figure 6.14 The concentration profile for SiW_{12} in the stationary cell experiments and the oxidation state vs reduction potential.

[20]. However, we have been unable to relate this property in a quantitative fashion and it is unclear if the two reduced oxidation states of interest here have absorbtion profiles different enough for reliable distinction. The molar attenuation coefficient is so high that samples with a concentration of ≥ 1 mM have an absorbance too large to be measurable with the spectroscopy equipment available to us, even after reducing the path length to 1 mm. In addition, the reduced POMs are sensitive to air oxidation, which could not entirely be avoided when pumping samples between the cell and the spectroscopy equipment.

^{183}W is NMR active, but measurements suffer from its very low sensitivity, necessitating specialised equipment and time consuming measurements. Therefore, analysing a large amount of samples via NMR was not feasible.

Measuring the electrochemical kinetics of the solution seemed the most reasonable approach. Disregarding the contribution of possible contaminants to the solution, there are two possible redox reactions which can occur to a significant extent:

$$\begin{aligned} &\mathrm{SiW_{12}(0) + e^- \rightleftharpoons SiW_{12}(-1)} && U^o_{(0)\rightleftharpoons(-1)}\,vs\,SHE = 0.00\,V \\ &\mathrm{SiW_{12}(-1) + e^- \rightleftharpoons SiW_{12}(-2)} && U^o_{(-1)\rightleftharpoons(-2)}\,vs\,SHE = -0.26\,V \end{aligned}$$

Provided that the rate limiting step is an elementary electron transfer from the POM to the electrode, the exchange current can be defined as:

$$j_0 = zFk_0(c_O^\alpha c_R^\beta) \tag{6.32}$$

where c_O and c_R are the concentrations of the reduced and oxidised species of interest, α and β are the anodic and cathodic charge transfer coefficients, which we assume to be 0.5, k_0 is the standard rate constant associated with the electron transfer.

Following the convention set out in section 6.2.4, i.e. associating letters to the species of interest starting from the lowest oxidation state, we define the concentration of the species of interest as: $[\mathrm{SiW}_{12}(-2)] = A$, $[\mathrm{SiW}_{12}(-1)] = B$ and $[\mathrm{SiW}_{12}(0)] = C$. The absence of $\mathrm{SiW}_{12}(-4)$ should be noted here, as it is only present in negligible quantities over the oxidation state range being investigated. The total exchange current density can be defined as:

$$j_{0(AB)} = Fk_{0(AB)}(B^\alpha A^\beta) \tag{6.33}$$

$$j_{0(BC)} = Fk_{0(BC)}(C^\alpha B^\beta) \tag{6.34}$$

$$j_{0(tot)} = (j_{0(AB)} + j_{0(BC)}) \tag{6.35}$$

where j is the current density. Assuming $\alpha = \beta = 0.5$, equations 6.33 and 6.34 predict that the exchange current reaches a local maximum when the reduced and oxidised species are present in equal proportions, i.e. when $S_{Ox} = -1.5$, -0.5. According to equation 6.35, a local minimum will be present at $S_{Ox} = -1$. The datasets that were used to determine reduction potential can also be used to determine $j_{0(tot)}$. Under kinetically controlled conditions at small overpotentials, the slope depicted in figure 6.10 is defined by:

$$j = j_0 \frac{zF}{RT} \Delta U \tag{6.36}$$

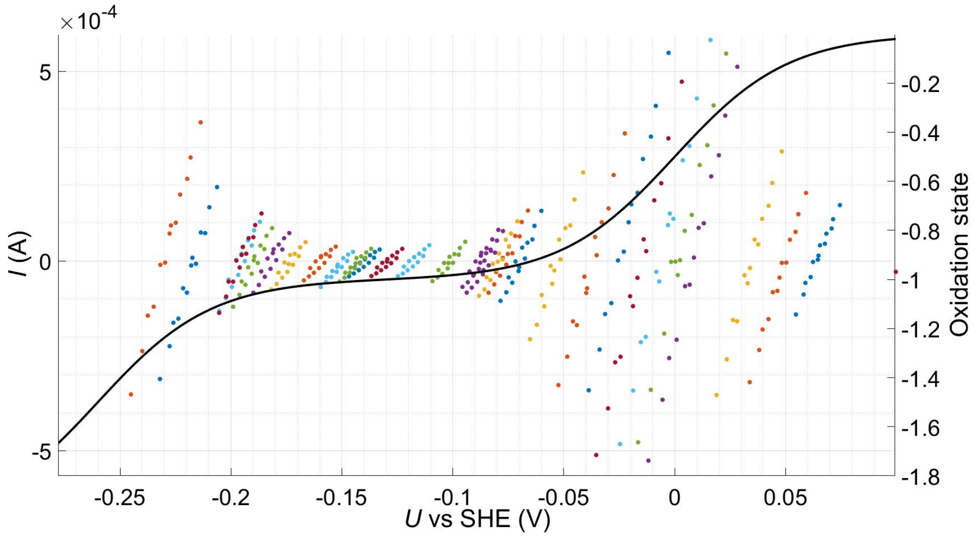

Figure 6.15 Current vs potential for SiW_{12} samples at varied oxidation state (varied open circuit potential), where each of the coloured series represents a different open circuit potential and each dot of the same colour the stabilised current at a potential perturbation. For each dataset, the potential perturbations are equivalent. The black line is the oxidation state vs reduction potential.

Hence, the slope is proportional to the exchange current. Figure 6.15 (data recorded as described in section 6.3.1, page 102) shows that, starting from $S_{Ox} = 0$, the slope for each individual dataset increases until $S_{Ox} = -0.5$ and then steadily decreases until the slope reaches a minimum at $S_{Ox} = -1$ and then rises again. Qualitatively, this is in line with the prediction. However, for a quantitative comparison, we must first determine the standard rate constants.

Figure 6.14 depicts the modelled concentration profile with respect to potential. Therefore, if k_0 for each reaction can be determined, the expected value for $j_{0(tot)}$ at any given oxidation state can be calculated. This value can then be compared with experimentally derived values of $j_{0(tot)}$ according to equation 6.36.

We see that at $S_{Ox} = -0.5$, the concentration of species $SiW_{12}(-2)$ (A) is negligible and similarly, at $S_{Ox} = -1.5$, the concentration of $SiW_{12}(0)$ (C) is negligible. Therefore, any measurement of the electrochemical kinetics carried out at these oxidation states can be fully attributed to the reactions $SiW_{12}(0) + e^- \rightleftharpoons SiW_{12}(-1)$ and $SiW_{12}(-1) + e^- \rightleftharpoons SiW_{12}(-2)$, respectively.

Table 6.2 EIS equivalent circuit element values

Element	$S = -0.5$	$S = -1.5$
R1	$16.9\,\Omega$	$17.5\,\Omega$
Q2	$4.057 * 10^{-6}$ F $\mathrm{s}^{(a-1)}$	$4.057 * 10^{-6}$ F $\mathrm{s}^{(a-1)}$
a1	0.7988	0.7988
R2	$131.0\,\Omega$	$166.4\,\Omega$
s1	$2882\,\Omega\ \mathrm{s}^{-1/2}$	$3014\,\Omega\ \mathrm{s}^{-1/2}$

Table 6.3 Measured k_0 values

Reaction	j vs U slope	PEIS
$\mathrm{SiW_{12}(0) + e^- \rightleftharpoons SiW_{12}(-1)}$	$4.7 \cdot 10^{-3}$ cm s^{-1}	$5.39 \cdot 10^{-3}$ cm s^{-1}
$\mathrm{SiW_{12}(-1) + e^- \rightleftharpoons SiW_{12}(-2)}$	$3.61 \cdot 10^{-3}$ cm s^{-1}	$4.25 \cdot 10^{-3}$ cm s^{-1}

The k_0 for each reaction was determined using two independent techniques. Perturbing the potential by a small amount relative to the open circuit potential and recording the steady state current for different potential perturbations results in a slope which is defined by equation 6.36. The exchange current was inserted into equations 6.33 and 6.34 for $S_{Ox} = -0.5$, where $B = C = 2.66$ mM and for $S_{Ox} = -1.5$, where $A = B = 2.66$ mM. All transfer coefficients are assumed to be 0.5.

Additionally, electrochemical impedance spectra at both oxidation states were also recorded in the reservoir under stationary conditions. The spectra and their fits are displayed in figure 6.16 and the equivalent circuit used for the fit is displayed in figure 6.17. Table 6.2 displays the fitted values for each circuit element. The value of interest here is the charge transfer resistance R_{CT}, as this value, for an elementary single electron transfer, relates to the exchange current by equation 6.37:

$$R_{CT} = \frac{RT}{FI_0} \tag{6.37}$$

Substitution of j_0 into equations 6.33 and 6.34 allows the k_0 for each reaction to be determined (table 6.3).

There is some variation between the calculated k_0 values depending on the

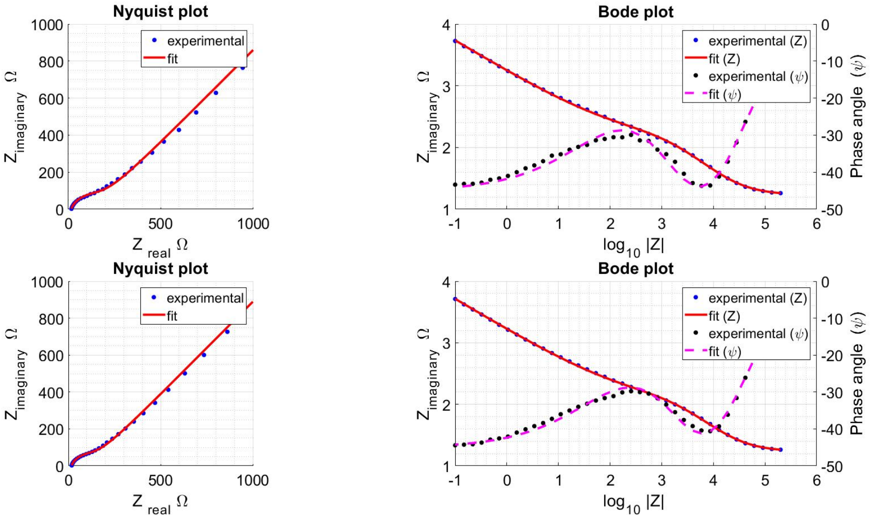

Figure 6.16 Nyquist and Bode plots for SiW_{12} in 1 M NaCl reduced to $S_{Ox} = -1.5$ (top) and $S_{Ox} = -0.5$ (bottom) on a glassy carbon disk electrode (stationary experiment setup). Nyquist plots display is limited to 1000 Ω for clarity of features.

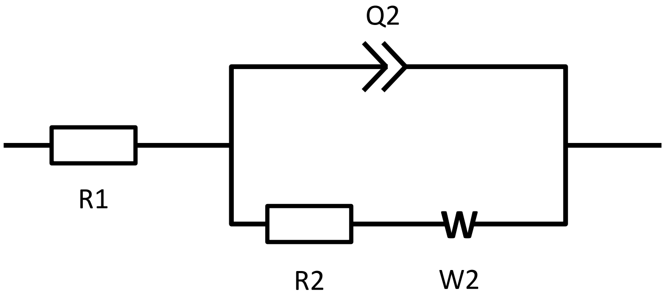

Figure 6.17 Equivalent circuit used for fitting the impedance spectra

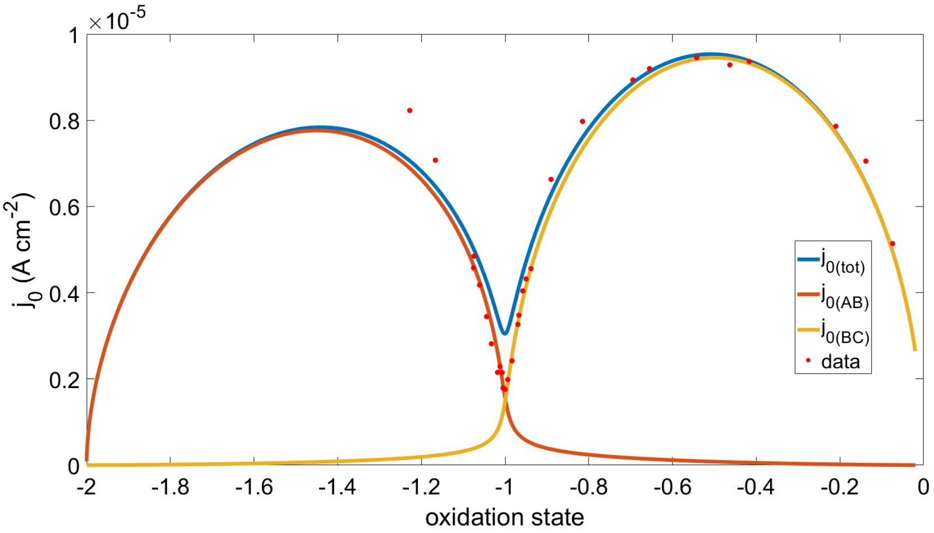

Figure 6.18 Exchange current density vs oxidation state. Exchange current densities predicted by equations 6.33 (yellow), 6.34 (orange), 6.35 (blue) and the experimentally derived values (red dots). Fitted parameters: $k_{0(BC)} = 5.2 \cdot 10^{-3}$ cm s^{-1} and $k_{0(CD)} = 4.25 \cdot 10^{-3}$ cm s^{-1}

technique applied, but the values are reasonably close together.

Now that the standard rate constants are established, the expected total exchange current can be calculated from equations 6.33 - 6.35. The result of which is plotted in figure 6.18 with the experimental values overlaid.

In general, the experimental results agree very well with the predicted values. However, we see that when $S_{Ox} = -1$ (figure 6.18) there is a small, but still significant deviation from the predicted value. The cause of this deviation becomes apparent when considering the combined effects of mass transport and significant depletion of species A and C when $S_{Ox} \approx -1$.

There are numerous ways to determine the limiting current for a given system. Perhaps the simplest method is through observation of the maximum current in a Tafel plot which features a plateau. Figure 6.19 shows that the limiting current $i_{l_{a/c}} \approx 1.4\,\mu\mathrm{A}$ when $S_{Ox} = -0.5$ (The increasingly negative gradient at $-200\,\mathrm{mV}$ is due to the onset of the AB reaction). Assuming that the limiting current is proportional to the concentration of species (A, B, and C), we can estimate the limiting anodic and cathodic currents for any given oxidation state (figure 6.20).

Qualitatively, it can now be seen that in the region where $S_{Ox} = -1$, the

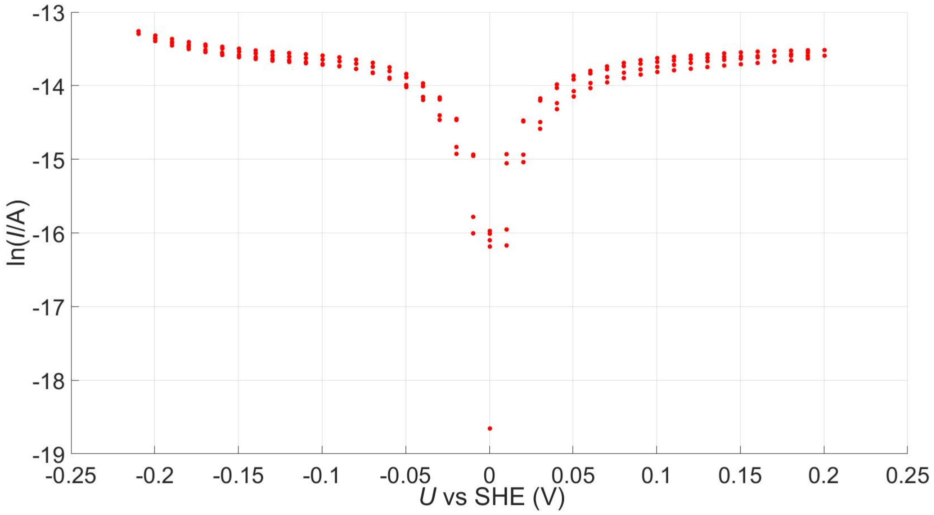

Figure 6.19 Tafel plot for SiW_{12} 5.33 mM in 1 M NaCl when $S_{Ox} = -0.5$.

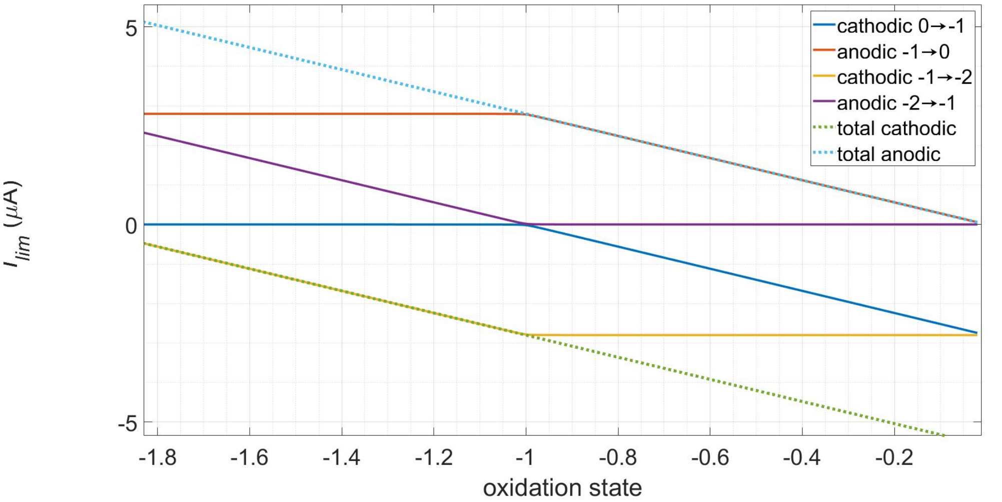

Figure 6.20 The limiting currents associated with each reaction, calculated from the value acquired from figure 6.19 ($i_{l_{a/c}} \approx 1.4\,\mu\mathrm{A}$) and assuming proportionality to the concentrations A, B, and C.

limiting anodic current for the BC reaction and the limiting cathodic current for the AB reaction are low relative to the overall current. Equations 6.33 - 6.35 adequately describe the behaviour for a kinetically controlled system at low overpotential. However, since we have established that mass transport has a considerable influence on this system, these equations are insufficient and the application of a more sophisticated model is necessary.

6.4.2 Rotating disk electrode experiment discussion

There are multiple advantages of using an RDE to record current vs potential plots, such as:

- The time required to attain a steady state current (depicted in figure 6.8) is less than 1 second at 5000 rpm. Therefore, data for a given oxidation state can be produced in 1-2 minutes (as thorough mixing is still necessary), ensuring that the effects of O_2 ingress are minimised. Additionally, the small timeframe allows many datasets over a large range of oxidation states to be collected in a timely fashion.
- The material flux in the vicinity of the RDE (the reservoir) is high enough that the flux from pumping to the flow cell can be ignored during measurement. Therefore, the procedure for measuring over different oxidation states can be easily automated.
- The applied potential range can be extended to high values ($\pm$ 250 mV) with little effect on data collection time. We can then analyse the kinetic and mass transport properties at a given oxidation state.
- As can be seen in figures 6.10 and 6.19, there is significant hysteresis when a stationary electrode is used. This probably occurs as a result of small differences in the density: It was observed that on reduction of SiW_{12} the newly generated blue material sank to the bottom of the reaction vessel, hardly mixing with the surrounding liquid. This induced uncontrolled convection in the vicinity of the working electrode. With the RDE at 5000 rpm, these effects are mitigated by forced convection in the vicinity of the working electrode surface.

Assuming that the rate limiting step is an elementary electron transfer process from the POM to the electrode and vice versa, the processes at the electrode can be adequately described by the extended current-overpotential relationship[65]:

$$j = j_0 \left[\left(1 - \frac{j}{j_{l,a}}\right) e^{\alpha f \eta} - \left(1 - \frac{j}{j_{l,c}}\right) e^{-\beta f \eta} \right] \tag{6.38}$$

where η = activation overpotential and f is defined as $\frac{nF}{RT}$. This can be rearranged for j:

$$j = \frac{j_0(e^{\alpha f \eta} - e^{-\beta f \eta})}{j_0(\frac{e^{\alpha f \eta}}{j_{l,a}} - \frac{e^{-\beta f \eta}}{j_{l,c}}) + 1} \tag{6.39}$$

Over the potential range studied in this experiment, there are four associated redox couples (figure 6.9). Consequently, there are five possible oxidation states, since the third reduction reaction of SiW_{12}, a two-electron reaction, is split into two one-electron reactions at this pH. According to the previous conventions, the concentrations of the various states are assigned A, B, C, D, E, starting from the lowest oxidation state, e.g. $[SiW_{12}(-4)] = A$. The redox reactions are as follows:

$SiW_{12}(0) + e^- \rightleftharpoons SiW_{12}(-1)$ U^o vs SHE = 0.00 V
$SiW_{12}(-1) + e^- \rightleftharpoons SiW_{12}(-2)$ U^o vs SHE = -0.26 V
$SiW_{12}(-2) + e^- \rightleftharpoons SiW_{12}(-3)$ U^o vs SHE = -0.65 V
$SiW_{12}(-3) + e^- \rightleftharpoons SiW_{12}(-4)$ U^o vs SHE = -0.87 V

Equation 6.39 gives the current at a given overpotential for a single redox couple, so the total current will be the sum of the currents according to equation 6.39 for all associated redox couples:

$$j_{tot} = j_{AB} + j_{BC} + j_{CD} + j_{DE} \tag{6.40}$$

Typically, the kinetic parameters for an electrochemical system are determined through analysing a Tafel plot. A typical analysis involves extrapolating along the linear regions in the $\log(j)$ vs U plot of the anodic and cathodic branch to zero overpotential. The value of the current density (j) at the abscissa intercept is taken to be the exchange current density and from this the rate constant can be calculated. The challenge here is that the onset of the linear region is very rarely clear-cut in experimental data, leaving the analysis of the data very much up to the interpretation of the individual researcher. Consciously or otherwise, this can lead to the researcher forming conclusions which support a preferred narrative. Moreover, this type of analysis would be insufficient to explain the kinetics arising from equation 6.40.

Given the wide availability of fitting tools in commonly used software (Excel, MATLAB etc.), it seems preferable to fit the experimental data directly to equation 6.40. If the system obeys the equation then a good fit will be achieved and the parameters will be calculated with much less ambiguity. If no good fit can be found, then this can potentially indicate that the underlying chemistry is more complex and/or different than anticipated. Furthermore, the application of a model to a series of Tafel plots taken over a large oxidation state range allows for a richer understanding of the kinetic and mass-transport parameters.

Data processing methodology

There are four associated redox couples of interest within the potential range studied in this experiment. Assuming that all four follow Butler-Volmer kinetics then equation 6.40 should describe the system. The expanded form of equation 6.40 is not displayed here for the sake of brevity, but it can be seen from equation 6.39 that there are a large number of variables (24 in total) which need to be fitted if an exact solution is to be found (table 6.4).

A number of approaches were taken in order to fit this data. The first and largely unsuccessful attempt was to fit all variables listed in table 6.4 to equation 6.40. This is achieved using the built-in MATLAB fitting function which, by default, uses the non-linear least squares method to fit a dataset to a pre-defined model. Major problems arose due to both the large number of variables involved and the range of their respective impacts to the overall current for a given

Equation term	Contained variables
j_{AB}	$[\mathrm{SiW}_{12}(-4)]$, $[\mathrm{SiW}_{12}(-3)]$, α_{AB}, β_{AB}, $k_{0_{AB}}$, $j_{l,a_{(AB)}}$ $j_{l,c_{(AB)}}$
j_{BC}	$[\mathrm{SiW}_{12}(-3)]$, $[\mathrm{SiW}_{12}(-2)]$, α_{BC}, β_{BC}, $k_{0_{BC}}$, $j_{l,a_{(BC)}}$ $j_{l,c_{(BC)}}$
j_{CD}	$[\mathrm{SiW}_{12}(-2)]$, $[\mathrm{SiW}_{12}(-1)]$, α_{CD}, β_{CD}, $k_{0_{CD}}$, $j_{l,a_{(CD)}}$ $j_{l,c_{(CD)}}$
j_{DE}	$[\mathrm{SiW}_{12}(-1)]$, $[\mathrm{SiW}_{12}(0)]$, α_{DE}, β_{DE}, $k_{0_{DE}}$, $j_{l,a_{(DE)}}$ $j_{l,c_{(DE)}}$

Table 6.4 Variables to be fitted

oxidation state. For example, when $S_{Ox} < -3$, the contribution of the j_{DE} is essentially 0.

We also encountered the obstacle that such fitting programs are generally unable to overcome the problem of localised minima. The fitting procedure works by changing the starting value in an iterative process until a decrease in the residual squares is no longer achievable. This can be problematic when both local and global minima are present. Hence, it is advisable to test a wide variety of starting values over a sensible range. However, for multivariate problems, the fitting procedure becomes computationally exhaustive very fast. If 10 starting values are tried for every variable, then there are 10^{24} possible combinations which need to be calculated and tracked.

The model is therefore simplified in the following ways:

- In section 6.4.1 we showed that the SiW_{12} example case is verifiable, in the sense that the reduction potential accurately behaves as predicted and that we can calculate the distribution of species for any given oxidation state. We therefore treat the concentrations of species as constants for a given oxidation state based on a modified form of equation 6.28 that includes five oxidation states.

- In section 6.4.1 we also presented two different ways of calculating the standard rate constant for each redox reaction. We use this data as starting values in the least squares fitting procedure.

- From a Tafel plot at $S_{Ox} = -0.5$ it was found that the limiting current density can be approximated as $0.567\,\mathrm{mA\ cm^{-2}\ mM^{-1}}$. Since no significant changes in molecule size or solvation shell are expected [80] and since the total concentration of SiW_{12} is small, the limiting current is assumed to be directly proportional to the concentration for all oxidation states. Hence, we apply this relation to all limiting current variables listed in table 6.4. For instance, if $A = 1$ mM, prior to fitting $j_{l,c(AB)} = 0.567\,\mathrm{mA\ cm^{-2}}$.

- As the SiW_{12} redox couples are well separated and because the potential range of the Tafel plots studied herein does not obviously exhibit characteristics associated with more than two redox reactions occurring simultaneously, we simplify equation 6.40 to include only the two most relevant redox reactions for a given oxidation state. This is achieved using the following conditions:

  - If $A+B+C > B+C+D$ and $A+B+C > C+D+E \Rightarrow j \approx j_{AB} + j_{BC}$
  - If $B+C+D > A+B+C$ and $B+C+D > C+D+E \Rightarrow j \approx j_{BC} + j_{CD}$
  - If $C+D+E > A+B+C$ and $C+D+E > B+C+D \Rightarrow j \approx j_{CD} + j_{DE}$

- Sensible bounds were placed on all variables. We know, for instance, that the limiting anodic current cannot be negative and is also probably not more than twice the value calculated from the Tafel plot (as described above), i.e. not more than $2 \cdot 0.567\,\mathrm{mA\,cm^{-2}mM^{-1}}$. Likewise, the limiting cathodic current is likely between 0 and $-2 \cdot 0.567\,\mathrm{mA\,cm^{-2}mM^{-1}}$ and the transfer coefficients are likely between 0 and 1. All of the standard rate constants are likely between 10^{-1} cm $\mathrm{s^{-1}}$ and $10^{-5}\,\mathrm{cm\,s^{-1}}$.

Processed data discussion

The total data collected amounts to 800 Tafel plots, which for obvious reasons cannot be displayed here, but an illustrative sample of the data is displayed in figure 6.21. Each of the Tafel plots exhibits features which justify our approach over a typical Tafel plot analysis:

- $U = -0.75\,\mathrm{V}$ vs SHE: The cathodic branch profile does not exhibit typical behaviour for a single-electron reaction (i.e. a single slope). Instead, this branch exhibits a kink with noticeably different slopes before and after, indicating two different reactions. On the anodic branch, the limiting current is reached at very low overpotential due to the low concentration of $\mathrm{SiW_{12}}(-2)$. A typical Tafel analysis would be prone to error in this case, because the region in which the reaction is purely under kinetic control is very small. Additionally, at high overpotential the contribution of j_{BC} becomes significant.

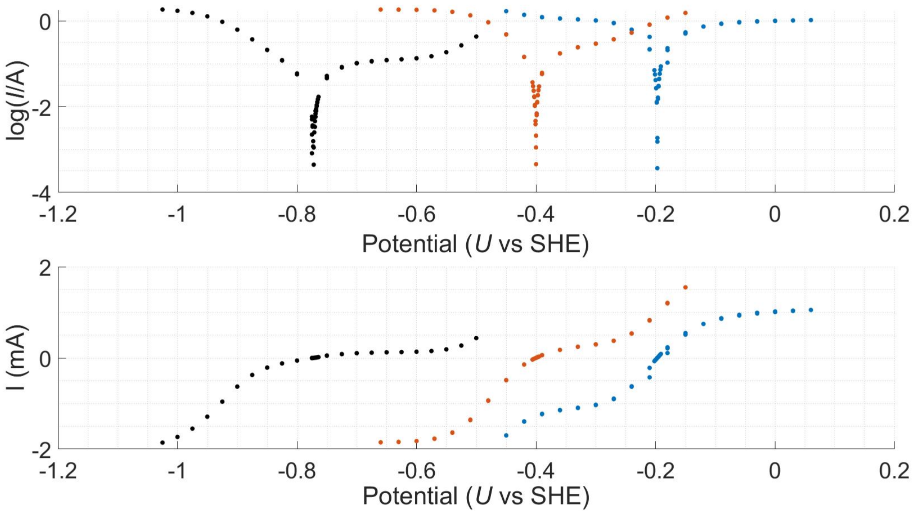

Figure 6.21 Selected Tafel plots of a SiW_{12} solution with different potentials. The top and bottom graphs are the same data in semi-log and non-logarithmic representations, respectively.

- $U = -0.40$V vs SHE: The anodic branch exhibits behaviour of two reactions with different standard reduction potentials.
- $U = -0.20$ V vs SHE: The cathodic branch exhibits behaviour of two reactions with different standard reduction potentials.

In each of these cases, the potential range of the segment that would be analysed in a typical Tafel analysis is small and therefore evaluation of the kinetic parameters is prone to error. Figures 6.22 - 6.24 show kinetic and mass transport parameters derived from the 800 Tafel plots generated throughout the experiment. As described above, we simplified equation 6.40 to include only the two most relevant redox reactions for any given oxidation state. For figures 6.22 - 6.24 this means that each of the respective reaction parameters was calculated for the oxidation state range of the two redox reactions where they were most relevant. As anticipated, figure 6.22 shows that the spread of values for k_0 for any given redox reaction is quite small. There are several outliers, which are likely due to erroneous fitting. However, other values which are inconsistent with the trend, such as the increase in k_0 for the $E \rightleftharpoons D$ at an oxidation state of around -0.9, could be due to the effect of slight temperature changes in the system. Even

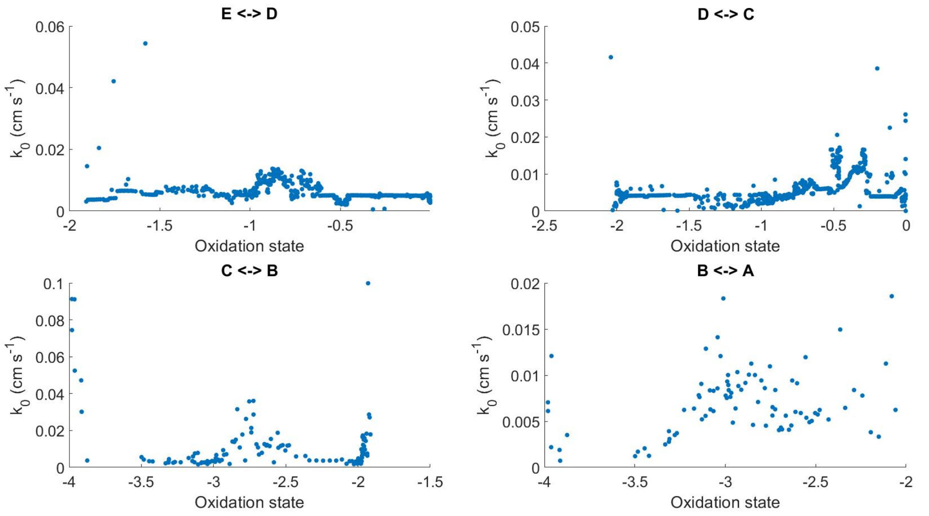

Figure 6.22 Fitted values for the standard rate constant of each reaction. The values of k_0 for all four redox reactions were calculated over the oxidation state range of the two redox reactions where they were most relevant.

though the temperature was not controlled in this experimental setup, the results are remarkably consistent to themselves and to results reported in the literature [24, 25]. The intention here is to illustrate that useful information about an electrochemical system with multiple associated redox couples can be easily and accurately determined using the methods described in this chapter.

It is apparent that, as the oxidation state decreases, the data is generally more scattered. This is especially true for the values of the electron transfer constant for the $B \rightleftharpoons A$ reaction. One possible explanation for this is that oxygen ingress leads to reoxidation of the POM as the Tafel plots are being recorded. This seems likely, given that the purge gas used in this experiment was provided from an in-house system, generated through a pressure swing absorption method, which leads to a relatively low purity compared to distillation. Furthermore, it is expected that oxygen from the lab atmosphere permeates the Norprene tubing leading to and from the flow cell to a certain extent. Additionally, at certain points U of the solution is in the region of -1 V vs SHE, so the thermodynamic driving force for oxidation is significant.

Another possible explanation is that at such low potentials at least some

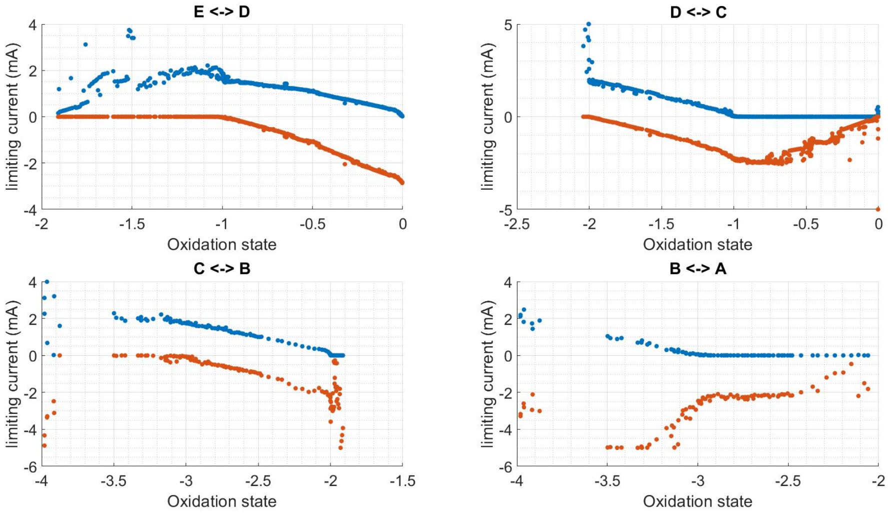

Figure 6.23 Fitted cathodic (orange) and anodic (blue) limiting currents for each reaction.

hydrogen was generated at both the rotating disk electrode surface and the flow cell electrode surface. As a consequence of the competing reaction, the data at low potentials may be erroneous. Data for the $B \rightleftharpoons A$ reaction at oxidation states < -3.0 supports this hypothesis. At this point, with decreasing oxidation state, the limiting cathodic current increases much faster than anticipated (figure 6.23). The peak (most negative) values associated with the $B \rightleftharpoons A$ reaction are also much higher than that observed for the other reactions.

The limiting current generally behaves as expected, as shown in figure 6.23. For example, at $S_{Ox} = 0$, the limiting current for the anodic process of the $D \rightleftharpoons E$ reaction is essentially 0. As the oxidation state decreases, the magnitude of the limiting currents for both the anodic and cathode processes increases linearly. They are roughly equal when $S_{Ox} = -0.5$ and the limiting current for the cathodic process drops to 0 when $S_{Ox} = -1$ and the limiting current for the cathodic process is at a maximum. At this point the concentration of species $\mathrm{SiW_{12}}(0)$ (E) in solution is basically zero, so the limiting cathodic current for the $D \rightleftharpoons E$ remains at zero. Also, the concentration of species $\mathrm{SiW_{12}}(-1)$ (D) decreases as the oxidation state decreases to $S_{Ox} = -2$, meaning that the limiting current of the anodic process also decreases (roughly) linearly towards

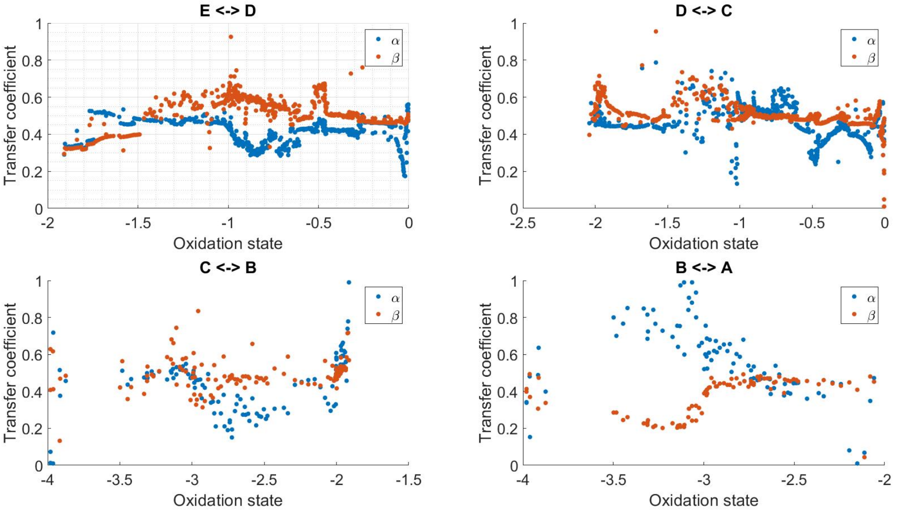

Figure 6.24 Anodic (blue) and cathodic (orange) charge transfer coefficients for each reaction.

0. The main outlier is the cathodic process for the $D \rightleftharpoons E$ reaction. Given that these values were generated using a least squares approach, the values presented in figure 6.23 provide evidence that supports our interpretation of the electrochemical system.

The transfer coefficients were derived as part of the procedure and are shown in figure 6.24. There is no clear trend or pattern to the reported values. The values associated with the $D \rightleftharpoons E$ and $C \rightleftharpoons D$ reactions have a reasonably low spread and show that the reaction is approximately symmetrical regardless of oxidation state. The values for the $C \rightleftharpoons B$ reaction are less consistent and the sum of the transfer coefficients for any given oxidation state is less than one. This potentially indicates that the rate limiting step for the $C \rightleftharpoons B$ reaction is not an elementary electron transfer reaction.

The transfer coefficient values for the $B \rightleftharpoons A$ seem to diverge as the oxidation state decreases (α_{AB} increases while β_{AB} decreases). As can be seen in figure 6.9, the standard potential for this reaction is -0.85 V vs SHE. Additionally, there is a plateau present on the cathodic sweep at -1.15 V vs SHE and a corresponding plateau on the anodic sweep at approximately -1.1 V vs SHE, indicating that this reaction is reversible (to some extent). The plateau is attributed to either the adsorption of hydrogen onto the electrode, or a reduction of SiW_{12}(-4) to SiW_{12}(-5). A further unresolved feature forming at -1.25 V vs SHE (without a corresponding anodic peak/plateau) is attributed to hydrogen evolution, since this process is irreversible under the experimental conditions described in the caption of figure 6.9.

The reactions which are accounted for to fit the data are SiW_{12}(-4) $\rightleftharpoons$ SiW_{12}(-3) and SiW_{12}(-3) $\rightleftharpoons$ SiW_{12}(-2). However, the processes occurring at -1.15 V and -1.1 V vs SHE are not. At an oxidation state of $\sim$ -3.5 ($U \leq$ -0.85 V vs SHE) this is problematic because the data accumulated on the cathodic branch of the Tafel plot will be influenced by the reactions centred around at -1.15 V and -1.1 V vs SHE.

In other words, the fitting procedure is attempting to find the best fit for a process which involves three or four reactions to the equation $I = I_{AB} + I_{BC}$. In this case, the Tafel plot is asymmetrical, with the current response being more pronounced on the anodic branch. This manifests as a decrease in the cathodic transfer coefficient and an increase in the anodic transfer coefficient, as this leads to the best fit.

6.5 Conclusion

A description of the reduction potential and distribution of species at any given oxidation state for species with multiple associated redox couples has been detailed. An explicit solution was presented for species with two associated redox couples (i.e. three possible oxidation states), which allows for direct calculation of oxidation state and the concentration of species in different oxidation states from the reduction potential and vice versa.

For species with more than two redox couples, the situation is more complex. No general solution for any number of redox couples was found that relates the oxidation state to the reduction potential. An alternative solution was presented instead, which involves calculating the concentration of species and the oxidation state for a defined potential window and using the results as a lookup table.

Solutions of SiW_{12} in NaCl (aq., 1 M) were gradually reduced in an electrochemical cell and the reduction potential was measured at various different oxidation states. In addition, current-overpotential measurements were recorded in a stationary solution and on a rotating disk electrode. The data from these experiments shows that the kinetic parameters (i.e. the exchange current density and limiting currents) as well as the reduction potential are consistent with the values predicted by our description of the underlying thermodynamics.

Furthermore, useful electrochemical information (e.g. electron transfer constants, limiting currents and transfer coefficients) about the investigated system was extracted by rigorous application of thermodynamic principles. This also provides insight into how these variables may evolve as the oxidation state changes.

The next steps might involve testing various other electrochemical systems with two or more redox couples with increasing complexity. This can include closer spacing of standard reduction potentials, species with proton coupled electron transfers, etc. Results could then be compared to elucidate if the concepts described here yield similarly accurate predictions for more complex systems.

Chapter 7

Bibliography

(1) IEA, *Key World Energy Statistics 2021 – Statistics Report*, tech. rep., International Energy Agency, 2021.

(2) BP Statistical Reviews, *BP Statistical Review of World Energy 2022*, tech. rep., BP p.l.c., 2022.

(3) United Nations, *Report of the Conference of the Parties serving as the meeting of the Parties to the Paris Agreement on its third session*, tech. rep., United Nations, Glasgow, 2021, pp. 1–46.

(4) W. He, M. King, X. Luo, M. Dooner, D. Li and J. Wang, *Advances in Applied Energy*, 2021, **4**, 100060.

(5) G. Gautham Prasad, N. Shetty, S. Thakur, Rakshitha and K. B. Bommegowda, *IOP Conference Series: Materials Science and Engineering*, 2019, **561**, 012105.

(6) A. Olabi, C. Onumaegbu, T. Wilberforce, M. Ramadan, M. A. Abdelkareem and A. H. Al – Alami, *Energy*, 2021, **214**, 118987.

(7) S. Koohi-Fayegh and M. Rosen, *Journal of Energy Storage*, 2020, **27**, 101047.

(8) M. M. Rahman, A. O. Oni, E. Gemechu and A. Kumar, *Energy Conversion and Management*, 2020, **223**, 113295.

(9) I. Derr, M. Bruns, J. Langner, A. Fetyan, J. Melke and C. Roth, *Journal of Power Sources*, 2016, **325**, 351–359.

(10) X. Han, L. Lu, Y. Zheng, X. Feng, Z. Li, J. Li and M. Ouyang, *eTransportation*, 2019, **1**, 100005.

(11) H. Chen, J. E. H. Buston, J. Gill, D. Howard, R. C. E. Williams, C. M. Rao Vendra, A. Shelke and J. X. Wen, *Journal of Power Sources*, 2020, **472**, 228585.

(12) W. Kangro, *Verfahren zur Speicherung von elektrischer Energie*, German patent, DE914264C, 1954.

(13) L. H. Thaller, *Electrically Rechargeable Redox Flow Cells,* US patent, US3996064A, 1974.

(14) M. Skyllas-Kazacos, M. Rychick and R. Robins, *All-vanadium redox battery,* US patent, US4786567A, 1988.

(15) A. Shibata and K. Sato, *Power Engineering Journal*, 1999, **13**, 130–135.

(16) C. Choi, S. Kim, R. Kim, Y. Choi, S. Kim, H.-y. Jung, J. H. Yang and H.-T. Kim, *Renewable and Sustainable Energy Reviews*, 2017, **69**, 263–274.

(17) K. Lourenssen, J. Williams, F. Ahmadpour, R. Clemmer and S. Tasnim, *Journal of Energy Storage*, 2019, **25**, 100844.

(18) J. B. Quinn, T. Waldmann, K. Richter, M. Kasper and M. Wohlfahrt-Mehrens, *Journal of The Electrochemical Society*, 2018, **165**, A3284–A3291.

(19) J. Sun, D. Shi, H. Zhong, X. Li and H. Zhang, *Journal of Power Sources*, 2015, **294**, 562–568.

(20) M. T. Pope, *Heteropoly and Isopoly Oxometalates*, Springer-Verlag Berlin Heidelberg, Berlin, 1st edn., 1983.

(21) F. J. C. Rossotti, H. Rossotti, J. G. Ormerod, E. Stenhagen and B. Thorell, *Acta Chemica Scandinavica*, 1956, **10**, 957–984.

(22) M. R. Horn, A. Singh, S. Alomari, S. Goberna-Ferrón, R. Benages-Vilau, N. Chodankar, N. Motta, K. K. Ostrikov, J. MacLeod, P. Sonar, P. Gomez-Romero and D. Dubal, *Energy & Environmental Science*, 2021, **14**, 1652–1700.

(23) T. Akutagawa, R. Jin, R. Tunashima, S.-i. Noro, L. Cronin and T. Nakamura, *Langmuir*, 2008, **24**, 231–238.

(24) J. Friedl, M. V. Holland-Cunz, F. Cording, F. L. Pfanschilling, C. Wills, W. McFarlane, B. Schricker, R. Fleck, H. Wolfschmidt and U. Stimming, *Energy & Environmental Science*, 2018, **11**, 3010–3018.

(25) J. Friedl, F. L. Pfanschilling, M. V. Holland-Cunz, R. Fleck, B. Schricker, H. Wolfschmidt and U. Stimming, *Clean Energy*, 2019, **3**, 278–287.

(26) U. Kortz, S. Isber, M. H. Dickman and D. Ravot, *Inorganic Chemistry*, 2000, **39**, 2915–2922.

(27) C. M. Flynn and G. D. Stucky, *Inorganic Chemistry*, 1969, **8**, 332–334.

(28) J. Liu, F. Ortéga, P. Sethuraman, D. E. Katsoulis, C. E. Costello and M. T. Pope, *J. Chem. Soc., Dalton Trans.*, 1992, 1901–1906.

(29) G. Johansson, L.-O. Gullman, A. Kjekshus and R. Söderquist, *Acta Chemica Scandinavica*, 1960, **14**, 771–773.

(30) R. E. Schreiber, L. Avram and R. Neumann, *Chemistry - A European Journal*, 2018, **24**, 369–379.

(31) G Hervé, A Tézé and R Contant, in *Polyoxometalate Molecular Science*, ed. J. J. Borrás-Almenar, E. Coronado, A. Müller and M. Pope, Springer Netherlands, Dordrecht, 2003, pp. 33–54.

(32) A Selling, I Andersson, L Pettersson, C. M. Schramm, S. L. Downey and J. H. Grate, *Inorg. Chem.*, 1994, **33**, 3141–3150.

(33) E. Zanzola, C. Dennison, A. Battistel, P. Peljo, H. Vrubel, V. Amstutz and H. H. Girault, *Electrochimica Acta*, 2017, **235**, 664–671.

(34) K. Gong, F. Xu, J. B. Grunewald, X. Ma, Y. Zhao, S. Gu and Y. Yan, *ACS Energy Letters*, 2016, **1**, 89–93.

(35) T. Xue and H. J. Fan, *Journal of Energy Chemistry*, 2021, **54**, 194–201.

(36) B. Huskinson, M. P. Marshak, C. Suh, S. Er, M. R. Gerhardt, C. J. Galvin, X. Chen, A. Aspuru-Guzik, R. G. Gordon and M. J. Aziz, *Nature*, 2014, **505**, 195–198.

(37) M. L. Perry, K. E. Rodby and F. R. Brushett, *ACS Energy Letters*, 2022, **7**, 659–667.

(38) H. Tomiyasu, H. Shikata, K. Takao, N. Asanuma, S. Taruta and Y.-Y. Park, *Scientific Reports*, 2017, **7**, 45048.

(39) K. Gong, Q. Fang, S. Gu, S. F. Y. Li and Y. Yan, *Energy & Environmental Science*, 2015, **8**, 3515–3530.

(40) X. Wei, W. Xu, M. Vijayakumar, L. Cosimbescu, T. Liu, V. Sprenkle and W. Wang, *Advanced Materials*, 2014, **26**, 7649–7653.

(41) X. Xing, Q. Liu, B. Wang, J. P. Lemmon and W. Q. Xu, *Journal of Power Sources*, 2020, **445**, 227330.

(42) E. I. Romadina, D. S. Komarov, K. J. Stevenson and P. A. Troshin, *Chemical Communications*, 2021, **57**, 2986–2989.

(43) M. Li, Z. Rhodes, J. R. Cabrera-Pardo and S. D. Minteer, *Sustainable Energy & Fuels*, 2020, **4**, 4370–4389.

(44) E. Sánchez-Díez, E. Ventosa, M. Guarnieri, A. Trovò, C. Flox, R. Marcilla, F. Soavi, P. Mazur, E. Aranzabe and R. Ferret, *Journal of Power Sources*, 2021, **481**, 228804.

(45) J. Winsberg, T. Hagemann, T. Janoschka, M. D. Hager and U. S. Schubert, *Angewandte Chemie International Edition*, 2017, **56**, 686–711.

(46) L. Li, S. Kim, W. Wang, M. Vijayakumar, Z. Nie, B. Chen, J. Zhang, G. Xia, J. Hu, G. Graff, J. Liu and Z. Yang, *Advanced Energy Materials*, 2011, **1**, 394–400.

(47) S. Roe, C. Menictas and M. Skyllas-Kazacos, *Journal of The Electrochemical Society*, 2016, **163**, A5023–A5028.

(48) C. J. Barnhart and S. M. Benson, *Energy & Environmental Science*, 2013, **6**, 1083.

(49) U.S. Geological Survey, *Vanadium - Historical Statistics (Data Series 140)*, tech. rep., U.S. Geological Survey, 2022.

(50) D. G. Kwabi, K. Lin, Y. Ji, E. F. Kerr, M.-A. Goulet, D. De Porcellinis, D. P. Tabor, D. A. Pollack, A. Aspuru-Guzik, R. G. Gordon and M. J. Aziz, *Joule*, 2018, **2**, 1894–1906.

(51) E. S. Beh, D. De Porcellinis, R. L. Gracia, K. T. Xia, R. G. Gordon and M. J. Aziz, *ACS Energy Letters*, 2017, **2**, 639–644.

(52) M. Duduta, B. Ho, V. C. Wood, P. Limthongkul, V. E. Brunini, W. C. Carter and Y.-M. Chiang, *Advanced Energy Materials*, 2011, **1**, 511–516.

(53) J. J. Biendicho, C. Flox, L. Sanz and J. R. Morante, *ChemSusChem*, 2016, **9**, 1938–1944.

(54) Q. Huang, H. Li, M. Grätzel and Q. Wang, *Phys. Chem. Chem. Phys.*, 2013, **15**, 1793–1797.

(55) P. Leung, J. Palma, E. Garcia-Quismondo, L. Sanz, M. Mohamed and M. Anderson, *Journal of Power Sources*, 2016, **310**, 1–11.

(56) S. Selverston, E. Nagelli, J. S. Wainright and R. F. Savinell, *Journal of The Electrochemical Society*, 2019, **166**, A1725–A1731.

(57) M. Park, E. S. Beh, E. M. Fell, Y. Jing, E. F. Kerr, D. Porcellinis, M. Goulet, J. Ryu, A. A. Wong, R. G. Gordon, J. Cho and M. J. Aziz, *Advanced Energy Materials*, 2019, **9**, 1900694.

(58) A. Khor, P. Leung, M. Mohamed, C. Flox, Q. Xu, L. An, R. Wills, J. Morante and A. Shah, *Materials Today Energy*, 2018, **8**, 80–108.

(59) Q. Wang, S. M. Zakeeruddin, D. Wang, I. Exnar and M. Grätzel, *Angewandte Chemie International Edition*, 2006, **45**, 8197–8200.

(60) M. T. Pope and G. M. Varga, *Inorganic Chemistry*, 1966, **5**, 1249–1254.

(61) J. P. Launay, *Journal of Inorganic and Nuclear Chemistry*, 1976, **38**, 807–816.

(62) S. P. G. Y. Y. Wansheng and T. Zhorgyin, *Journal of Electrochemistry*, 1997, **3**, 71.

(63) Y. Liu, S. Lu, H. Wang, C. Yang, X. Su and Y. Xiang, *Advanced Energy Materials*, 2017, **7**, 1601224.

(64) H. D. Pratt, N. S. Hudak, X. Fang and T. M. Anderson, *Journal of Power Sources*, 2013, **236**, 259–264.

(65) R Bard, Allen J.; Faulkner, Larry, *Electrochemical Methods: Fundamentals and Applications*, Wiley New York, 2001.

(66) S. V. Bhosale, C. H. Jani and S. J. Langford, *Chemical Society Reviews*, 2008, **37**, 331–342.

(67) B. Gómez-Lor, G. Hennrich, B. Alonso, A. Monge, E. Gutierrez-Puebla and A. M. Echavarren, *Angewandte Chemie - International Edition*, 2006, **45**, 4491–4494.

(68) B. Gómez-Lor, B. Alonso, A. Omenat and J. L. Serrano, *Chem. Commun.*, 2006, 5012–5014.

(69) S. Gámez-Valenzuela, A. Benito-Hernández, M. Echeverri, E. Gutierrez-Puebla, R. Ponce Ortiz, M. C. Ruiz Delgado and B. Gómez-Lor, *Molecules*, 2022, **27**, 1121.

(70) H. V. Schröder and C. A. Schalley, *Beilstein Journal of Organic Chemistry*, 2018, **14**, 2163–2185.

(71) C. Granqvist and A. Hultåker, *Thin Solid Films*, 2002, **411**, 1–5.

(72) C. M. Cardona, W. Li, A. E. Kaifer, D. Stockdale and G. C. Bazan, *Advanced Materials*, 2011, **23**, 2247–2383.

(73) T. J. Curphey, J. O. Santer, M. Rosenblum and J. H. Richards, *Journal of the American Chemical Society*, 1960, **82**, 5249–5250.

(74) M. Malischewski, K. Seppelt, J. Sutter, F. W. Heinemann, B. Dittrich and K. Meyer, *Angewandte Chemie International Edition*, 2017, **56**, 13153–13530.

(75) Fisher Scientific, *Tetrathiafulvalene, 99+%, MSDS No. 97477*, One Reagent Lane, Fair Lawn, NJ, 2004.

(76) A. Misra, K. Kozma, C. Streb and M. Nyman, *Angewandte Chemie International Edition*, 2020, **59**, 596–612.

(77) N. N. Greenwood, in *Chemistry of the Elements*, Elsevier, 1997, pp. 789–887.

(78) X. Sun, Y. Qi, J. Li, W. Wang, Q. Ma and J. Liang, *Journal of Organometallic Chemistry*, 2018, **859**, 117–123.

(79) E. Falbo and T. J. Penfold, *The Journal of Physical Chemistry C*, 2020, **124**, 15045–15056.

(80) H. Wang, S. Hamanaka, Y. Nishimoto, S. Irle, T. Yokoyama, H. Yoshikawa and K. Awaga, *Journal of the American Chemical Society*, 2012, **134**, 4918–4924.

(81) K. Oláh, *Periodica Polytechnica Chemical Engineering*, 1960, **4**, 141–156.

(82) V. I. Volkov, A. V. Chernyak, D. V. Golubenko, V. A. Tverskoy, G. A. Lochin, E. S. Odjigaeva and A. B. Yaroslavtsev, *Membranes*, 2020, **10**, 272.

Appendices

Appendix A

Abbreviations and symbols

A	electrode area
D	diffusion coefficient
F	Faraday constant
I_{peak}	peak current
I	current
P	power
R	universal gas constant
S_{Ox}	average oxidation state
T	temperature
U^o	standard reduction potential
U^o_{AB}	standard reduction potential for the reaction $\mathrm{A} + z\,\mathrm{e}^- \longrightarrow \mathrm{B}$
U^o_{BC}	standard reduction potential for the reaction $\mathrm{B} + z\,\mathrm{e}^- \longrightarrow \mathrm{C}$
U	reduction potential
η	activation overpotential
$\mathbf{Q}$	charge
a_{Ox}	activity of the oxidised species

a_{Red}	activity of the reduced species
c_{Ox}	concentration of the oxidised species
c_{Red}	concentration of the reduced species
c	concentration of active species
f	$\frac{nF}{RT}$
j_0	exchange current density
j	current density
k_0	standard rate constant
n	number of electrons exchanged
v	scan speed
AQ	anthraquinone
AQ-tris	booster based on anthraquinone and a linker of trifold symmetry
BE	bulk electrolysis
CB	carbon black
CCCP	constant current/constant potential
CE	counter electrode
CF	carbon felt
CV	cyclic voltammogram
DBF	1,1-dibromoferrocene
GC	glassy carbon
HER	hydrogen evolution reaction
ITO	indium tin oxide
LIB	lithium-ion battery
MSE	mercury/mercurous sulfate electrode
NDI	naphthalenetetracarboxylic diimide
OCP	open circuit potential
OCV	open circuit voltage
OER	oxygen evolution reaction
PANI	polyaniline
PCET	proton-coupled electron transfer

PMo_{12}	$[PMo_{12}O_{40}]^{3-}$
POM	polyoxometalate
PTFE	polytetrafluoroethylene
PV_{14}	$[PV_{14}O_{42}]^{9-}$
RE	reference electrode
RFB	redox flow battery
SiW_{12}	$[SiW_{12}O_{40}]^{4-}$
TAT	5,10,15-Tris[2-(hydroxy)ethyl]-10,15-dihydro-5,10,15-triaza-5H-tribenzo[a,f,k]triindene
TEMPO	(2,2,6,6-Tetramethylpiperidin-1-yl)oxyl
tris-Br	bromide salt of a 1,3,5-tris(1-pyridyl)benzene-based booster material
TTF	tetrathiafulvalene
VRFB	all-vanadium redox-flow battery
WE	working electrode

Appendix B

Publication: A polyoxometalate redox flow battery: functionality and upscale

Clean Energy, 2019, Vol. 3, No. 4, 278–287

doi: 10.1093/ce/zkz019
Advance Access Publication Date: 15 August 2019
Homepage: https://academic.oup.com/ce

RESEARCH ARTICLE

A polyoxometalate redox flow battery: functionality and upscale

Jochen Friedl[1,2], Felix L. Pfanschilling[1], Matthäa V. Holland-Cunz[1], Robert Fleck[3], Barbara Schricker[3], Holger Wolfschmidt[3] and Ulrich Stimming[1,*]

[1]Chemistry—School of Natural and Environmental Sciences, Bedson Building, Newcastle University, Newcastle upon Tyne, NE1 7RU, UK
[2]Present address: BMW AG, Petuelring 130, 80788 Munich, Germany
[3]Corporate Technology, Siemens AG, 91058 Erlangen, Germany

*Corresponding author. E-mail: ulrich.stimming@ncl.ac.uk

Abstract

While redox flow batteries carry a large potential for electricity storage, specifically for regenerative energies, the current technology-prone system—the all-vanadium redox flow battery—exhibits two major disadvantages: low energy and low power densities. Polyoxometalates have the potential to mitigate both effects. In this publication, the operation of a polyoxometalate redox flow battery was demonstrated for the polyoxoanions $[SiW_{12}O_{40}]^{4-}$ (**SiW_{12}**) in the anolyte and $[PV_{14}O_{42}]^{9-}$ (**PV_{14}**) in the catholyte. Emphasis was laid on comparing to which extent an upscale from 25 to 1400 cm^2 membrane area may impede efficiency and operational parameters. Results demonstrated that the operation of the large cell for close to 3 months did not diminish operation and the stability of polyoxometalates was unaltered.

Keywords: energy storage; redox flow battery; polyoxometalates; upscale

Introduction

Redox flow batteries (RFBs) are one of the few options to store energy from intermittent renewable-energy sources such as wind and solar electrochemically. The concept of the RFB has several advantages [1–3], such as the independent scalability of power and energy content. The former is determined by the size of the power converter, whereas the latter is given by the energy density of the electrolyte and the size of the tanks. Furthermore, as opposed to other battery types, the electrodes themselves are not redox-active and do not undergo conversion, intercalation or alloying reactions, which often lead to degradation. Instead, the energy is stored in redox-active species that are dissolved in the electrolyte.

Current challenges for RFB chemistry are their power density, their energy density and their costs [1–4]. According to Arenas et al., the development of new RFB technology can be described as follows [5]. As a first step, the fundamental electrochemistry is explored. Physical and chemical properties as well as important parameters, such as the equilibrium potential U_0 and the electron-transfer constant k_0 of the involved species, are investigated (Stage 1a). Following this, the cycling behaviour and stability of the novel RFB electrolytes are assessed in H-cells or laboratory-scale flow cells (Stage 1b). The next step then involves optimization of the electrochemical power converter according to the chemical and physical properties of the RFB electrochemistry. Potential and

Received: 15 January, 2019; **Accepted:** 19 June, 2019

current distribution, hydrodynamics, mass transport and cell geometry are optimized (Stage 2a), followed by the development of a pilot stack and a prototype RFB system (Stage 2b). The final stage according to Arenas et al. is a commercial implementation, which involves fabrication, testing, maintenance, marketing and many other tasks outside the realm of electrochemical engineering (Stage 3).

The properties of the used redox shuttles and employed solvents determine how the electron transfer and mass transport proceed within the power converter. Therefore, ideally, the power converter should be optimized for the specific redox shuttle. However, while many novel redox electrochemistries were proposed for RFBs in recent years, the literature focuses mostly on Stages 1a and 1b [6]. A recent literature review by our group showed that, of 24 published redox electrochemistries for RFBs, only 4 were demonstrated with a power rating of more than 100 W [3]. These are the all-vanadium RFB (VRFB) [7, 8], the zinc-bromine cell [9, 10], the iron-chromium cell [11, 12] and the bromine-polysulphide RFB [1, 13, 14]. Of the remaining 20, 7 were tested in H-cell configurations only, all the others except for 2 in cells with less than 1-W power output. So, there is currently a knowledge gap between the laboratory Stage 1b and the electrochemical technology Stage 2a. This is one of the reasons for showing how a scale-up of a novel electrochemistry from a 25-cm^2 cell to a cell of 1400 cm^2 may affect important performance parameters of the RFB. The approach in our laboratory is to use polyoxometalates as redox shuttles. The redox electrochemistry described here is a polyoxometalate (POM) system, utilizing the polyoxoanions $[SiW_{12}O_{40}]^{4-}$ (**SiW_{12}**) in the anolyte and $[PV_{14}O_{42}]^{9-}$ (**PV_{14}**) in the catholyte as nano-sized charge carriers [15].

Due to their structural and chemical properties, these metal-oxygen clusters have a number of advantages for energy-storage applications [15]. First, due to their large size, the interaction of the redox centres of the POM with solvent molecules is small. Therefore, the outer-sphere reorganization energy of the electron transfer is low, enabling fast kinetics and thus high power densities [16, 17]. Also, the inner-sphere reorganization energy is low due to the added electrons often being delocalized [18], causing only a minimal change in coordination upon reduction or oxidation [19]. This behaviour adds to the fast kinetics and thus high power densities. Their nature as large anions also prevents POMs from penetrating commercial cation-exchange membranes [15]. Size exclusion and electrostatic repulsion prohibit cross-over and mixing of the active species. Furthermore, some POMs exhibit high solubility, e.g. a concentration of 0.875 mol L^{-1} can be obtained for **SiW_{12}** [15]. With multiple redox-active centres per molecule, this enables a high energy density in the battery. Moreover, both **SiW_{12}** and **PV_{14}** are stable during the operation of the battery. Losses in capacity only seem to stem from a parasitic reaction with residual oxygen, which could be avoided with an improved airtight setup [15].

Comparing the asymmetric POM system with the VRFB, one main difference is apparent: the electron transfer for the V^{2+}/V^{3+} and VO^{2+}/VO_2^{+} redox reactions is slow ($k_0 \approx 10^{-6} cm\ s^{-1}$) [7, 20], whereas electron transfer for the POMs is facile ($k_0 \approx 10^{-2}$cm s^{-1}) [15, 21]. The consequence is that the charge-transfer resistance R_{CT} for the POMs is considerably lower than for the VRFB. This leads to consequences for the design of the power converter, as the power-converter design aims to reduce the total resistance R_{tot}, which is the sum of R_{CT}, R_{diff} and the Ohmic losses R_{Ohm}. The resistance of the cell determines the currents I that can be drawn from a battery for a given voltage efficiency η_V :

$$\eta_V = \frac{\Delta U - R_{tot} I}{\Delta U + R_{tot} I}$$

with cell voltage ΔU. In this study, we describe our findings of a novel flow battery electrochemistry for a laboratory-type cell of 25 cm^2 and the scale-up to a commercial cell of 1400 cm^2. Details on the basic electrochemistry of this novel RFB system can be found in a recent publication [15].

In this paper, we are describing the operational parameters such as charge–discharge cycles, coulombic and energy efficiencies, and stability of the electrolytes. Typical values such as R_{Ohm}, R_{CT} and R_{diff} are determined using electrochemical impedance spectroscopy (EIS) and compared for the two cells.

1 Materials

1.1 Cells, sensors and parameters

Three electrode measurements were performed in custom-built glass cells with a polished glassy carbon working electrode (surface area A = 0.02 cm^2), a gold wire (diameter d = 0.5 mm) counter electrode and a mercury/mercurous sulphate reference electrode in 1 M H_2SO_4 (MSE, 0.668 V vs. Standard Hydrogen Electrode [SHE]). Prior to the measurements, the electrolyte was purged with nitrogen and the cell was kept under nitrogen pressure during the experiment. A Bio-Logic SP-300 potentiostat was used for control and data acquisition.

The small flow cell used was a commercial cell (C-Tech 5x5, surface area A = 25 cm^2). Graphite felts (GFD, SGL Carbon) were used as electrodes and pre-treated at 400°C for 24 h in a laboratory atmosphere. In the cell, the 4.6-mm-thick electrodes were compressed to 3.5 mm. As the membrane, a cation-exchange membrane (FUMASEP—F-1075-PK) was used. During the experiment, the cell and the pump with tubing were kept in a polycarbonate box purged with nitrogen. The peristaltic pump could supply flow rates of 12–150 ml min^{-1}. Charge and discharge cycles were measured using a Bio-Logic BCS-810 battery tester. EIS measurements were performed using the Bio-Logic SP-300 (maximum supplied f = 7 MHz, measurement up to 200 kHz), as this could apply higher frequencies than the battery tester (f up to 10 kHz).

The large flow cell used was a commercial cell (J. Schmalz GmbH, surface area A = 1400 cm^2), originally designed for the VRFB chemistry. The same membrane as in the small cell was used. The flow rate was adjusted via the pressure drop in the cell. Measured electrolyte flow and pressure drop were always proportional for both anolyte and catholyte. Flow rates from 450 to 1872 ml min^{-1} were determined. Both the charge–discharge cycles and EIS were measured using a Bio-Logic BCS-815. *In operando* measurements of the *pH* values in the tanks were performed using Unitrode pH sensors from Metrohm. For data acquisition of the pH values, a National Instruments cDAQ-9175 was used in combination with a National Instruments Module 9205 and a current loop converter CLC-01 from company providing electronic measurement. Fig. 1 shows a photograph of a 1400-cm^2 cell with its periphery and containment. The cell itself is fixed in the top part of an acrylic glass container, the pumps are installed underneath and the electrolyte tanks are to the left and right of the pumps. The electrolyte tanks are continuously purged with nitrogen to avoid oxidation of the reduced redox species by atmospheric oxygen.

Tables 1 and 2 give an overview of the parameters used in this work. These quantities are used to discuss and compare the performance of the two cells.

1.2 Electrolytes and their electrochemistry

The electrochemistry and preparation of **SiW**$_{12}$ and **PV**$_{14}$ were described in detail in ref. [15]. In short, **SiW**$_{12}$ was bought from Sigma-Aldrich as tungstosilic acid ($H_4SiW_{12}O_{40}$) and dissolved in de-ionised (DI) water with 1 M LiCl. Diluted LiOH was used for pH adjustment to 1.8 to prepare the anolyte. **PV**$_{14}$ was prepared following the synthesis for $Na_5[H_4PV_{14}O_{42}]\cdot 28\ H_2O$ described in ref. [22]. To prepare the catholyte, $Na_5[H_4PV_{14}O_{42}]\cdot 28\ H_2O$ was dissolved in DI water with 1 M LiCl and pre-reduced by addition of hydrazine (Sigma-Aldrich). This reduction was necessary, as otherwise both anolyte and catholyte would have been fully oxidized at the start of the battery operation, making cycling impossible. Cyclic voltammograms (CVs) of 1 mM **PV**$_{14}$ (red line) and 1 mM **SiW**$_{12}$ (blue line) are shown in Fig. 2a. **PV**$_{14}$ exhibits a multi-electron redox reaction in the range from 0.2 to 0.7 V vs. SHE. Experiments in a symmetric flow battery (**PV**$_{14}$ as both anolyte and catholyte) have shown that **PV**$_{14}$ transfers at least seven electrons [15]. **SiW**$_{12}$ shows two redox reactions at $U^{\theta,1}_{SiW_{12}} = 0.0$ V vs. SHE and $U^{\theta,2}_{SiW_{12}} = -0.21$ V vs. SHE. A third redox wave centred on $U^{\theta,3}_{SiW_{12}} = -0.37$ V vs. SHE is a two-electron redox reaction as opposed to the previous two, which are one-electron transfers. However, the third reaction is not used in the flow battery because the potential at which it takes place leads to an irreversible dimerization of the POM onto the carbon electrodes [23]. The polyhedral structures shown in Fig. 2b and Fig. 2c reveal that both **SiW**$_{12}$ and **PV**$_{14}$ are of the Keggin structure, with two additional V–O caps for the polyoxovanadate [24].

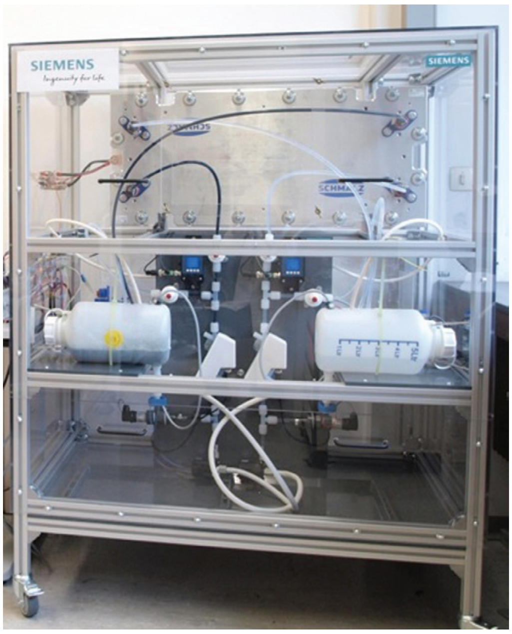

Fig. 1 Photograph of 1400-cm^2 cell with periphery (tanks, pumps, tubing) and containment

2 Results in a 25-cm² cell

In order to obtain data from a polyoxometalate redox flow battery, a commercial cell from C-Tech with a membrane area of 25 cm^2 was used. Heat-treated, compressed graphite felts (Sigracell GFD 4.6 EA) were used as electrodes as described earlier and a FUMASEP—F-1075-PK membrane was employed. The electrolytes comprised 80 mM **SiW**$_{12}$ for the anolyte and 80 mM **PV**$_{14}$ for the catholyte in 1 M LiCl each. In charge–discharge cycles, the 25-cm^2 cell exhibited a coulombic efficiency $\eta_C^{25cm^2}$ of 96% and an energy efficiency $\eta_E^{25cm^2}$ of 64%. The theoretic capacity was $Q_{dch}^{theo,25cm^2} = 214$ mAh, of which 90% was reached. A study of the influence of the electrolyte concentration on the diffusion resistance R_{diff} was conducted.

In Fig. 3, R_{diff} is compared for the 25-cm^2 cell with 80 mM **SiW**$_{12}$ and 80 mM **PV**$_{14}$ as electrolytes (blue data) and a setup in which the anolyte was 600 mM **SiW**$_{12}$ and the catholyte 300 mM **PV**$_{14}$ (red data). To balance the charge, the **PV**$_{14}$ was pre-reduced by four electrons with hydrazine (instead of a pre-reduction by two electrons as for equal concentrations of POMs). The volume flow $\dot{v}$ has been recalculated to normalized mass flow $\dot{c}$ (see Table 2) by multiplying $\dot{v}$ with the used concentrations of catholyte. It can clearly be seen that the mass flow, that is the amount of unreacted active material that is brought into the cell per minute, determines R_{diff}.

3 Results in a 1400-cm² cell

3.1 Charge and discharge

An electrolyte solution with 80 mM **SiW**$_{12}$ was prepared as anolyte; a solution of 80 mM **PV**$_{14}$ was used as catholyte.

Table 1 Experimental parameters obtained or set in the measurements

Experimental parameters	Symbol	Obtained from
Surface area of cell	A (cm^2)	Geometric area cell/membrane
Charge time	t_{ch} (s)	Charge–discharge experiment. Time until defined cut-off voltage reached
Discharge time	t_{dch} (s)	
Upper voltage limit	U^{up} (V)	Set voltage limits (cut-off voltages)
Lower voltage limit	U^{low}(V)	
Charge current density	I_{ch} ($mA\ cm^{-2}$)	Set in galvanostatic charge–discharge experiment
Discharge current density	I_{dch} ($mA\ cm^{-2}$)	
Cell voltage	$\Delta U(t)$ (V)	Measured in galvanostatic charge–discharge experiment
Anolyte pH value	pH_{an}	Measured in electrolyte tanks by pH sensors
Catholyte pH value	pH_{cat}	
Volumetric flow rate	$\dot{V}$ ($ml\ min^{-1}$)	Set by pump control
Pressure drop	Δp (mbar)	Measured by pumps in 1400-cm^2 cell
Ohmic resistance	R_{Ohm} ($\Omega\ cm^2$)	Fit of impedance spectrum
Charge-transfer resistance	R_{CT} ($\Omega\ cm^2$)	Fit of impedance spectrum
Diffusion resistance	R_{diff} ($\Omega\ cm^2$)	Fit of impedance spectrum
Anolyte volume	V_{an} (L)	Electrolyte preparation
Catholyte volume	V_{cat} (L)	
Anolyte concentration	c_{an} ($mol\ L^{-1}$)	Electrolyte preparation
Catholyte concentration	c_{cat} ($mol\ L^{-1}$)	
Transferred electrons of anolyte species	n_{an}	Defined by properties of molecule, $n_{an} = 2$
Transferred electrons of catholyte species	n_{cat}	Determined by pre-reduction with hydrazine

Table 2 Derived parameters: F (Faraday constant) = 96 485 $\frac{As}{mol}$

Derived parameters	Definition
Theoretical capacity anolyte (mAh)	$Q_{an}^{theo} = n_{an} \cdot c_{an} \cdot V_{an} \cdot F$
Theoretical capacity catholyte (mAh)	$Q_{cat}^{theo} = n_{cat} \cdot c_{cat} \cdot V_{cat} \cdot F$
Discharge capacity (mAh)	$Q_{dch} = I_{dch} \int_0^{t_{dch}} dt$
Charge capacity (mAh)	$Q_{ch} = I_{ch} \int_0^{t_{ch}} dt$
Coulombic efficiency (%)	$\eta_C = \frac{Q_{dch}}{Q_{ch}} \cdot 100$
Voltage efficiency (%)	$\eta_V = \frac{\int_0^{t_{dch}} U(t)dt}{\int_0^{t_{ch}} U(t)dt} \cdot 100$
Energy efficiency (%)	$\eta_E = \frac{I_{dch} \int_0^{t_{dch}} U(t)dt}{I_{ch} \int_0^{t_{ch}} U(t)dt} \cdot 100$
Normalized volume flow ($ml\ min^{-1}\ cm^{-2}$)	$\dot{\upsilon} = \frac{\dot{V}}{A}$
Normalized mass flow ($mol\ min^{-1}\ cm^{-2}$)	$\dot{c} = \dot{\upsilon} \cdot c_{cat}$

With $n_{an} = n_{cat} = 2$ L and $V_{an} = V_{cat} = 1.5$ L, the theoretical capacity for both electrolytes was $Q_{an}^{theo} = Q_{cat}^{theo} = 6.4$ Ah. Fig. 4a shows cycle 10 as an example for the cycling behaviour of the 1400-cm^2 cell. At a current density of 4 mA cm^{-2}, the cell reaches its upper voltage cut-off $U^{up} = 1.4$ V after ~3000 s; the successive discharge takes another 3000 s and stops at $U^{low} = 0$ V. During cycle 10, the coulombic efficiency was $\eta_C^{10} = 99.13$ % and the energy efficiency was measured to be $\eta_E^{10} = 86.13\%$. The pH probes reveal that the concentration of hydronium ions in the anolyte (green line) does not change significantly during one cycle, but that the *pH* in the catholyte drops during charge and increases during discharge. The explanation for this is the proton-coupled electron transfer (PCET) of **PV$_{14}$** [15] in combination with a change in pK_a [22]. During the charge of the battery, **PV$_{14}$** is oxidized, which releases two electrons and two protons:

$$\left[H_6PV_{12}^{V}V_{10}^{IV}O_{42}\right]^{5-} \rightarrow \left[H_4PV_{14}^{V}O_{42}\right]^{5-} + 2e^- + 2H^+ \qquad (1)$$

During discharge, the reverse process of Equation 1 takes place: **PV$_{14}$** takes up protons from the catholyte and the pH increases. This effect is restricted to the catholyte because the majority of the cations that cross the cation-exchange membrane are Li^+ ions. Fig. 4b compares the previously shown 10th cycle to the 1000th cycle. The latter was recorded 1508 h or 63 days after the former. As can be seen in the graph, the general shape of the charge and discharge curves is not changed, exhibiting similarly high efficiencies $\eta_C^{1000} = 99.2\%$ and $\eta_E^{1000} = 85.1\%$. The theoretical capacity $Q_{an}^{theo} = Q_{cat}^{theo} = 6.4$ Ah was not reached during cycling. In the 10th cycle, a discharge capacity of 4.6 Ah was measured, which corresponds to 72% of the theoretical capacity. Two plateaus can easily be distinguished and can be assigned to the first and second one-electron waves of **SiW$_{12}$**. The oxidation state of **PV$_{14}$** does not influence the potential that much because of its multiple electron waves occurring at similar potentials. However, the plateau at higher voltages is shorter than the one at low voltages, which can be explained by an insufficient pre-reduction of **PV$_{14}$** with hydrazine or oxidation by residual oxygen, respectively. Since the unit was not suited for applying a vacuum, it was impossible to completely empty the whole container of oxygen, so oxidation by air probably happened to a certain degree.

The long-term cycling behaviour of the 1400-cm^2 cell is shown in Fig. 5. The changes in pH of the anolyte and catholyte are given in Fig. 5a. The behaviour over 1400 cycles is in line with the pH changes shown in Fig. 4a for

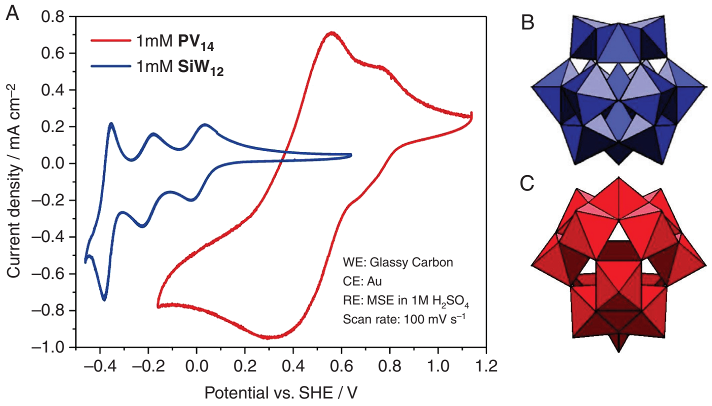

Fig. 2 Cyclic voltammograms (CVs) and structure of the used POMs. (a) CVs of 1 mM **SiW**$_{12}$ and 1 mM **PV**$_{14}$ at a scan rate of 100 mV s^{-1}. (b) Polyhedral representation of **SiW**$_{12}$. (c) Polyhedral representation of **PV**$_{14}$.

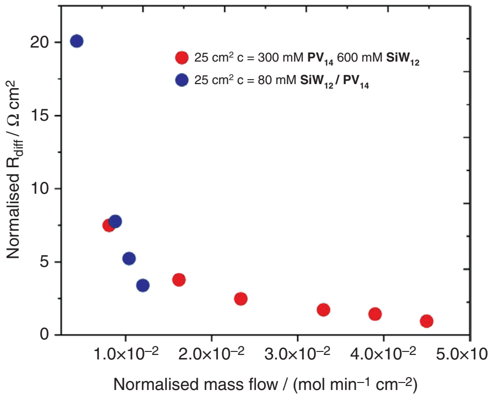

Fig. 3 Mass-transport resistance R_{diff} over normalized mass flow for two different concentrations of electrolyte measured in the 25-cm^2 cell

cycle 10; the hydronium concentration in the catholyte (green area) changes much more than that of the anolyte (blue area). The pH of the catholyte is stable; the pH of the anolyte increases slightly from 1.5 to 2 during 1400 cycles (pH data were not continuously recorded). Fig. 5b shows the capacity retention (red data) and the current density (blue line) of the 1400-cm^2 cell during 1400 cycles. The discharge capacity dropped from Q^1_{dch} = 4.70 Ah to Q^{1400}_{dch} = 3.95 Ah, which equals an average capacity loss of 0.53 10^{-3} Ah/cycle or 0.011% per cycle. The capacity loss of 0.75 Ah may be due to slow ingress of atmospheric oxygen, taking up protons while being reduced to water. This is supported by similar numbers of charges involved: 0.75 Ah is equal to 28 mmol of transferred electrons while the pH shift from 1.5 to 2 mentioned earlier corresponds to 32 mmol of used-up protons. When the current density was increased from 4 to 43 mA cm^{-2} (cycles 185 to 240), the discharge capacity dropped to $Q_{dch} \approx 3.2$ Ah. Comparing Fig. 5a and Fig. 5b, one can notice that the pH of the anolyte decreases from approximately 1.5 to 1.0 when the current density is increased from 4 to 43 mA cm^{-2}. This observation can currently not be explained. Fig. 5c shows the coulombic efficiency η_C (black data) and energy efficiency η_E (red data). For the 1400 cycles measured, η_C is at approximately 99%. During the cycles with higher current density (cycles 185 to 240), η_C increases to 100%. The coulombic efficiency η_C of the **PV**$_{14}$–**SiW**$_{12}$ system in the 1400-cm^2 cell is higher than it is for typical VRFB cells ($\eta_C^{VRFB} \approx 0.9$ [1, 25, 26]). While the VRFB loses charge through cross-mixing of the electrolytes and by the parasitic hydrogen evolution reaction (HER) [27], the POM system experiences no cross-over and the HER has not been observed due to more positive potentials in the anolyte compartment. An energy efficiency $\eta_E \approx 86$ % during the cycles at 4 mA cm^{-2} and only $\eta_E \approx 40$ % during the cycles at 43 mA cm^{-2} was achieved. An EIS study was conducted to determine which resistance, R_{Ohm}, R_{CT} or R_{diff}, contributes most to the overvoltage and therefore the decrease in η_E at higher rates.

3.2 EIS

Impedance spectra were recorded at different volumetric flow rates $\dot{V}$ in the 1400-cm^2 cell; Nyquist plots of these spectra are shown in Fig. 6a. The volumetric flow rates $\dot{V}$ (ml min^{-1}) were normalized to volumetric flow rates per surface area of the cell $\dot{v}$ (ml min^{-1} cm^{-2}). To obtain R_{Ohm}, R_{CT} and R_{diff}, semicircles were fitted to the spectra. The intercepts of these semicircles with the abscissa determine the resistances. The first intercept at the highest frequencies is R_{Ohm}, then R_{CT} followed by R_{diff}. As can be seen in Fig. 6a, especially in the inset Fig. 6b, the first semicircle (at high frequencies) is relatively independent of the normalized flow

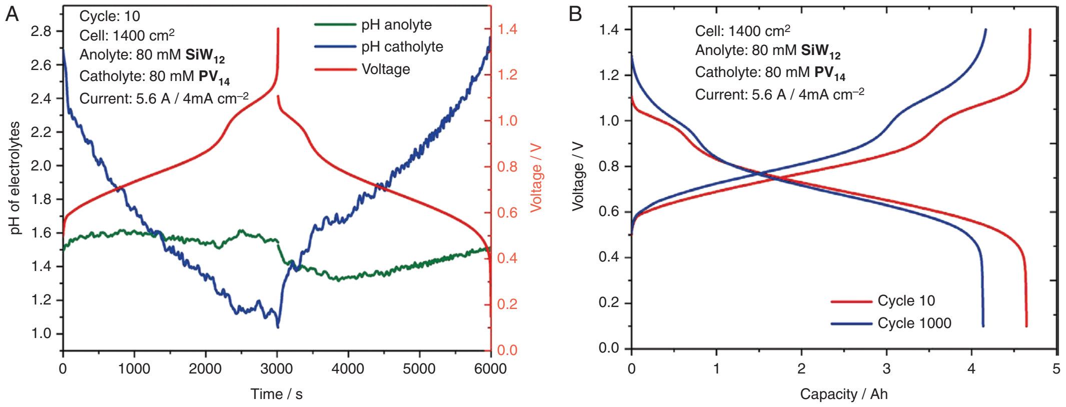

Fig. 4 Cycling behaviour of the 1400-cm² cell. (a) Recorded observables of the 10th charge–discharge cycle over time. Measured pH values of anolyte (green line) and catholyte (blue line) are shown, as well as the cell voltage (red line). (b) Direct comparison of cycle 10 and cycle 1000. Cycle 1000 was recorded 63 days after the 10th cycle.

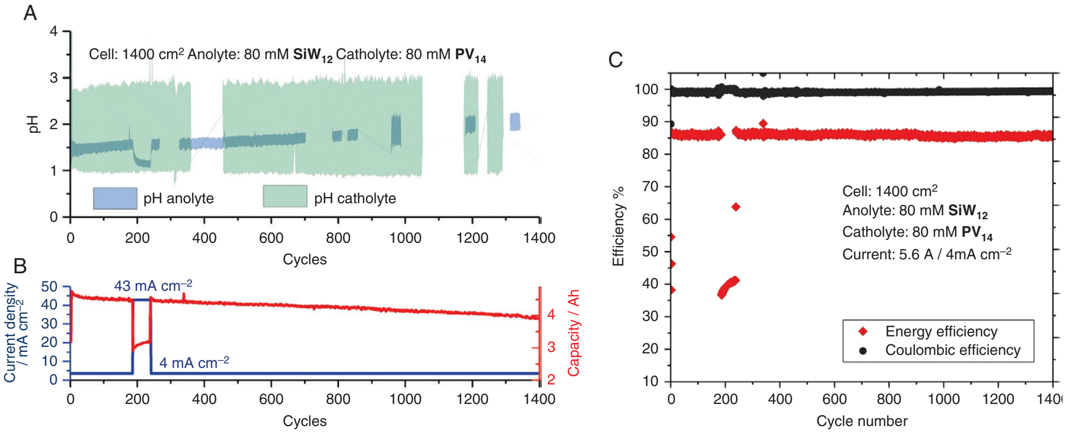

Fig. 5 Long-term behaviour of the 1400-cm² cell. (a) pH of anolyte and catholyte over cycle number. (b) Capacity retention and current density. (c) Coulombic and energy efficiency.

rate. The second semicircle (at lower frequencies) becomes smaller with higher normalized flow rates. Determined values for R_{Ohm} (red segment), R_{CT} (blue segment) and R_{diff} (green segment) are shown in Fig. 6c. The Ohmic resistance R_{Ohm} represents Ohmic losses in the leads, the current collector, the contact resistance between the current collectors and the electrodes, the resistance of the solution and the ionic resistance in the membrane [28]. R_{Ohm} is independent of flow rate and with R_{Ohm} = (2.806 ± 0.021) Ω cm² higher than typical values for the VRFB system, $R_{\mathrm{Ohm}}^{\mathrm{VRFB}} \approx 0.5\ \Omega\ \mathrm{cm}^2$ [29]. We assume that this high resistance stems mostly from the ionic resistance of the membrane. Due to a lack of protons ($pH > 1$), Li⁺ cations are used to enable charge balance by their transport through the membrane and the diffusion coefficient for Li⁺ through a perfluorosulphonated polymer membrane is smaller than that of H⁺ [30]. The charge-transfer resistance R_{CT} is also independent of the flow rate and, at R_{CT} = (0.382 ± 0.015) Ω cm², smaller than R_{Ohm}. The explanation for this small value of R_{CT} is that it is inversely proportional to the electron-transfer constant k_0 and k_0 is large for the POMs [15, 31]. The resistance invoked by mass-transport limitations depends on $\dot{v}$ because the flow rate governs at which rate fresh electrolyte is transported to the electrodes, which can then undergo electron transfer. Even at the highest flow rate ($\dot{v}$ = 1.34 ml cm^{-2} min^{-1}), $R_{diff} = 4.4\ \Omega\ \mathrm{cm}^{-2}$ and therefore diffusion presents a larger resistance than R_{Ohm} and R_{CT} combined. At lower flow rates, this problem is aggravated. There are two ways to bring more unreacted electrolyte to the electrode in a given time:

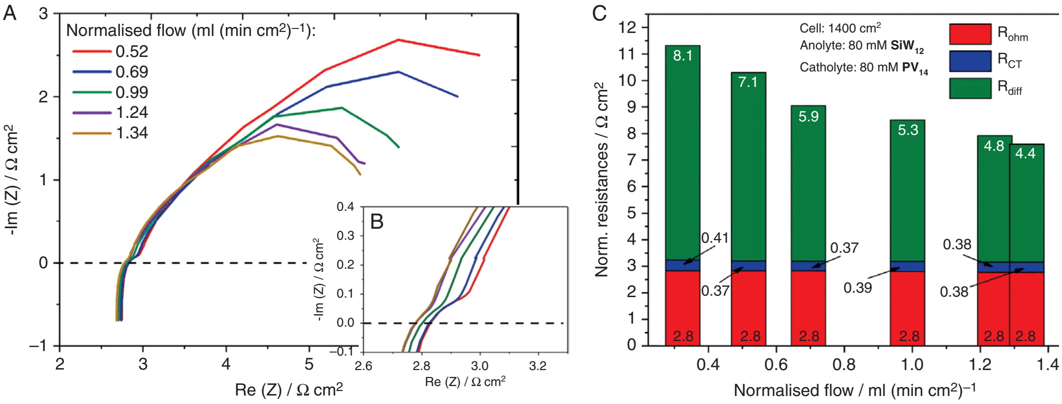

Fig. 6 Galvanostatic impedance data for the 1400-cm² cell. (a) Nyquist plots for various normalized pump rates. (b) Detail of (a) showing the first semicircle. (c) Extracted resistances (R_{ohm}, R_{CT}, R_{diff}) over the normalized flow. Measurements were made with no current bias at 36% SOC, which corresponds to the centre of the first one-electron redox wave of SiW_{12}.

(i) Increase the concentration of the redox species to increase the amount of reactant per pumped volume. This approach can be done without changing the power converter and has been shown earlier in this work using the 25-cm² cell (see Fig. 3).

(ii) Increase the pump rate and thereby the flow of electrolyte. In order to increase the pump rate, the cell would have to be modified because, at the moment, the pressure drop within the cell is already at 900 mbar at 1.34 ml cm⁻² min⁻¹, and the cell could most likely not withstand higher pressure drops. Therefore, the cell would have to be converted to a design with a lower impedance to flow, such as a flow-by design instead of a flow-through configuration [5, 32].

3.3 Post-cycling analysis of electrolytes

After 1400 cycles, the electrolytes used were extracted from the battery and investigated by ^{51}V NMR and CV studies, the results of which are shown in the supporting information. Supplementary Fig. 1a (see the online supplementary data) gives the ^{51}V NMR spectra of the anolyte and the catholyte. The signal of the catholyte (red curve) shows the typical fingerprint signal of $\mathbf{PV_{14}}$ [15, 22]. Two small additional peaks at a chemical shift of –505 p.p.m. and –525 p.p.m. can be attributed to $[V_{10}O_{28}]^{6-}$, a polyoxovanadate that forms from $\mathbf{PV_{14}}$ at pH >2.3 but is in a pH-dependent dynamic equilibrium with $\mathbf{PV_{14}}$ [22]. We investigated the formation of $[V_{10}O_{28}]^{6-}$ and the time and pH dependency of this process earlier via ^{51}V NMR and found that a pH value as low as 1.7 can be tolerated permanently and even lower values are acceptable for short periods of time [15]. All observed conversions are reversible and do not cause permanent capacity loss. This indicates that $\mathbf{PV_{14}}$ in the catholyte was stable during the cycling and did not decompose to single vanadium species. The anolyte (blue curve) shows no vanadium signal, indicating that no $\mathbf{PV_{14}}$ has crossed over into the anolyte reservoir during the 1400 cycles. This result is in line with our earlier results that showed that the negatively charged POMs do not cross cation-exchange membranes [15]. CVs of both electrolytes were recorded to check the state of health of the anolyte and to confirm the result of the ^{51}V NMR for the catholyte. Supplementary Fig. 1b (see the online supplementary data) shows the CV of the anolyte after 1400 cycles, which matches the typical CV of $\mathbf{SiW_{12}}$ (compare Fig. 2a). Similarly, the CV of the anolyte shown in Supplementary Fig. 1c (see the online supplementary data) matches the CV of $\mathbf{PV_{14}}$ (compare Fig. 2a). In conclusion, the post-cycling analysis showed that the POMs in the electrolyte were stable for 1400 cycles equalling 88 days of cycling.

4 Comparison of the two cells

In order to compare the cycling performance of the two cells under investigation, both the flow rate and the capacity are normalized, as shown in Fig. 7a. The 25-cm² cell reached a discharge capacity of $Q_{dch}^{25cm^2}$ = 192 mAh, which is 90% of its theoretical capacity of $Q_{dch}^{theo,25cm^2}$ = 214 mAh. For the 1400-cm² cell, the 10th cycle that was described in Fig. 4b is given for comparison. At a similar flow rate and the same current density (4 mA cm⁻²), the coulombic efficiency of the larger cell is higher: $\eta_C^{1400cm^2}$100% versus $\eta_C^{25cm^2}$ = 96%. It is assumed that the superior atmospheric containment of the 1400-cm² cell keeps more oxygen from entering the tanks and therefore oxidation of reduced $\mathbf{PV_{14}}$ electrolyte is prevented. The difference in energy efficiency is larger, however, for the big cell: $\eta_E^{1400cm^2}$ = 86% as compared to $\eta_E^{25cm^2}$ = 64%. Therefore, the voltage efficiency η_V of the 1400-cm² cell must be higher than that of the 25-cm² cell (as $\eta_E = \eta_V \cdot \eta_C$). While the coulombic efficiency is mainly given by the redox electrochemistry

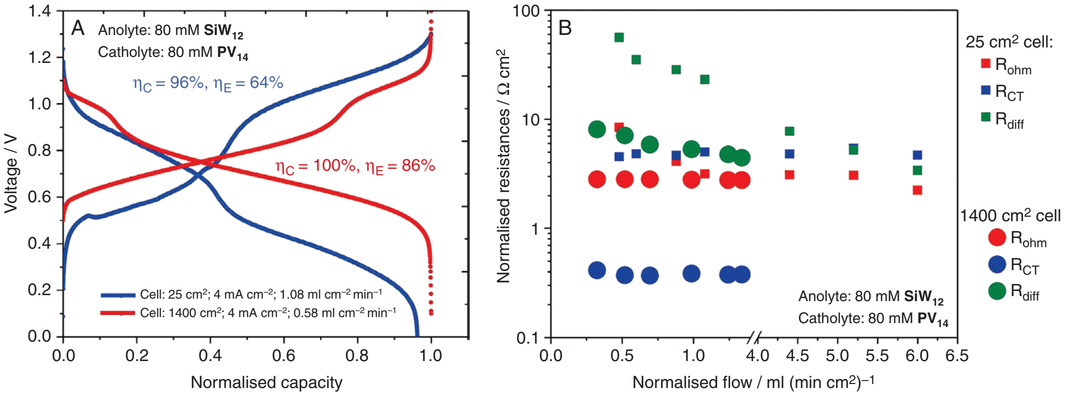

Fig. 7 Comparison of a 25-cm² cell and a 1400-cm² cell with the same electrolyte. (a) A single charge–discharge cycle for the 1400-cm² cell and the 25-cm² cell with energy efficiency η_E and coulombic efficiency η_C given. The capacity is normalized to 1. (b) Resistances R_{Ohm}, R_{CT} and R_{diff} for the 1400-cm² cell (larger circles) and the 25-cm² cell (smaller squares) over the flow rate (normalized to membrane area).

and the electrode materials, cell construction and its materials determine the voltage efficiency. To identify the loss mechanism(s) that contribute to the difference in voltage efficiency, we compare R_{Ohm}, R_{CT} and R_{diff} for both cells versus the normalized flow rate. Data points for the 1400-cm² cell in Fig. 7b are the same as shown in Fig. 6b, but here the resistances for the smaller cell are shown in addition. For both cells, R_{Ohm} and R_{CT} are independent of the flow rate, whereas R_{diff} decreases with higher flow. R_{Ohm} (red data) is very similar for both cells, which is understandable, as this resistance should be determined mostly by the membrane resistance and the same membrane is used in both cells. On average, the charge-transfer resistance is more than 12 times higher in the smaller cell, with $R_{CT}^{25cm^2} = 4.75\ \Omega\ \text{cm}^2$ versus $R_{CT}^{1400cm^2} = 0.382\ \Omega\ \text{cm}^2$, and therefore the charge transfer must be considerably faster in the 1400-cm² cell than in the 25-cm² cell. The difference in R_{CT} values between the two cells cannot be due to the redox electrochemistry, which is identical, and stems most likely from the used electrodes or their pre-treatment. The electrodes of the 25-cm² cell, graphite felts (GFD, SGL Carbon), were heated to 400°C for 24 h in laboratory atmosphere. The electrodes in the 1400-cm² cell were preconditioned in oxygen plasma. The exact parameters of this process are unknown. When heat-treating the GFD 4.6 EA carbon felts for 3 h at various temperatures in air, it was found that R_{CT} reaches a minimum at around 600°C treatment temperature (Pfanschilling, **unpublished** work [33]). Whether this is a long-term effect is yet to be investigated.

Also R_{diff} (green data) is significantly larger in the 25-cm² cell than it is in the 1400-cm² cell, varying with the flow rate we determined factors from 4 to 7. The reason for this difference is unknown but we assume that the flow distribution in the larger cell is more effective than the one in the small cell.

The conclusion from the comparison of the 1400-cm² cell and the 25-cm² cell using the same electrolytes is that the bigger cell performed better. This is indicated by the higher energy efficiency during cycling, and confirmed by the lower resistances found in EIS studies. While R_{Ohm} was similar in both cells, both R_{CT} and R_{diff} were considerably smaller in the 1400-cm² cell. This suggests that the commercial cell, even though it was designed to be used as a VRFB, can yield a higher efficiency than the laboratory cell. The most crucial parameter to improve is R_{diff} (compare Fig. 6c). Looking at the equations for diffusion overvoltage given by Vetter, an increase in the concentration of active species should alleviate this problem [34]. As shown in Fig. 3, R_{diff} indeed depends heavily on mass flow. At high concentrations and for the highest measured rate $R_{diff} = 0.91\ \Omega$ cm². This demonstrates that increasing the concentration of electrolyte is a possible approach to reduce R_{diff}.

5 Summary and conclusion

In this study, we have shown that a recently developed POM electrochemistry for flow batteries can work effectively in a redox flow battery. Data obtained for a 25-cm² laboratory cell were quite satisfying, with a coulombic efficiency of 96%. The energy efficiency of 64% was considerably lower, probably due to specifications in the cell design. It was also demonstrated that a large single cell of 1400 cm² can be successfully employed. While the cell was designed for the VRFB chemistry, it still shows good performance for the investigated **SiW**$_{12}$–**PV**$_{14}$ electrolytes. During 88 days, the 1400-cm² cell was charged and discharged 1400 times. The initial discharge capacity of $Q_{dch}^{1} = 4.70$ Ah dropped to $Q_{dch}^{1400} = 3.95$ Ah, which equals an average capacity loss of 0.53 10^{-3} Ah/cycle. During the cycling at 4 mA cm⁻², a coulombic efficiency of $\eta_C \approx 99\%$ and an energy efficiency of $\eta_E \approx 86\%$ were reached—both values larger than in the small laboratory cell. A post-cycling analysis was performed on the electrolytes. Both ^{51}V NMR and cyclic voltammetry showed that the polyoxoanions in the electrolyte were not damaged during the battery operation and that the molecules had not crossed the membrane. Using pH sensors in the electrolyte tanks, we could show that the pH value of the catholyte changes during cycling, as expected for the PCET experienced by $\mathbf{PV_{14}}$, but that the average pH of the catholyte does not shift over 1400 cycles. The average pH of the anolyte increases slightly during the experiment, from pH 1.5 to 2 during 1400 cycles.

While the cell showed a high energy efficiency at low current densities, this value dropped to $\eta_E \approx 40\ \%$ at 43 mA cm^{-2}. Using impedance spectroscopy, we found that both the Ohmic resistance R_{Ohm} and the charge-transfer resistance R_{CT} were independent of the electrolyte flow rate, but that high flow rates decreased the mass-transport resistance R_{diff}. At the highest volumetric flow rate (1.34 ml cm^{-2} min^{-1}), the measured resistances were as follows: R_{Ohm} = 2.78, R_{CT} = 0.39 and R_{diff} = 4.4 Ω cm^2 . Comparing the first electron transfer of $\mathbf{SiW_{12}}$ (k_0 = 4.2 10^{-2} cm s^{-1}) and the VO^{2+}/VO_2^+ redox reaction (k_0 = 3 10^{-7} cm s^{-1}), the electron transfer of the POM is more than five orders of magnitude faster than that of the latter [15, 35]. This confirms the assumption from the introduction that, for redox couples with fast electron-transfer kinetics, the total resistance R_{total} depends more on the cell parameters R_{diff} and R_{Ohm} than on the electrochemical parameter R_{CT}. For higher concentrations, this will also remain true, with a larger influence from R_{Ohm}. While the above resistances were recorded at an electrolyte concentration of c_{an} = c_{cat} = 80 mM, we have shown in Fig. 3 that R_{diff} decreases with higher mass flows (mol $min^{-1}cm^{-2}$) and therefore concentrations. Simultaneously, R_{CT} will decrease with higher concentrations, as it is inversely proportional to the concentration of redox species [7]. The Ohmic drop R_{Ohm}, which is governed by the membrane, will remain unchanged by a change in the concentration of active material.

This indicates that, in order to increase the performance of the presented asymmetric POM RFB, the cell, specifically parameters related to R_{Ohm} and R_{diff} need to be the main focus for improvements. Components to work on are:

- *Membrane/separator:* The Ohmic drop R_{Ohm}, which is dominated by the membrane resistance, is likely to be the highest resistance in a cell, with a higher concentration of active material, as R_{Ohm} does not scale with the concentration of the redox electrolyte. To reduce R_{Ohm} incurred from the membrane, two measures can be taken:
    - ○ Use a membrane thinner than the currently used FUMASEP—F-1075-PK (thickness 75 μm), as the ionic resistance of the membrane increases with thickness of the membrane. For the VRFB, it was found that a sulphonated fluorinated poly(arylene ether) membrane with 45-μm thickness enabled a higher power density than the same type of membrane with 28 or 80-μm thickness [36]. The 45-μm-thick membrane was found to be the optimum due to the combined effects of Ohmic losses and cross-over. We found that $\mathbf{SiW_{12}}$ does not cross perfluorosulfonic acid (PFSA) membranes as thin as 40 μm due to size exclusion and electrostatic repulsion [15]. The minimum membrane thickness that still prevents cross-over should be determined.
    - ○ Reduce the specific Ohmic resistance of the membrane. We assume that the high value for R_{Ohm} stems from the fact that Li^+ cations are used for charge balance instead of protons. The cell chemistry could either be transferred into a more acidic solvent, which allows the use of protons, or the membrane could be optimized for the use of Li^+ cations. A lower pH than currently employed might lead to stability issues for $\mathbf{PV_{14}}$ [22].

- *The geometry of the power converter and its flow design* [5, 37]: Neglecting an effect of R_{Ohm}, there are two limiting cases for the type of rate control in a electrochemical converter: charge-transfer control and mass-transport control [37]. In the former case, the rate of electron transfer limits the current that can be drawn from the cell; a larger overpotential or a larger surface area for the electrode can increase the rate. Under mass-transport control, the supply of active species and its removal after reaction determine the current; a limiting current $I_L \propto \underline{\mathrm{v}} \cdot \mathrm{c}_{cat/an} = \dot{\mathrm{c}}$ can be defined. Assuming that R_{diff} is a measure for $1/I_L$, the connection between I_L and $\dot{\mathrm{c}}$ is empirically shown in Fig. 3. The proportionality depends on the geometry and typically turbulent flow allows higher I_L than laminar flow. As the POMs exhibit fast electron transfer, and judging from Fig. 6c, I_L needs to be increased to enhance the performance of the cell, which can be done in two ways:
    - ○ Increase the concentration $c_{cat/an}$. This approach was tested for the small cell with the result shown in Fig. 3. Clearly, a higher concentration of active species reduces R_{diff} and increases I_L.
    - ○ Increase the rate at which fresh active material is supplied to the electrodes. This can be done by increasing the pump rate or by enhancing the spatial distribution of the mass flow in the cell to maximize electrolyte utilization.

Supplementary data

Supplementary data is available at *Clean Energy* online.

Acknowledgements

This work was supported by a grant from Siemens AG. Additional support comes from the North East Centre of Energy Materials (NECEM) funded by EPSRC (EP/R021503/1) and Newcastle University.

References

[1] Ponce de Leon C, Friasferrer A, Gonzalezgarcia J, et al. Redox flow cells for energy conversion. *J Power Sources* 2006; 160:716–32.

[2] Weber AZ, Mench MM, Meyers JP, et al. Redox flow batteries: a review. *J Appl Electrochem* 2011; 41:1137–64.

[3] Holland-Cunz MV, Cording F, Friedl J, et al. Redox flow batteries—concepts and chemistries for cost-effective energy storage. *Front Energy* 2018; 12:198–224.

[4] Zhang M, Moore M, Watson JS, et al. Capital cost sensitivity analysis of an all-vanadium redox-flow battery. *J Electrochem Soc* 2012; 159:A1183–8.

[5] Arenas LF, Ponce de León C, Walsh FC. Engineering aspects of the design, construction and performance of modular redox flow batteries for energy storage. *J Energy Storage* 2017; 11:119–53.

[6] Noack J, Roznyatovskaya N, Herr T, et al. The chemistry of redox-flow batteries. *Angew Chemie Int Ed* 2015; 54:9776–809.

[7] Friedl J, Stimming U. Determining electron transfer kinetics at porous electrodes. *Electrochim Acta* 2017; 227:235–45.

[8] Zhang H. Development and application of high performance VRB technology. In: *IFBF 2017—International Flow Battery Forum*, Manchester, UK, 2017.

[9] Rabiul Islam FM, Al Mamun K, Amanullah MTO. *Smart Energy Grid Design for Island Countries*. Basel, Switzerland: Springer, 2017.

[10] Lim HS, Lackner AM, Knechtli RC. Zinc-bromine secondary battery. *J Electrochem Soc* 1977; 124:1154–7.

[11] Johnson DA, Reid MA. Chemical and electrochemical behavior of the Cr(lll)/Cr(ll) half-cell in the iron-chromium redox energy system. *J Electrochem Soc* 1985; 132:1058–62.

[12] Nice AW. *NASA Redox System Development Project StatusCleveland, OH: Cleveland, OH*. 1981.

[13] Scamman DP, Reade GW, Roberts EPL. Numerical modelling of a bromide-polysulphide redox flow battery. Part 1: Modelling approach and validation for a pilot-scale system. *J Power Sources* 2009; 189:1220–30.

[14] Morrisey P. Regenesys: a new energy storage technology. *Int J Ambient Energy* 2000; 21:213–20.

[15] Friedl J, Holland-Cunz MV, Cording F, et al. Asymmetric polyoxometalate electrolytes for advanced redox flow batteries. *Energy Environ Sci* 2018; 11:3010–8.

[16] Laborda E, Henstridge MC, Batchelor-McAuley C, et al. Asymmetric Marcus-Hush theory for voltammetry. *Chem Soc Rev* 2013; 42:4894–905.

[17] Chen H-Y, Friedl J, Pan C-J, et al. In situ X-ray absorption near edge structure studies and charge transfer kinetics of $Na_6[V_{10}O_{28}]$ electrodes. *Phys Chem Chem Phys* 2017; 19:3358–65.

[18] Aparicio PA, Poblet JM, López X. Tungsten redox waves in $[XMW_{11}O_{40}]$ n- (X = P, Si, Al and M = W, Mo, V, Nb, Ti) Keggin compounds—effect of localised/delocalised charges. *Eur J Inorg Chem* 2013; 2013:1910–6.

[19] Yang H-H, McCreery RL. Effects of surface monolayers on the electron-transfer kinetics and adsorption of methyl viologen derivatives on glassy carbon electrodes. *AnalChem* 1999; 71:4081–7.

[20] Fink H, Friedl J, Stimming U. Composition of the electrode determines which half-cell's rate constant is higher in a vanadium flow battery. *J Phys Chem C* 2016; 120:15893–901.

[21] Friedl J, Al-Oweini R, Herpich M, et al. Electrochemical studies of tri-manganese substituted Keggin polyoxoanions. *Electrochim Acta* 2014; 141:357–66.

[22] Selling A, Andersson I, Pettersson L, et al. Multicomponent polyanions. 47: The aqueous vanadophosphate system. *Inorg Chem* 1994; 33:3141–50.

[23] Keita B, Nadjo L. New aspects of the electrochemistry of heteropolyacids. *J Electroanal Chem Interfacial Electrochem* 1987; 227:77–98.

[24] Keggin JF. The structure and formula of 12-phosphotungstic acid. *Proc R Soc A Math Phys Eng Sci* 1934; 144:75–100.

[25] Pezeshki AM, Sacci RL, Veith GM, et al. The cell-in-series method: a technique for accelerated electrode degradation in redox flow batteries. *J Electrochem Soc* 2016; 163:A5202–A5210.

[26] Skyllas-Kazacos M, Grossmith F. Efficient vanadium redox flow cell. *J Electrochem Soc* 1987; 134:2950–4.

[27] Schweiss R, Pritzl A, Meiser C. Parasitic hydrogen evolution at different carbon fiber electrodes in vanadium redox flow batteries. *J Electrochem Soc* 2016; 163:A2089–94.

[28] Sun C-N, Delnick FM, Aaron DS, et al. Probing electrode losses in all-vanadium redox flow batteries with impedance spectroscopy. *ECS Electrochem Lett* 2013; 2:A43–5.

[29] Liu QH, Grim GM, Papandrew AB, et al. High performance vanadium redox flow batteries with optimized electrode configuration and membrane selection. *J Electrochem Soc* 2012; 159:A1246–52.

[30] Samec Z, Trojanek A, Langmaier J. Diffusion coefficients of alkali metal cations in Nafion® from ion-exchange measurements. *J Electrochem Soc* 1997; 144:4236.

[31] Friedl J, Bauer CM, Rinaldi A, et al. Electron transfer kinetics of the VO^{2+}/ VO_2^+—reaction on multi-walled carbon nanotubes. *Carbon N Y* 2013; 63:228–39.

[32] Zhou XL, Zhao TS, An L, et al. Critical transport issues for improving the performance of aqueous redox flow batteries. *J Power Sources* 2017; 339:1–12.

[33] Pfanschilling FL. Unpublished results.

[34] Vetter KJ. *Electrochemical Kinetics—Theoretical and Experimental Aspects*, English edn. New York/London: Academic Press Inc., 1967.

[35] Gattrell M, Park J, MacDougall B, et al. Study of the mechanism of the vanadium 4+/5+ redox reaction in acidic solutions. *J Electrochem Soc* 2004; 151:A123.

[36] Chen D, Hickner MA, Agar E, et al. Optimizing membrane thickness for vanadium redox flow batteries. *J Memb Sci* 2013; 437:108–13.

[37] Walsh FC, Pletcher D. Electrochemical engineering and cell design. In: Pletcher D, Tian Z-Q, Williams D (eds). *Developments in Electrochemistry: Science Inspired by Martin Fleischmann*. Hoboken, NJ: John Wiley & Sons, 2014, 95–109.

Appendix C

Cation-pH effect of $[PV_{14}O_{42}]^{9-}$

During a number of experiments, interesting observations were made concerning the concentration of countercations in PV_{14} solutions, particularly lithium ions and protons. For example, in one instance 30.5 mL of a 0.209 M PV14 solution (also containing 2.926 M Li^+) at pH 2.30 was supposed to be diluted to lower the PV_{14} concentration. To keep the pH, the dilution was done with 50 mL of a 1 M LiCl solution that was also at pH 2.30. However, it was found that the combined solution now had a pH of 2.82.

During another experiment, LiCl (13.7 g) was dissolved in a PV_{14} solution (30 mL, ca. 300 mM), causing the pH to decrease from 2.11 to 0.89. In both cases the Li^+ concentration relative to the PV_{14} concentration was altered. Lowering the Li^+ concentration caused the pH to rise, while increasing the Li^+ concentration caused the pH to drop. A measurement error from the pH-meter (Mettler Toledo FiveEasy pH meter F20) was considered. However, the cation error, also known as lithium- or sodium error or as alkaline error, only appears (as the latter name suggests) at elevated pH values starting from pH 9-12, depending on the type of glass membrane used and thus can be ruled out.[81]

In the first example above, the total dissociated protons of the two original solutions calculated from the pH values (both 2.3) amounts to 0.404 mmol H^+. However, the combined solution contained only 0.122 mmol H^+ (disregarding volume contraction effects and assuming a combined volume of 80.5 mL), so it seems that 0.282 mmol H^+ were adsorbed by the PV_{14}, or 0.044 H^+ per

PV_{14}-molecule.

These findings indicate that PV_{14} reversibly releases and takes up protons based on the Li^+ concentration in its medium, i.e. Li^+ and H^+ compete for the undissociated countercation positions on the POM with the respective concentrations of Li^+ and H^+ in the surrounding medium determining the resulting population.

The exact mechanism was not further investigated. Irrespective of the reason, however, this behaviour has implications for the use of Li-PV_{14} as a battery material, especially when employing higher concentrations. Even though protons have a higher mobility than Li^+ in sulfonated membranes,[82] a considerable amount of the charge balance through the membrane during battery operation will be carried out by Li^+, as their number is much greater: Even if the concentration of Li^+ in the electrolyte was only 1 M, at pH 2.3 this means that there are 200 times more Li^+ than protons. Thus, during charge, a number of Li^+ will move through the membrane to the anolyte side, thereby lowering the concentration of Li^+ in the catholyte and vice versa during discharge. However, in parallel to that another effect takes place: PV_{14} binds more countercations at lower oxidation states, i.e. in discharged states.

Pope and Varga have shown that for Keggin-type POMs at sufficiently low pH that the maximum charge for the anion is -6. Beyond that, any further reduction is accompanied by protonation (proton-coupled electron transfer (PCET)), keeping the charge of the anion at the maximum of -6.[60]

Even though PV_{14} is a bicapped-Keggin-type POM, it is reasonable to assume similar behaviour in terms of PCET to the related Keggin-type. For PV_{14}, with its formal anion charge of -9, this means that even in its fully oxidised form there will be undissociated countercations, which is in agreement with the results of Selling *et al.* (see figure 2.3 on page 13).[32]

In previous experiments in our group (see appendix B) it could be shown that the proton uptake of 80 mM PV_{14} even overcompensated for the amount of protons migrating through the membrane, resulting in an increase in pH of the catholyte during discharge, even though protons move through the membrane towards the catholyte during this process.[24, 25] The described behaviour in this case is beneficial, since experiments in our group showed that reducing a

POM shifts its stable pH window towards higher pH values. However, it shows that the type and quantity of the countercations not only influence solubilities in a POM-RFB, but also influence pH changes during charge and discharge and thus have to be balanced with other parameters, like POM concentration(s), initial pH, etc. to ensure stable operation conditions when scaling up this type of battery.